Aggregation kinetics in a chiral selection process

By Frank de Graaf

Master thesis *Natural Sciences (research)*
May 2012- July 2013
Supervisors: drs. P.G. van Rhee, prof. dr. P.C.M. Christianen
Second reviewer: dr. H.L.M. Meekes

Abstract

Many important biomolecules exist in only one of the two possible mirror images structures. This single-handedness, or homochirality of life, is one of the important unresolved issues nowadays. Many different external influences are able to cause enantioselection. Recently, Micali et al.[1] showed that the combination of rotational and magnetic (both levitating and orientating) forces is able to achieve enantioselection of the helical supramolecular aggregates formed by an achiral porphyrin molecule. The kinetics is very important in this process because a falsely chiral influence, such as the combination of rotation and effective gravity, is only capable of enantioselection by means of the kinetics. In this research the kinetics of the supramolecular aggregation is characterized for different conditions and especially the influence of the rotational and magnetic forces is investigated.

The aggregation is a statistical and highly sensitive process in which the microscopic environment is essential. The aggregation kinetics consists of three different stages: nucleation, amplification and saturation. Rotational forces cause an acceleration of the aggregation process in all three stages. Moreover, the aggregates obtained under rotation conditions have a different absolute configuration and are energetically more favorable than when formed under stationary conditions. The nucleation-growth of the aggregates in a rotating solution is influenced by the local hydrodynamics which therefore cannot be described by a solid body rotation. Secondary flows arise in the vial, responsible for the different influences of rotation. With the application of both the magnetic field and rotation, the same enantioselection as Micali et al. is achieved. The magnetic field does on average not have an effect on the aggregation kinetics. The magnetic field does however split the aggregation kinetics for clockwise (fast kinetics) and anticlockwise rotation (slow kinetics) when chiral selection is present. In a batch without chiral selection, also the difference in aggregation kinetics disappeared. The difference in kinetics is the result of a symmetry breaking factor which is yet unknown. This research shows that the external physical forces have a big influence on the aggregation kinetics and this aggregation kinetics plays an important role in the chiral selection process.

Contents

1 Introduction

Many important biomolecules exist in only one of the two possible mirror-image structures, called enantiomers. Either the molecule itself has an asymmetric center, or the three-dimensional structure results in chirality. A good example of a biomolecule with an asymmetric center is an amino acid, the basic unit of proteins, which in functional proteins is always found in the L-configuration. An example of a chiral three-dimensional structure is a helix. For example DNA, which is mostly found as the B-type right-handed double helix. This single handedness is essential for life on earth because molecules with the wrong handedness cannot function properly. The origin of this single-handedness of biological systems, the homochirality of life, is however one of the important unresolved issues nowadays.[2]

Chemists can achieve homochirality by chemical asymmetric synthesis[3], but also external influences inducing enantioselection have been identified. These external influences, including circularly polarized light[4,5], the electroweak interaction[6,7], vortex motion[8], stirring[9,10], catalysis at prochiral crystal surfaces[11] and also combinations of external fields[12,13] are seen as possible causes for the homochirality of life. They can, however, only account for a tiny enantiomeric excess and amplification mechanisms are required to achieve homochirality.

Chirality does not only exist for single molecules, but also supramolecular systems can be chiral because of their three-dimensional structure. Micali et al.[1] found supramolecular enantioselection by purely physical fields and subsequent chiral amplification in absence of these fields. An achiral molecule, tris-(4-sulfonatophenyl)phenylporphyrin ($TPPS_3$) self assembles into chiral J-aggregates. The application of rotational and magnetic forces (both levitating and orientating) in the initial stage of the self-assembly leads to enantioselection. This chiral selection is amplified in growing aggregates, when these forces are no longer applied. The chiral sign of these aggregates is solely determined by the sign of the rotational force and magnetically tuned effective gravitational force and not by the sign of the magnetic field. It is surprising that this effective gravitational force is able to cause enantioselection, because it is a very weak force compared to other forces such as the Coulomb force. This system is also special because it is the first experimental evidence of the theoretical prediction that a falsely chiral influence is able to induce absolute enantioselection in a process that is far from equilibrium. The mechanism behind this enantioselection under influence of the effective gravitational and rotational forces remains a big mystery and is therefore the starting point for this research.

Micali et al.[1] proposed a model based on kinetics measurements of the aggregates. The aggregation process consists of two subsequent steps; nucleation and amplification. The kinetic curve (aggregate absorbance versus time) was however measured under different circumstances than the chiral selection experiments, which might not be justifiable. While the chiral selection experiments involved rotation of a cylindrical vial and magnetic forces, the kinetic absorbance trace was measured of a stirred solution in a square cuvette without the presence of a magnetic field. These external forces might have a great influence on the aggregation kinetics, since these influences also induce enantioselection. Consequently, the proposed model might be wrong.

In this specific aggregation process, the kinetics is very important for the mechanism of chiral selection, because the two enantiomers are iso-energetic. To achieve enantioselection by application of the physical forces (composing a falsely chiral influence), the kinetic route to forming them must be different. This can result in different kinetics of the aggregation process.

In this research, therefore, the aggregation kinetics of TPPS3 into J-aggregates is investigated. First, the aggregation process itself will be characterized to achieve a reproducible procedure for performing the aggregation kinetics. Secondly, the influences of the physical forces (rotational and magnetic) on the aggregation kinetics will be explored by *in situ* absorbance measurements. This includes temperature controlled absorbance measurements of the solution in a rotating vial with and without the presence of a magnetic field. The goal of this research is to investigate the role of both the rotational and magnetic forces on the aggregation kinetics. Based on the aggregation kinetics and the influence of these physical forces, ideas about a model of the aggregation process and a mechanism behind the chiral selection will be proposed.

2 Scientific background

In this chapter, some of the underlying physical concepts and relevant results of previous research will be explained. First, the physical concepts of chirality, circular dichroism, H- and J-aggregates and magnetic influences on molecules and aggregates will be discussed. Secondly, the research of Micali et al.[1] is summarized, followed by a short description of aggregation mechanisms and modeling.

2.1 Chirality

2.1.1 Basic definition

Already in 1904 Lord Kelvin defined chirality: *"I call any geometrical figure, or group of points, chiral, and say it has chirality, if its image in a plane mirror, ideally realized, cannot be brought to coincide with itself".*[14] The basic definition of chirality thus says for chiral molecules/aggregates, that the mirror image of that molecule/aggregate cannot be superimposed on the original molecule/aggregate itself by any proper rotation. For molecules this is true once if there is an asymmetric center, meaning an atom covalently bound to four different groups as depicted in figure 2.1a. Figure 2.1b shows the two enantiomers of a helix which cannot coincide by any proper rotation. Lord Kelvin's definition is just a first and basic definition which provides insight into the meaning of chirality. The concept of chirality will be further developed in the next paragraphs.

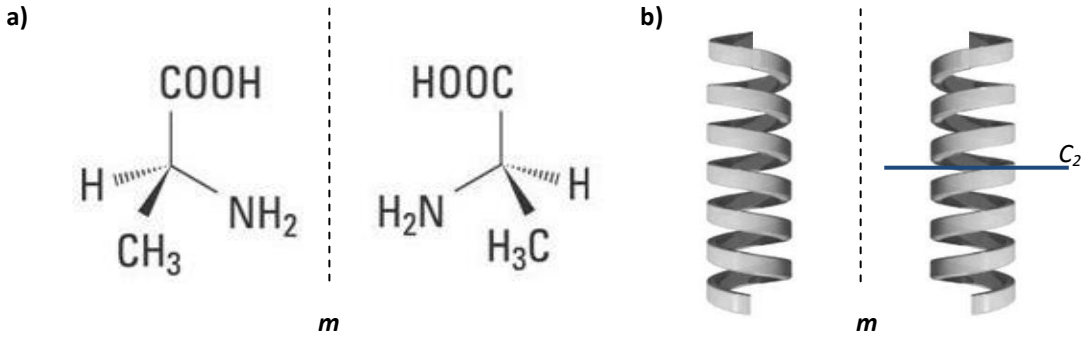

Figure 2.1 Examples of a chiral molecule (a) and a chiral helix (b), including a symmetry axis C_2 for the helix and the mirror planes *m.*

2.1.2 Chirality and symmetry

Chirality is about mirror-images and therefore it is an excellent subject for the application of symmetry principles. Conventional point group symmetries can describe the symmetries of chiral objects. The fact that a mirror-image of a chiral object cannot be superimposed on the object itself does not infer that a chiral object is completely asymmetric, but there are some restrictions. Chirality excludes the so-called improper symmetry elements. Among these are inversion, reflection planes and improper rotations (combining a rotation with reflection through a plane perpendicular to the rotation axis). If an object is imposable on itself after one of these symmetry operations, it cannot be chiral. On the other hand, proper rotations are allowed symmetries in chiral structures. The helix in figure 2.1b has for example a C_2 axis (blue line). Chirality is supported merely by the point groups C_n, D_n, T and I, possessing only proper rotations.[2]

To understand more fundamental symmetry aspects of chirality, symmetries in the laws of physics need to be considered. The invariance of physical laws under certain transformations generates a conservation law that follows from the invariance of the Hamiltonian under the transformation.[15] There are three fundamental symmetry operations under which physical laws should be invariant: parity (P), time reversal (T) and charge conjugation (C).[2]

Parity is the inversion of all spatial coordinates of a particle through the origin of the coordinate system, *(x,y,z)* → *(-x, -y, -z)*. Parity is equal to the application of subsequently a mirror-plane and a rotation and is therefore directly related to chirality. A physical law conserves parity if the physical equations (e.g. Maxwell or Newton's equations) do not change under changing all spatial coordinates according to the parity operation. Conservation of parity implies that the parity operator *P* commutes with the Hamiltonian *H*. As a consequence, if ψ_a is an eigenfunction of *H* with eigenvalue E_a, then $P\,\psi_a$ is also an eigenfunction of *H* with the same eigenvalue as is shown below.

$$H\psi_a = E_a\,\psi_a$$
$$[H,P] = 0 \qquad \text{, meaning} \quad HP\psi_a = PH\psi_a$$
$$HP\psi_a = PE_a\,\psi_a = E_a\,P\,\psi_a$$
$$so\ H\,(P\psi_a) = E_a\,(P\psi_a)$$

This means that for a chiral system, if *H* commutes with *P*, the enantiomers have to be iso-energetic.

Time reversal reverses the motion of all particles in a system and is formulated as the inversion of the time coordinate *(t)* → *(-t)*. Analogous to parity, if the physical equations do not change under time reversal, there is conservation of time reversal, also called reversality. Again this means that the time reversal operator *T* commutes with the Hamiltonian *H*. If *H* is time independent, then the stationary state ψ_a and its time reversed state $T\psi_a$ have the same energy eigenvalue.

The third fundamental symmetry operation is called charge conjugation (*C*) and it interconverts particles and antiparticles. This symmetry operation is not directly relevant here, but it appears in the CPT theorem, which is important. The CPT theorem states that a system is always invariant to the combined operation of *C,P* and *T*.[16] The Hamiltonian of a system will thus always commute with the operator combination *CPT* and the energy of a wavefunction ψ_a is the same as for the wavefunction $CPT\psi_a$. This will have important consequences for the next paragraphs. Some definitions of vectors and scalars which will be used in the proceeding paragraphs are given in table 2.1.

Table 2.1 Definitions of different scalars en vectors

Name	**Definition**	**Example**
Scalar	Physical quantity with a magnitude but no direction	Energy
Pseudoscalar	A scalar which changes sign under space inversion	Optical rotary dispersion
Polar vector	Quantity with both a magnitude and a direction, which changes sign under space inversion	Gravity
Axial vector	Quantity with both a magnitude and a direction, which does not change sign under space inversion	Angular momentum
Time odd (even) vector	A vector that does (not) change sign under time reversal is called time odd (even)	Momentum (gravity)

2.1.3 True and false chirality

The term chirality can be applied to stationary objects such as the examples in figure 2.1, but also to systems in motion. The time-reversal operator is needed here to clarify the concept of chirality. A chiral system should be a system that supports time-even pseudoscalar observables. Pseudoscalar observables are only supported by quantum states with mixed parity that conserve time reversal. 'Chiral' systems can therefore be classified into two kinds; truly chiral systems and falsely chiral systems. *Barron* stated: "A truly chiral system exists in two distinct enantiomeric states that are interconverted by space inversion, but not by time reversal".[2] In a falsely chiral system the enantiomeric states are not only interconverted by space inversion but also by time reversal.[17]

Figure 2.2 shows examples of an achiral system (a), a truly chiral system (b) and a falsely chiral system (c). Figure 2.2a shows a rotating cylinder which does not change under parity operation and is therefore per definition an achiral system. Figure 2.2b shows a combination of rotation and translation, e.g. circularly polarized light. This is a truly chiral system because it does not conserve parity, but it does have reversality. Finally, figure 2.2c shows a spinning cone which is an example of a falsely chiral system. The spinning cone does not conserve parity and also time reversal is not conversed.

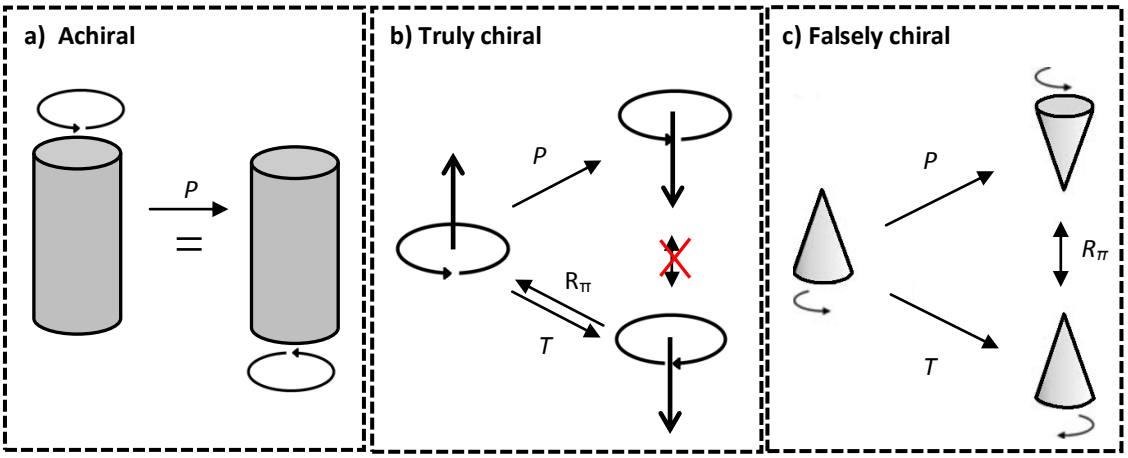

Figure 2.2 An example of an achiral system, a rotating cylinder (a), a truly chiral system, circularly polarized light (b) and a false chiral system, a spinning cone (c).[17] *P* represents the parity operator, *T* represents the time reversal operator and R_π is a rotation over 180 degrees.

2.1.4 Chiral influences and absolute enantioselection

Absolute enantioselection is the production of an enantiomeric excess by the use of physical influences. According to the CPT theorem above, there are restrictions on what kind of physical influences can induce enantioselection. The enantiomeric excess' obtained by using physical influences are nevertheless expected to be small. To get large amounts of enantiomeric excess, chiral amplification mechanisms are needed.

Analogous to the definition of truly and falsely chiral systems, chiral influences can also be characterized as either true or false. A truly chiral influence is parity-odd and time- even while a falsely chiral influence is characterized by being parity-odd and time-odd. A chiral influence should at least be composed of two collinear vectorial influences. The symmetry characteristics of the vectorial influences determine if the combination of these influences is either achiral, truly chiral or falsely chiral. Table 2.2 characterizes the chirality of combinations of two collinear vectors with properties as defined in table 2.1.

Table 2.2 Characterization of the chirality of two collinear vectors

	Time-even Polar	*Time-odd Polar*	*Time-even Axial*	*Time-odd Axial*
Time-even Polar	X	X	True[a]	False[c]
Time-odd Polar	X	X	False[b]	True[d]
Time-even Axial	True[a]	False[b]	X	X
Time-odd Axial	False[c]	True[d]	X	X

Superscripts indicate combinations that are exactly equal because the order of the vectors does not matter.

An example of a truly chiral influence is the combination of a magnetic field (time-odd axial) and collinear light (wave vector is time-odd polar). [18] A falsely chiral influence is for example a combination between a magnetic field (time-odd axial) and an electric field (time-even polar).

According to these symmetry characteristics, a truly chiral influence is able to induce enantioselection at both equilibrium and non-equilibrium processes. On the contrary, a falsely chiral influence can only induce enantioselection in processes that are far from equilibrium. The ability of inducing absolute enantioselection does however not mean that enantioselection actually occurs, because the influence might be too weak.

A truly chiral influence can induce enantioselection because there is an energy difference between the two enantiomers in the presence of this influence. According to the CPT theorem, the Hamiltonian commutes with the operator combination *CPT*. For a truly chiral influence, the combination *PT* is not conserved and the energy of these chiral molecules will therefore not be the same in the presence of this influence. This energy difference in chiral molecules is called the parity-violating energy difference (PVED). Only the energies of the charge conjugated, space inverted molecules are equal.

On the contrary, a falsely chiral influence will not result in different energies for the different enantiomers in presence of this influence, because the Hamiltonian *H* commutes with *PT*. Because the energies of the enantiomers are equal, a falsely chiral influence cannot induce enantioselection in an equilibrium process. In a system far from equilibrium, however, not only the thermodynamics but also the kinetics is important.[19,20] Figure 2.3 illustrates the ability of a falsely chiral influence to induce enantioselection via the kinetics. An achiral molecule *A* forms chiral structures, mirror images *R* and *S*. These structures are of equal energy (same *ΔG* with respect to *A*) in the presence of the falsely chiral influence since the falsely chiral influence breaks *P* and *T* separately but is PT-invariant overall. The energy difference *ΔG* determines how much of *A* will be converted to *R* and *S*, the potential energy profile towards *R* and *S*, determines the kinetics (forming rates).

The potential energy barrier usually is equal for a forward and backward reaction based on the reversality of the system. A process with a falsely chiral influence is however not invariant under time reversal which means these potential energy barriers can be different for the back and forth reaction (depicted by the arrows). Symmetry must be recovered in the time reversed enantiomeric process, i.e. the process generated by *PT* rather than *T* alone, depicted by the red and blue lines in figure 2.3. A falsely chiral influence can thus act as a chiral catalyst because it alters the potential energy profiles to change the relative forming rates of the enantiomers without affecting the equilibrium thermodynamics. This way a falsely chiral can induce absolute enantioselection by means of kinetic control.

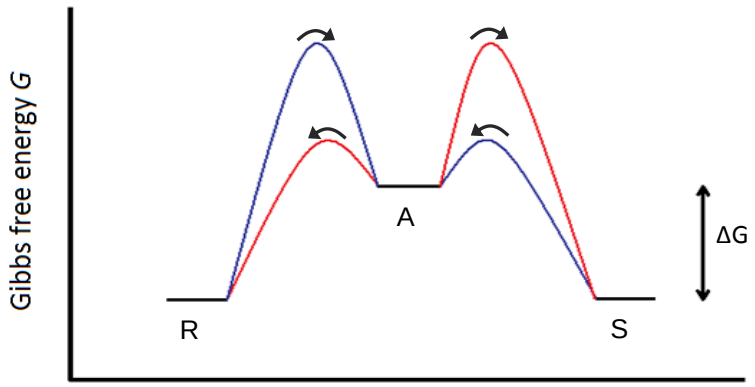

Figure 2.3 Schematic representation of the ability of a falsely chiral influence to induce absolute enantioselection. The potential energy profiles are shown for reactions of an achiral molecule *A* producing a chiral structure *R* or its enantiomer *S* in the presence of a falsely chiral influence. In the presence of a falsely chiral influence both enantiomers are of equal energy with respect to the achiral molecule *A* (*ΔG*). The falsely chiral influence breaks time reversal symmetry which means the potential energy barriers for the forward and backward reaction (depicted by the arrows) are different. Symmetry is recovered for the time reversed enantiomeric process (generated by *PT*), indicated by the red and blue lines. The falsely chiral influence generates different energy profiles giving rise to different forming rates for *R* and *S,* resulting in absolute enantioselection.[20]

2.2 Circular Dichroism

2.2.1 Principles of circular dichroism

Optically active (or chiral) systems are studied by two general techniques, optical rotary dispersion (ORD) and circular dichroism (CD). Optical rotary dispersion results from a different refractive index for left and right circularly polarized light while circular dichroism is the difference in absorbance for the left and right circularly polarized light. The refractive index is coupled to the absorbance via the Kramers-Kronig relations, so both techniques are based on the same general principles.[21]

A general quantitative description of circular dichroism can be provided using the law of Lambert-Beer. The law of Lambert-Beer describes the relation between the absorbance *A* and properties of the material through which the light is traveling. The absorbance *A* is defined as the negative logarithm of the intensity of the transmitted light *I* divided by the intensity of the incident light I_0.[22]

$$A = -\log_{10}\frac{I}{I_0} = \varepsilon \cdot c \cdot d \qquad (1),$$

in which ε is the molar absorbance coefficient of the material, *c* the concentration of the material and *d* the distance over which the light is travelling through the material. For an optically active medium the absorbance of left circularly light (A_L) is different than for right circularly polarized light (A_R), resulting in an absorbance difference ΔA which is related to a difference in molar absorbance coefficient $\Delta\varepsilon$ by;

$$\Delta A = A_L - A_R = \log_{10}\frac{I_R}{I_0} - \log_{10}\frac{I_L}{I_0} = \log_{10}\frac{I_R}{I_L} = c \cdot d \cdot \Delta\varepsilon \qquad (2).$$

As seen from equation (2), no reference beam is needed because I_0 is eliminated from the equation.

2.2.2 Ellipticity

Because of the difference of absorbance of left and right circularly polarized light, circular dichroism also results in another effect called “ellipticity”. Ellipticity is the effect that linear polarized light passing through an optically active medium becomes elliptically polarized characterized by an angle φ.

This effect is due to the fact that linear polarized light is composed of left circularly polarized light and right circularly polarized light with equal amplitude (respectively E_L and E_R). The optically active medium absorbs one more than the other, resulting in elliptically polarized light afterwards, shown in figure 2.4.

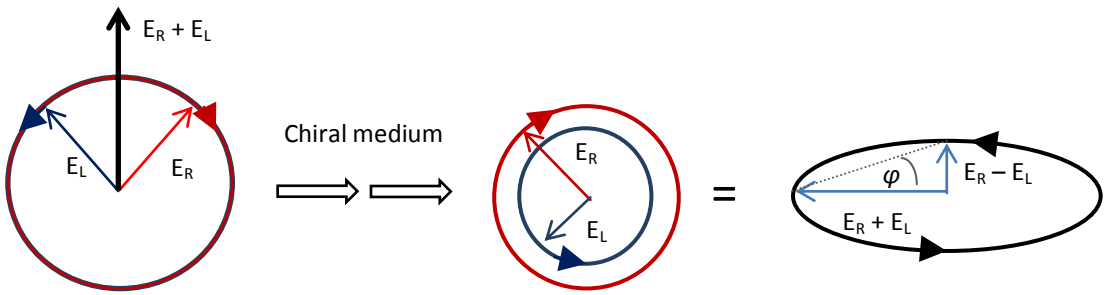

Figure 2.4 Linear polarized light (black) consists of left circularly polarized light (blue) and right circularly polarized light (red) which are absorbed differently in a chiral medium. This results in elliptically polarized light characterized by an angle φ.

The relationship between φ (mdeg) and ΔA is given in equation (3), for derivation see S1.[19]

$$\varphi = \Delta A \cdot \frac{\ln 10}{4} \cdot \frac{180}{\pi} \cdot 1000 \approx 32982\, \Delta A \qquad (3).$$

When one measures the circular dichroism of an optically active medium, either ellipticity spectra or ΔA spectra are obtained which are connected by equation (3).

2.2.3 Quantum mechanical description

The origin of (electronic) circular dichroism is in the quantum mechanics of a chiral system. The quantum mechanical quantity describing circular dichroism is the *rotational strength*. The rotational strength is proportional to the area of the circular dichroism band. The rotational strength R_{01} is the imaginary part (*im*) of the scalar product of the electric (μ) and the magnetic (m) transition moments between the ground state ψ_0 and the excited state ψ_1.

$$R_{01} = im\{<\psi_0|\,\mu\,|\psi_1> \cdot <\psi_0|\,m\,|\psi_1>\} \qquad (4),$$

with $\mu = -e\sum_{i=0}^{n} r_i$
and $m = \gamma \sum_{i=0}^{n} r_i \times p_i$

with r_i the position vector of electron i, p_i the momentum vector of electron i, n the total number of electrons, e the electron charge and γ the gyromagnetic ratio of the electron. This relation can be derived using time-dependent perturbation theory with the assumption that the wavelength of the light is much bigger than the dimensions of the system. Equation (4) puts a few restrictions on systems that show circular dichroism. The transition from ψ_0 to ψ_1 only shows circular dichroism if the transition has both an electric transition moment and a magnetic transition moment and these moments are not perpendicular to each other.[22]

2.3 H- and J- aggregates

In 1937, Scheibe et al.[23] and Jelley et al.[24] independently found an unusual behavior of pseudoisocyanine chloride (PIC chloride) in aqueous solutions. Compared to PIC chloride in ethanol, in water the absorbance maximum (Soret band) was shifted to lower energies when either the concentration of the PIC chloride was above 10^{-3} M or a sodium chloride solution was added. This shift was correctly interpreted by Scheibe as a result of the aggregation of the PIC molecules. The individual molecules in an aggregate are interacting via exciton coupling which alters the electronic properties.

2.3.1 Exciton coupling

Excitation of a molecule usually involves the movement of an electron from a high energy occupied molecular orbital (MO) to a low energy unoccupied molecular orbital. This movement is always associated with an electric transition dipole, otherwise excitation is not allowed. This dipole has both an orientation and a magnitude that varies with the nature of the transition and the molecule involved. When two or more molecules are close to each other, the electric transition dipole of one molecule can interact with the transition dipole of another molecule. For this interaction to be significant, the electronic transitions associated with the molecules should have similar energies and intensities. This dipole-dipole coupling of locally excited states produces a delocalized excitation (exciton) and results in splitting of the locally excited states (*exciton* or *Davydov* splitting), see figure 2.5. This interaction is called exciton coupling.[25]

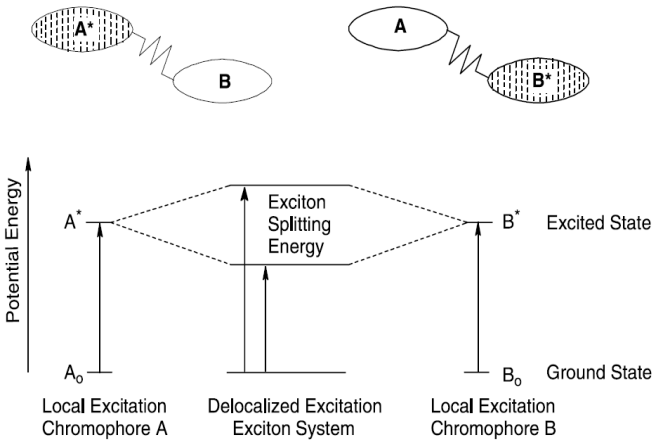

Figure 2.5 Schematic representation of exciton coupling[25]

Exciton coupling results in two different possible excitations with different energies. Compared to the absorbance of the single molecule, one excitation is redshifted en the other is blueshifted. Not always are both transitions allowed. If excitation is allowed for the blueshifted (hypsochromically shifted) absorbance band with respect to the monomers, the term H-aggregates is used. H-aggregates often show low or no fluorescence because the fluorescence can be quenched by the redshifted energy level.

Aggregates with an allowed excitation of the absorbance band that is shifted to the longer wavelength (bathochromically shifted) with respect to the monomer absorbance band are generally termed Scheibe-aggregates or J-aggregates, named after their discoverers. J-aggregates possess a nearly resonant fluorescence with a narrow band (small Stokes shift).

The terms H- and J- aggregates are somewhat misleading because it does not necessarily mean that they are actually different aggregates. Both transitions are often allowed in one type of aggregates, meaning the aggregates both show the red- and blueshifted absorbance.

2.3.2 Exciton- coupled circular dichroism

If the interacting molecules inside an aggregate are orientated in a chiral structure, each of the UV/Vis exciton bands, if allowed, has a corresponding CD spectrum. The interaction of circularly polarized light and an aggregate (one enantiomer) is different for left circularly polarized light and right circularly polarized light. If the achiral molecules are stacked in a chiral order (e.g. screw wise), the electric transition dipole contains both a translation and rotation. For a specific enantiomer this redistribution of electrons is easier achieved for right circularly polarized light than for left circularly polarized light. Therefore there will be an energy difference in the absorbance peaks for right circularly polarized light and left circularly polarized light resulting in a bisignate CD spectrum, see figure 2.6. In the wavelength region close to the absorption, the CD signal varies rapidly with wavelength, crosses zero at the absorbance maximum and then again varies rapidly with wavelength but in opposite direction. If the CD signal first decreases with increasing wavelength it is called the *positive Cotton effect*. If the CD signal first increases with increasing wavelength it is called the *negative Cotton effect*. Figure 2.6 shows an example of the positive *Cotton effect*.[22]

The order of the signs in the bisignate CD spectrum is related to the absolute orientation of the interacting molecules. The CD spectra of the enantiomers are equal in magnitude but opposite in sign. Only media in which there is an enantiomeric excess can be observed by circular dichroism, since in a racemic mixture the CD signals of both enantiomer cancel each other out.

Chiral stacking of two molecules

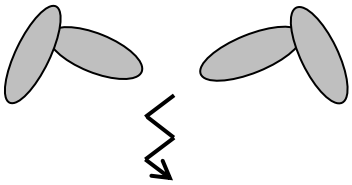

In the interaction of these structures with light, a redistribution of the electron cloud by both rotation (in plane) and translation (perpendicular to plane) occurs.

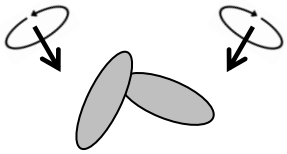

This redistribution is for one enantiomer easier achieved by left- than for right circularly polarized light. This gives an energy difference of the absorbance for both polarizations, resulting in a bisignate CD spectrum (right)

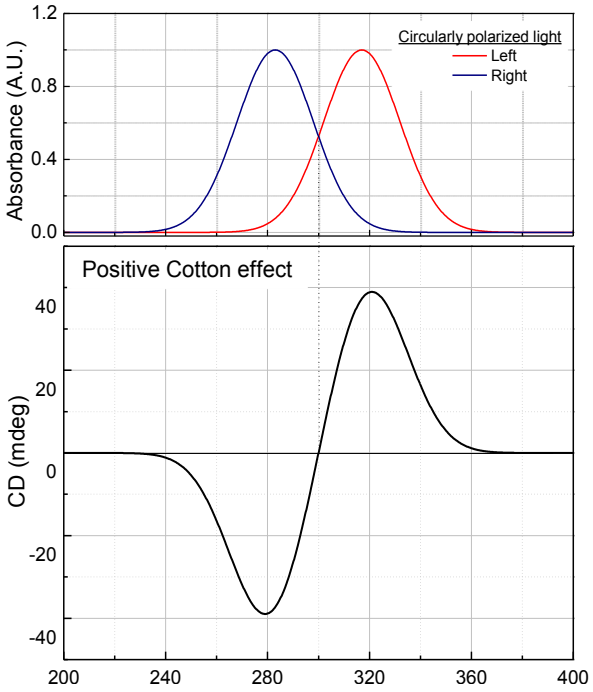

Figure 2.6 Schematic view of the interaction of circularly polarized light with a chiral stacking of two molecules and the absorbance and bisignate CD spectrum. This spectrum is an example of the positive *Cotton effect*.

Factors influencing the CD spectrum are the magnitude of the transition dipoles, the orientation of the transition dipoles and the distance between them. Because excitons originate in electron transition dipole-dipole coupling, transitions with large dipoles will be more effective. The distance and relative orientation of the transition dipoles are thereby also important factors and information about the orientation can be deduced from the observed absorbance and CD spectra. For example, both a parallel and in-line orientation of the transition dipoles cannot show circular dichroism, since it is not a chiral system. By application of the *Exciton Chirality Rule* by Harada and Nakanishi[22] the helical orientation of the transition moments can be deduced.

Combining this information with knowledge about the electronic structure, the absolute configuration of the molecules can be found. In a typical bisignate CD spectrum a dissymmetry parameter Δg *i*s defined to quantify both the magnitude and sign of the chirality.[1]

$$\Delta g = g(\lambda_1) - g(\lambda_2) \qquad \text{and} \qquad g = \frac{\Delta A}{A} = \frac{A_L - A_R}{A} \qquad (5),$$

in which λ_1 and λ_2 are the wavelengths at the peaks (either a minimum or a maximum) of the *g* value, and $\lambda_1 > \lambda_2$.

In the example above, a system of only two molecules is discussed. For systems consisting of more identical molecules, the CD signal can be much more complicated.

2.3.3 Molecules forming J-Aggregates: Porphyrins and in particular $TPPS_3$

Many different molecules form H- and J-aggregates. Besides isocyanine dyes, also merocyanines, squaraines, chlorofyls and perylene bisimides are forming J-aggregates under specific conditions[26]. Here, the focus will be on porphyrins (class of chlorophylls, see figure 2.7) and more specifically on tris-(4-sulfonatophenyl)phenylporphyrin ($TPPS_3$). Porphyrins are tetrapyrroles and exist in several different forms. In nature, the chlorin, bacteriochlorin and phthalocyanine are derivatives of tetrapyrroles and using organic chemistry many other different derivatives (like $TPPS_3$) can be made.

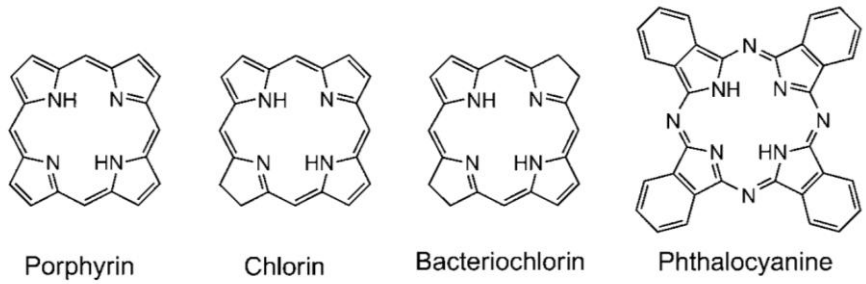

Figure 2.7 Structures of the class of chlorophylls that are able to from J-aggregates. The basic unit of a porphyrin is shown with some of its natural derivatives.[29]

In solution, porphyrin molecules appear in different forms depending on the pH. The two nitrogen atoms in the center occupy a free election pair which can act as a Brønsted base. In solutions of pH >4.8 the $TPPS_3$ molecule is mainly found in its free base form and in solutions with pH>4.8 the molecule is found in its diacid form, as shown in figure 2.8.[26]

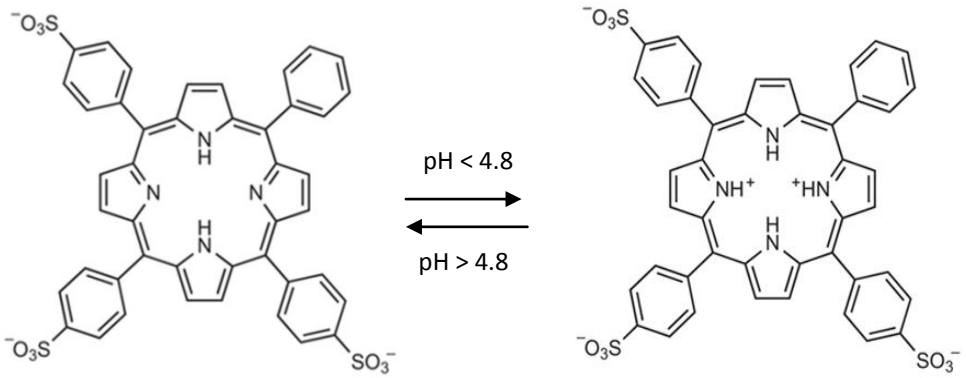

Figure 2.8 Structure of tris-(4-sulfonatophenyl)phenylporphyrin ($TPPS_3$) in its free base (left) and diacid form (right) in aqueous solutions.

The H- and J-aggregates are formed by interplay of hydrogen bonds, π-π stacking interactions and electrostatic interactions. The positive charges in the center of the molecule are a necessary ingredient for aggregation, because they counterbalance the negative charges at the periphery of the molecule. $TPPS_3$ is therefore only able to form J-aggregates when the pH is smaller than 4.8. Besides, the monomer concentration should be high enough and the addition of a salt can facilitate the aggregation. Salts can induce the aggregation because the counter ions are able to form a "cloud' around the J-aggregates which reduces the electrostatic repulsion between the anionic monomers.[26]

$TPPS_3$ is an achiral molecule, but the J-aggregates from $TPPS_3$ have a helix-like structure, resulting in two different mirror-images that are non-superimposable. The exact structure of the aggregates formed by $TPPS_3$ is unknown, however for $TPPS_4$ recently the structure has been revealed by X-ray and electron diffraction methods.[27] $TPPS_4$ has an extra sulfonate group on the fourth phenyl of $TPPS_3$. The exact structure of $TPPS_3$ might be a lot different because the symmetry is broken by removing one sulfonate group. The absorbance and CD spectra are however pretty similar for both the porphyrin molecules and their aggregates. The basic structural architecture responsible for the excitonic spectra must therefore be shared by the different J-aggregates.

2.4 Magnetic field influences on molecules and aggregates

A magnetic field has several different influences on the $TPPS_3$ molecules and aggregates in a solution. Three of these influences are described on the next pages; the Lorentz force, magnetic alignment and magnetic levitation.

2.4.1 Lorentz force

The Lorentz force, also called the magnetic force, can be derived from Maxwell's equations and is the force on a charged particle moving in a magnetic field.[28] The Lorentz force F_L depends on the charge o a particle q, the velocity $\vec{v}$ of this particle and the magnetic field $\vec{B}$

$$\vec{\mathrm{F}}_{\mathrm{L}} = q\,(\vec{v}\,\mathrm{x}\,\vec{B}) \qquad (6).$$

The direction of the Lorentz force is determined by the cross product, following the right hand rule. In the diacid form, $TPPS_3$ is a particle with three negative charges and two positive charges, so five different Lorentz forces are present on each molecule and because there is an overall negative charge of the molecule, there is a resulting Lorentz force.

In the case of forming J-aggregates from $TPPS_3$, also other charged particles are present, such as sodium ions, chloride ions, sulfate ions and hydroxonium ions. The Lorentz force will also act on these particles.

2.4.2 Magnetic alignment

Besides the general Lorentz force, there is also a magnetic alignment force. This force results from the magnetic moment a molecule possesses in a magnetic field.[29] The diamagnetic moment $\vec{m}$ of a molecule is proportional to the magnetic field $\vec{B}$.

$$\vec{\mathrm{m}} = \frac{1}{\mu_0 N_a}\bar{\bar{\chi}}_{mol} \cdot \vec{B} \qquad (7).$$

In equation (7), $\bar{\bar{\chi}}_{mol}$ is a second rank symmetric tensor representing the molar diamagnetic susceptibility of a specific material, μ_0 is the permeability of free space and N_a is Avogadro's number. This second rank tensor can always be diagonalized, which leads to a $\bar{\bar{\chi}}_{mol}$ of the form

$$\bar{\bar{\chi}}_{mol} = \begin{pmatrix} \chi_{x'x'} & 0 & 0 \\ 0 & \chi_{y'y'} & 0 \\ 0 & 0 & \chi_{z'z'} \end{pmatrix} \qquad (8),$$

with x', y' and z' the principal axes of the molecule. The energy E_{mag} of this magnetic moment is dependent on its orientation with respect to the magnetic field.

$$E_{mag} = -\int_0^B \vec{m} \cdot d\vec{B} \qquad (9).$$

To minimize this magnetic energy an orientation force arises. In the simplest model, a porphyrin molecule can be regarded as a flat ellipsoid disk, which reduces the second rank tensor $\bar{\bar{\chi}}_{mol}$ to a tensor with only two different diagonal components of the molar susceptibility $\chi_{\parallel}$ and $\chi_{\perp}$.[1] The molar susceptibility along the long molecular axis is called $\chi_{\parallel}$ and the molar susceptibility along the short molecular axis is $\chi_{\perp}$. Equation (9) now reduces to an equation for the increase in energy ΔE_{mag} due to the magnetic field. This increase in energy is a function of the angle ϑ between the long molecular axis and the magnetic field and the difference in molar susceptibility $\Delta\chi = \chi_{\parallel} - \chi_{\perp}$

$$\Delta E_{mag} = -\frac{1}{2\,\mu_0 N_a}\,\Delta\chi\; B^2(\cos\theta)^2 \qquad (10).$$

The orientation force leads towards an orientation of the molecule with the axis of the smallest diamagnetic susceptibility parallel to the magnetic field.

For individual molecules this magnetic alignment energy is much smaller than the thermal energy k_BT and it is not possible to align this molecule with present day high magnetic fields. Alignment is therefore only applicable to materials that contain a sufficient amount of coupled molecules in order to result in an energy difference that is bigger than the thermal energy, for example molecular aggregates. The $\Delta\chi$ of a porphyrin molecule is about $7.5 \cdot 10^{-9}$ m^3/mol, which means that aggregates consisting of at least 1000 porphyrin molecules can be magnetically aligned at a magnetic field of 25T.[30,31]

2.4.3 Magnetic levitation

Every diamagnetic substance experience forces in regions with a magnetic field gradient. For diamagnetic substances, $\chi < 0$, the force is directed towards a lower magnetic field to minimize the energy according to equations (7) and (9). This magnetic force can be used to counteract the gravity resulting in stable magnetic levitation[32] and it can also be used to create a tunable effective gravity. [33]

The magnetic force is proportional to χ, $B(z)$ and $B'(z)$, where χ is the magnetic susceptibility , $B(z)$ is the magnetic field strength at position z inside the magnet and $B'(z)$ the corresponding magnetic field gradient $\frac{dB(z)}{dz}$. Both the field strength and field gradient are in the z-direction assuming the field is homogeneous in the other directions. The effective gravity on water is given by equation (11) in which G_n is the normal gravitational acceleration of 9.81 m/s^2. [1]

$$G_{eff} = G_n \cdot \left(1 + \frac{B(z)B'(z)}{1360\ T^2/m}\right) \qquad (11).$$

Depending on the sign of the field gradient this magnetic force can result in an effective gravity that is higher or lower than normal gravitational forces, and even an inverted gravity is possible.

2.5 Selection of supramolecular chirality

The starting point for this research is the *Nature Chemistry* publication by Micali et al. [1] about the selection of supramolecular chirality. Micali et al. were able to achieve enantioselection of the J-aggregates of $TPPS_3$ by use of external physical influences; effective gravity and rotation. The handedness of the J-aggregates is directed by the sign of both the angular momentum L and the effective gravity G_{eff}(figure 2.9). This section shortly summarizes the experiments and results, since they are important for comparison with the experiments in this research.

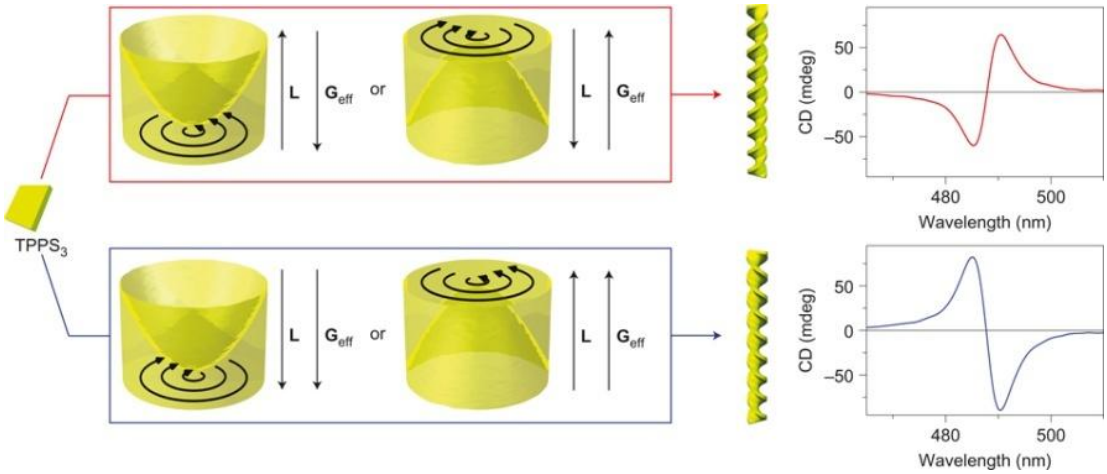

Figure 2.9 Correlation between the observed chirality (bisignate CD spectra) and the applied physical forces; rotation L and effective gravity G_{eff}. For illustrative purposes, $TPPS_3$ is depicted as a platelet and the aggregates are depicted as perfect helices.

The external physical influences; rotation and effective gravity

Rotation and effective gravity are used as external physical forces. Rotation was applied by rotating the cylindrical vial (in which the aggregation mixture is present) at a frequency of 15 Hz. Such rotation of cylindrical vials is described by a solid- body rotation, because it does not contain any translational components. The effective gravity is tuned by the application of high magnetic fields, through magnetic levitation. Equation (11) represents the effective gravity of the reacting solution, since the solution is almost only composed of water. By tuning the position of the vial inside the magnet, it experiences a different field gradient and this way a different effective gravity.

The combination of this rotational and effective gravitational force offers several advantages in these experiments. First of all, both forces are independently tunable in size and direction, permitting the investigation of the separate effects of both forces. Secondly, it is easy to impose the physical forces only a certain amount of time (e.g. only in the nucleation phase) and remove the forces during the subsequent growth of the aggregates. This allows for disentangling the chiral selection and amplification processes. Another advantage is that the chiral sign of the hydrodynamic flow can be controlled by two parameters, inverting rotation or the effective gravity, which can act as a control.

Note: The combination of rotation and effective gravity is a falsely chiral influence, since rotation is a time-odd axial vector and effective gravity is a time-even polar vector (see table 2.2). Micali et al. were the first to prove that a falsely chiral influence can induce enantioselection in a process that is far from equilibrium.

The experiments and results

A solution of 3µM $TPPS_3$ in MilliQ was made and aggregation was triggered by lowering the pH to 1.9, by adding sulfuric acid, and increasing the ionic strength by sodium chloride (0.1M final concentration). Seven cylindrical vials containing this solution were placed at different positions (z) inside the magnet (to achieve different G_{eff}). The magnetic field and rotation were applied from the beginning of the aggregation for a period *t*, ranging from 30 to 120 minutes. Temperature was held stable at temperature of 23°C. The full aggregation process required about three days to complete.

The aggregates exhibit an absorbance band at 490nm and their chirality is measured after three days by measuring circular dichroism of the solution in a quartz cell. Figure 2.9 shows the typical bisignate CD spectra that were observed. Figure 2.10 shows the results of these measurements in which the dissymmetry factor *Δg i*s plotted for the different directions of the physical forces (a) and against $B^2G_{eff}^{-1}$ (b).

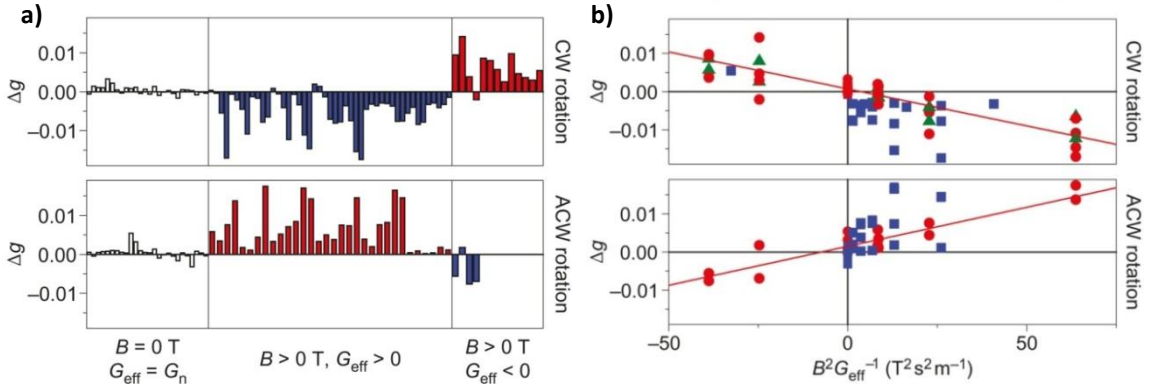

Figure 2.10 Selection of supramolecular chirality results. a) The dissymmetry factor Δg measured for clockwise (upper panel) and anticlockwise (lower panel) rotation, with B =0 (left panels) and B>0 (middle and right panels) resulting in a G_{eff}>0 (middle panels) and G_{eff} < 0 (right panels). b) Δg plotted for all experiments against $B^2G_{eff}^{-1}$, to show the magnetic field dependency of the chiral selection. Green triangles, *t*= 30 minutes; red circles, *t*= 60 minutes; blue squares, *t*=120 minutes.

Here, the dissymmetry factor Δg is defined as g(491nm) – g(486nm), instead of subtracting the maximum and minimum of g (equation (5)), which is in practice very similar. Inverting the gravity or inverting the rotation results in opposite chirality of the J-aggregates. Inverting both leaves the chiral sign unchanged. In case of no external physical forces, a bias towards positive Δg is clearly visible (left panels in figure 2.10). This bias is however overruled by the applied set of physical forces. The absolute value of the dissymmetry parameter has a large variation between the measurements, showing that this is a statistical process.

In the presence of the external physical forces, the values of Δg are a lot bigger than without these forces (when no chiral selection takes place). The absence of chiral selection when no magnetic field is applied demonstrates the importance of the alignment of the aggregates. The sign of the magnetic field does however not matter for the magnetic alignment, so it is not the magnetic field itself that plays the fundamental role. The important roles here are played by the effective gravity and alignment forces, which both scale with B^2. This dependence is shown in figure 2.10b.

The kinetics of the aggregation is monitored by measuring the absorbance at 490nm over time, shown in figure 2.11. Also the time at which the external influences are present is indicated, and this shows that the external influences are only present in the nucleation stage of the aggregation. Based on this aggregation kinetics curve, Micali et al. proposed the following model for the enantioselection mechanism:

"In the nucleation period preceding the growth of the aggregates, nano-assemblies form in the solution. At this stage the hydrodynamic flow gives a chiral twist to the nuclei. The magnetic field orients the nuclei along the rotation axis, and thereby decreases the influence of the randomizing Brownian motion that tends to destroy the chirality. Once the chiral seeds are formed, they serve as templates for chiral growth, even after the chiral influence is removed, which leads to amplification of the supramolecular chirality".[1]

This kinetics experiment is however performed in a quartz cell without an applied magnetic field and with stirring instead of rotation. This situation might not be representative for the situation in the chiral selection experiments. In this research, the influence of these external physical influences on the aggregation kinetics is investigated.

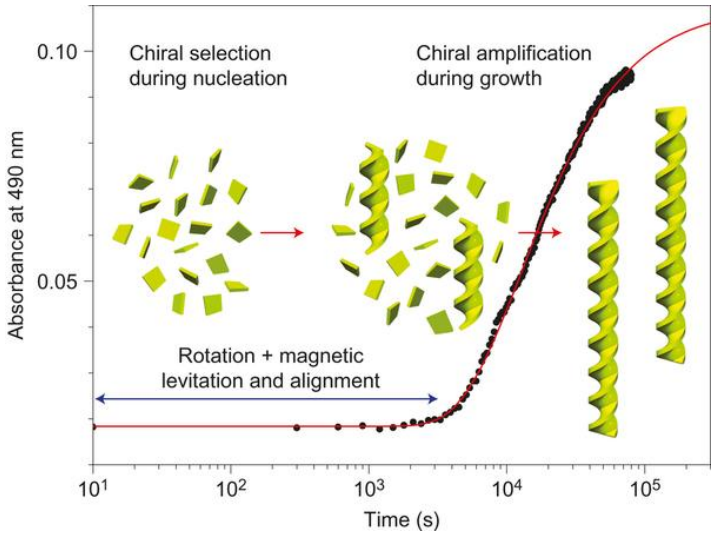

Figure 2.11 The aggregation kinetics of $TPPS_3$ forming J-aggregates including a proposed model for the chiral selection and amplification. The external physical influences are only present in the early stage of the aggregation (blue arrow). At this stage , the achiral $TPPS_3$ monomers (yellow plates) self-assemble into small nano- assemblies (short yellow helices), which in a couple of days grow into large chiral structures (yellow helices) .

2.6 Mechanisms and modeling

2.6.1 Aggregation mechanisms

The process of aggregation is also called supramolecular polymerization to link it to 'normal' polymerization. The biggest difference in supramolecular polymerization and 'normal' polymerization is that it involves non-covalent bonding between the monomers resulting in a reversibility of the polymerization. The extent of the supramolecular polymerization, or aggregation, is therefore dependent on thermodynamic forces such as concentration, temperature and pressure.[34]

There are several mechanisms for supramolecular polymerization, resulting in different models for the aggregation kinetics and thermodynamics. Thermally induced growth mechanisms are considered, meaning that aggregation will take place when the temperature is below a critical value T_a. This is of course also concentration-related.

Two general models for supramolecular polymerization are the isodesmic and cooperative models.[29] In the isodesmic model, the strength of the non-covalent interactions between the monomers and aggregates is independent of the size of the aggregate. The association constant *K* and the reaction rate constant *k* are thus the same at any moment during the aggregation.

In the cooperative model the aggregation takes place in two stages (simplest case), with each their own rate constant en association constant. First there is the nucleation stage, with a small reaction rate k_0 , in which the molecules are forming nuclei (activation for aggregate growth). Secondly there is the elongation stage in which molecules grow on the nuclei, with a usually much bigger rate constant k_1. The cooperative model is also often called the nucleation—elongation model. Figure 2.12 summarizes the differences between the isodesmic (a) and cooperative (b) model.

In figure 2.12b, nucleation is depicted as some sort of activation of a single molecule. A more realistic view is that nucleation is considered as forming clusters (nuclei) of a few monomers which requires a certain activation energy. On this nucleus other monomers can attach more easily, represented by the elongation phase which has a different rate constant. The biggest difference in the aggregation kinetics of these two models is the presence/absence of a nucleation stage. Besides the difference in the kinetics, the two mechanisms can also be distinguished in forms of thermodynamics. The relationship between temperature and fraction of polymerized material is different for these two models, because the existence of an extra association constant in the cooperative model. For more information on this topic, see ref [34] and [35].

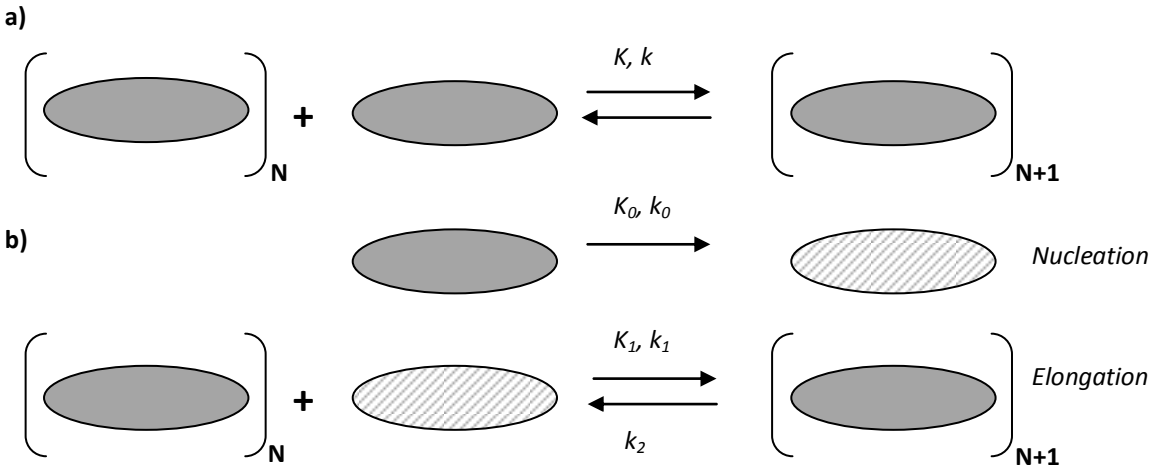

Figure 2.12 Schematic representation of the isodesmic model (a) and cooperative model (b) for the aggregation mechanism. The isodesmic model consists of one stage with one association constant *K* and rate constant *k* while the cooperative model consists of two stages (nucleation and elongation) with each their own constants.[29]

Another, more specific model for the aggregation kinetics of porphyrin assemblies was published by Pasternack et al. in 2000.[36] With this model, the aggregation kinetics of $H_4TPPS_4^{2-}$ could be perfectly fitted. Originally this model is derived for the auto-catalyzed formation of organized assemblies of DNA-bound porphyrins[37]. In this process the aggregates catalyze the rate-limiting step in the aggregation process, and especially the size of the aggregates is important.

The *Pasternack model* is a nonconventional approach of analyzing aggregation kinetics, because it is using a fractal approach. For fractal aggregates, the mean aggregate size *s(t)* as a measure of time *t* scales with the power t^n and the rate constants should occupy such a time dependence as well. The model is based on a system in which there is a rate-limiting step in the early stage (nucleation) and this step is catalyzed by the aggregates. As more and more aggregates are formed with time, the system becomes increasingly reactive, eventually equilibrating because the monomer concentration reaches a critical value. The expression of the monomer/aggregate concentration [M] at time *t* in this model is:

$$\frac{([M]-[M_0])}{([M_0]-[M_\infty])} = 1/(1+(m-1)\{k_0\, t + (n-1)^{-1}\,(k_c t)^{n+1}\})^{1/(m-1)} \qquad (12),$$

in which $[M_0]$ is the initial concentration, $[M_\infty]$ is the equilibrium concentration, k_c is the rate constant for the catalytic pathway, k_0 for the uncatalyzed pathway, *n* a parameter that describes the growth of the fractals, and *m* a parameter that is related to the size of the critical nucleus. The complete derivation is an exact solution to the following rate equation and is given in ref [37].

$$\frac{d[M]}{dt} = -k \cdot \frac{([M]-[M_0])}{([M_0]-[M_\infty])} \qquad \text{with} \qquad k = k_0 + k_c \cdot (k_c t)^n \qquad (13).$$

2.6.2 Fitting the aggregation kinetics

To look at the applicability of the given models on the $TPPS_3$ system, data should be fitted by these models. For the Pasternack model, equation (12) should be fitted to the aggregation kinetics data to obtain values for the parameters k_0, k_c, *m* and *n*. For both the isodesmic and cooperative model, rate equations should be formulated. As an illustration, equations (14) and (15) give the basic coupled differential equations for the cooperative model, representing the scheme in figure 2.12b. These are differential equations for the monomer concentration *[M]* and the aggregate concentration *[A]*. Values for the different rate constants from figure 2.12 can be obtained, and these differential equations can be altered in any preferential way to improve the fit, e.g. by adding extra parameters.

$$\frac{d[M]}{dt} = -k_0 \cdot [M] - k_1 \cdot [M][A] + k_2\,[A] \qquad (14).$$

$$\frac{d[A]}{dt} = k_0 \cdot [M] + k_c \cdot [M][A] - k_2[A] \qquad (15).$$

Matlab software is used to numerically calculate the outcome of these differential equations for different sets of parameters. An error function is defined as equation (16) and the function *fminsearch* is used to minimize this error function, resulting in a best fit with values for all parameters.

$$E = \sum_i \left(M_{model}(t_i) - M_{data}\,(t_i)\right)^2 \qquad (16).$$

Fminsearch is a function that finds the minimum of an unconstrained multivariable function using a derivative-free method, the simplex search method of Lagarias et al. [38]

Figure 2.13 shows simulations of the monomer- and aggregate concentrations (arbitrary units) of the three discussed models with respectively straight and dashed lines. The isodesmic model is shown in blue, the cooperative model is shown in red and the Pasternack model is shown in green. The isodesmic model does not have a nucleation period, while the other two models do. In addition, the Pasternack model has a slower reaction rate at the later stages relative to the cooperative model when similar nucleation kinetics is simulated.

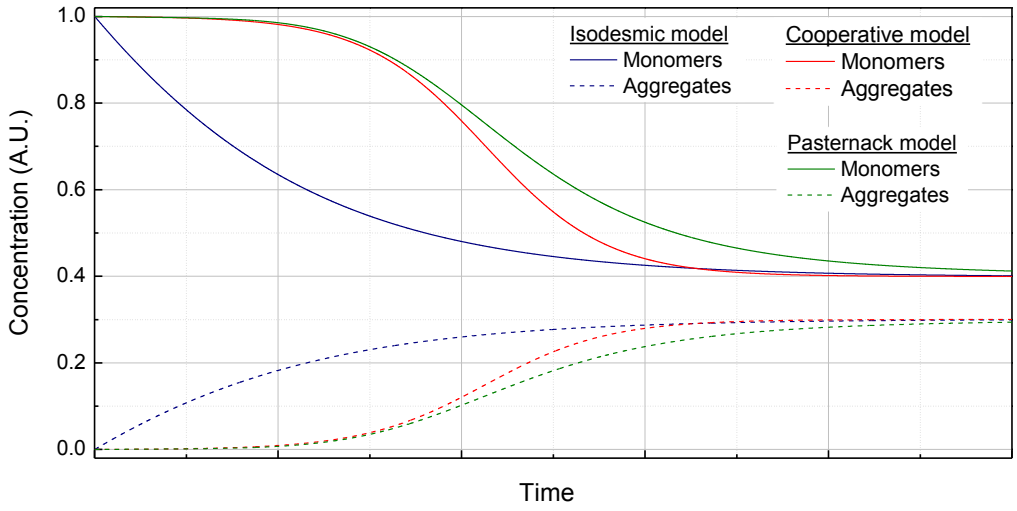

Figure 2.13 Simulations of the different growth models. The concentration of the monomers (straight) and aggregates (dashed) are shown as a function of time for the isodesmic model (blue), cooperative model (red) and Pasternack model (green).

3 Experimental methods and materials

3.1 Experimental setups for absorbance measurements

Three different setups, described below, are used for absorbance measurements in this research.

3.1.1 Setup 1. Characterizing absorbance measurements

For quick absorbance measurements, such as characterizing the absorbance of the monomers and aggregates, a setup depicted in figure 3.1 is used. A halogen light source from *TOP Sensor Systems* is coupled into an optical fiber. With a fiber lens and a pinhole, the light is focused on the sample as a circular spot of 1.5 mm in diameter. The transmitted light is coupled into a second optical fiber by the use of an optical fiber lens. This optical fiber is connected to an *Avantes Fiberoptic Spectrometer* which is controlled by *OOIBase32 Spectrometer Operating Software* on a personal computer.

For characterizing the monomers and aggregates and performing trial kinetics, the sample in this setup is put into a *Hellma* quartz cuvette. This setup is also used to measure the stationary control experiments for the aggregation kinetics in a magnetic field. In this case the sample solution is put into a clear glass screw top cylindrical vial that is secured by a Teflon ring inside a 20x20mm homemade cuvette filled with water in order to reduce refraction at the vial surface.

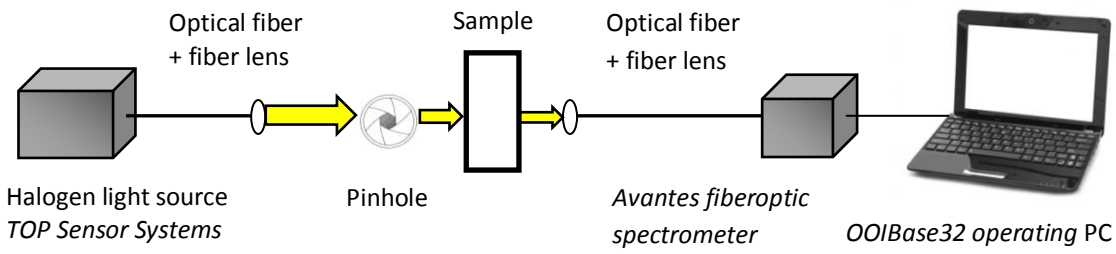

Figure 3.1 Schematic view of experimental setup 1 for quick absorbance measurements.

3.1.2 Setup 2. Absorbance measurements of a rotating vial

To probe the influence of rotation on the aggregation kinetics, a setup capable of measuring absorbance of a rotating solution is built. Figure 3.2 shows this setup in a schematic view (a) including a more detailed description of the sample holder (b) and figure 3.3 shows pictures.

The basic futures of an absorbance measurement setup, like setup 1, are also present in experimental setup 2. A halogen light source, *Avantes AvaLightHal*, couples light into an optical fiber. A fiber lens together with a pinhole focusses the light as a circular spot (1.5mm in diameter) on the middle of a sample vial inside the sample holder. Between the pinhole and the sample holder a mechanical shutter is placed to prevent illumination of the sample at all times. The shutter is connected to a *National Instruments (NI) output board*, which is connected to a personal computer. After the sample, the transmitted light passes through a combination of filters and is then coupled into an *Ocean Optics USB2000+ spectrometer* by use of a fiber lens and optical fiber. The halogen light source together with the filters C3C20 and C3C22 provide light with a spectrum ranging from 400-560 nm, see figure S2. The filters are used to get a higher sensitivity around 400 nm and also to avoid second order interference inside the spectrometer. The spectrometer is connected to a computer.

A homebuilt *Labview* script controls both the shutter and spectrometer to measure absorbance spectra at fixed times and save the data to text files. The special features of experimental setup 2 are in the sample holder, which is described next.

The sample is put into a clear glass screw top vial which is held on the cap by a Teflon cylinder connected to a rotator. This rotator can rotate the vial up to 2000 rpm (33 Hz) in both clockwise (CW) and anticlockwise (ACW) direction. A stroboscope is used to set the rotation frequency within 0.5 Hz accuracy. To control the temperature of the sample, the vial is put into a so called *Copper Cuvette Temperature Bath.* This temperature bath consists of a 20x20x30mm glass cuvette filled with water, surrounded by a copper cuvette with four windows connected to a copper disk. All components of the *Copper Cuvette Temperature Bath* are glued together with *Dow Corning 340 Heat-Sink Compound*, to get optimal heat transfer. A water circulator, set at a desired temperature, circulates water through the copper disk. This way the water inside the *Copper Cuvette Temperature Bath* will have the same temperature as the water from the circulator and will keep the sample at the desired temperature. A PT100 thermometer was used to measure the temperature of the water inside the *Copper Cuvette Temperature Bath.*

A second, more important, reason of the vial being put into a glass cuvette filled with water is to reduce the scattering and refraction from the vial surface when the vial is rotating. With the vial being cylindrical, the incident light is not perpendicular to the vial surface at all positions of the light spot. Therefore there will be refraction of the incident light from air to glass and from glass to the sample solution. Both refractions will also occur for the transmitted light. This double refraction causes the spot of the transmitted light to be non-circular and its position shifts. By putting the vial inside water, the refraction becomes less since the refraction index of water is closer to the refraction index of the glass and to the refraction index of the sample. The transmitted light spot will shift less and stays in shape. Especially for rotating vials this setup is needed because any small precession of the vial causes the transmitted light spot to move, and unable to detect at all times.

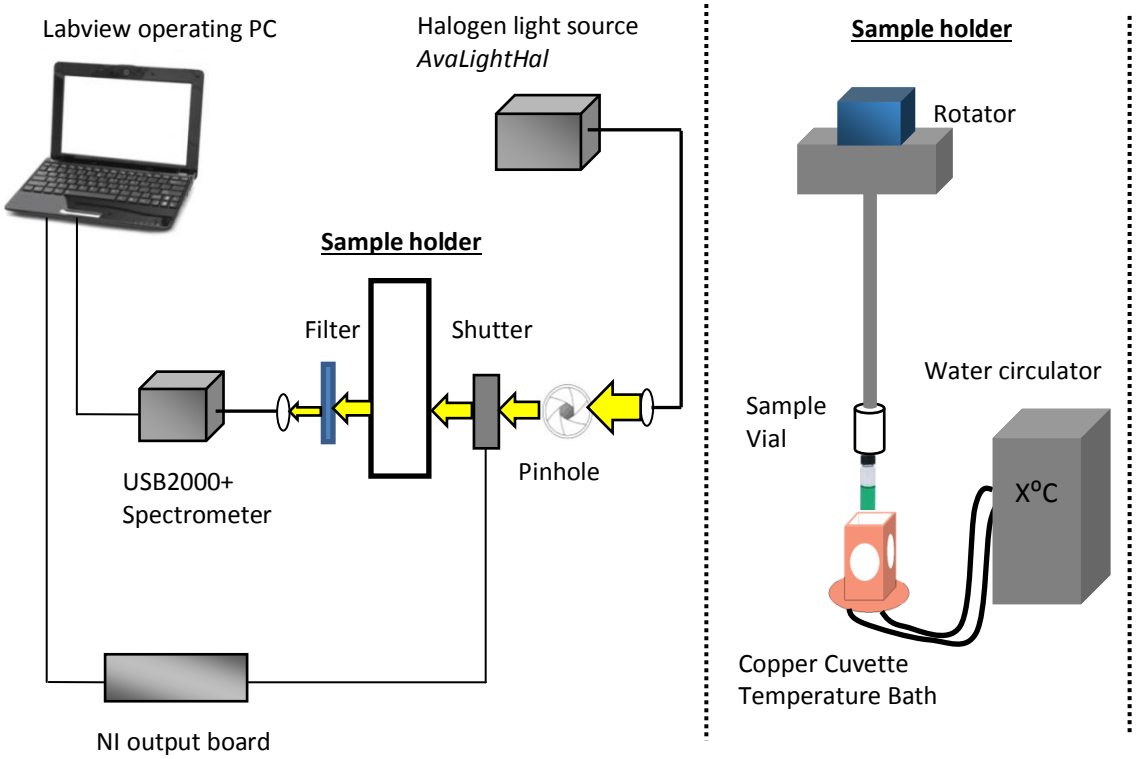

Figure 3.2 Schematic view of experimental setup 2 for absorbance measurements of a rotating vial. A schematic view of the total setup is given in (a) with a magnification of the sample holder (b).

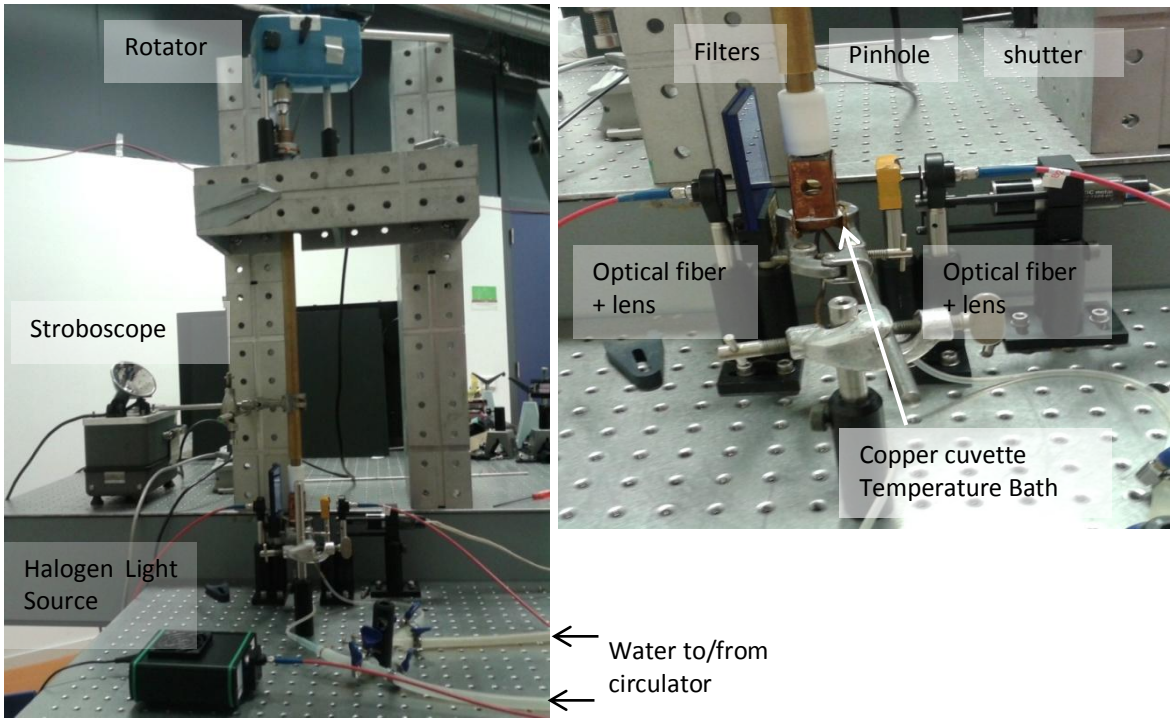

Figure 3.3 Pictures of experimental setup 2. Experimental setup 2 is used for absorbance measurements of the aggregation kinetics in a rotating vial.

3.1.3 Setup 3. Absorbance measurements of a rotating vial in a magnetic field

To measure the absorbance of a rotating vial in a magnetic field a similar setup as setup 2 is built to fit inside a 50 mm bore 30 T Bitter magnet at the High Field Magnet Laboratory at the Radboud University Nijmegen. The magnetic field strength is set by the electrical current. The magnetic field profile and extra specifications are given in supplemental material S3.

A temperature tube, connected to a water-circulator, is placed inside the magnet to keep the inside of the tube at a constant temperature. Inside this temperature tube, an experimental setup was mounted to measure absorbance spectra of a rotating vial with and without a magnetic field of 25T. The magnetic field is parallel to the axis of the magnet. The part of the experimental setup that is inside the magnet is referred to as 'insert'. The insert consists of two separate parts; the upper part which rotates the vial and the lower part which is used for the actual absorbance measurements. These parts have no mechanical connection to prevent any motion of the absorbance measurement part. Figure 3.4 shows the design of the insert at several levels. Pictures of the setup are shown in figure 3.5 and figure S4.

A rotator is put about half a meter above the magnet on an optical table and is connected to the vial via two extension tubes. The first extension tube transfers the rotation from the rotator to the top of the temperature tube where it is fixed to another extension tube. This second extension tube (nr. 1) has bearings at the bottom (nr. 3) and will transfer the rotation to an aluminum connector (nr. 4). This aluminum connector holds a nylon tube (nr. 10) in which the vial (nr. 12) is secured by the sides of the glass, to minimize any precession. The length of the nylon tube and extension tube are such that the bottom of the vial is 2 mm below the center of the magnetic field. In the center of the magnetic field the field gradient is zero which means the effective gravity is equal to the normal gravity. Since the field center is constant over about 20mm (figure S3), the entire solution in the vial experiences normal gravity.

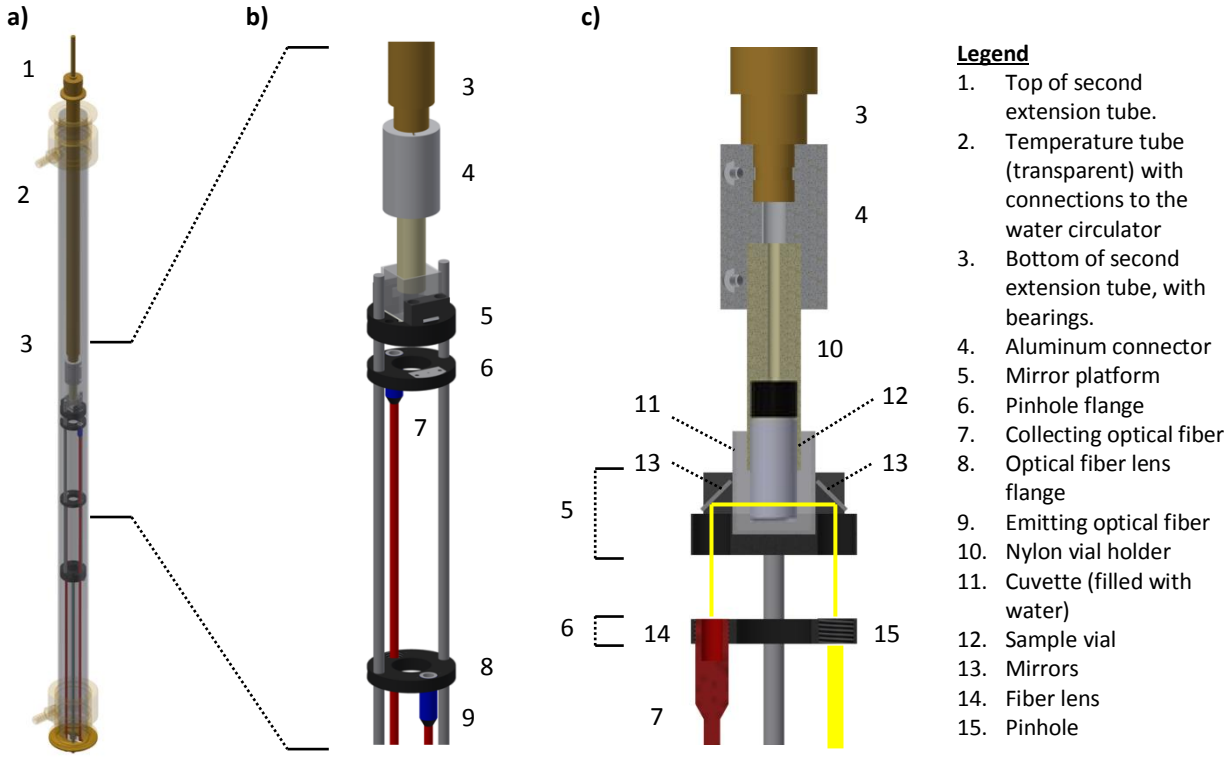

Figure 3.4 Schematic view of the insert in experimental setup 3. The insert consist of two separate parts, an upper part for the rotation of the vial and a lower part for the absorbance measurements. The part inside the magnet is shown in (a) with a close-up (b) and a cross-section (c) including the light path (yellow).

The lower part of the insert is the part for measuring absorbance spectra. This part of the insert consists of a platform (nr. 5) on which a glass cuvette filled with water (nr. 11) is mounted. This water-filled cuvette is necessary to reduce the scattering and refraction of the incident light on the surface of the vial. On the sides of the water bath, two mirrors at an angle of 45^{o} with the platform are placed. Two fibers are mounted in the insert to collect and emit light, respectively nr. 7 and nr. 9. For the fiber emitting the light (nr. 9), a small optical setup outside the magnet is used (figure 3.5c). A halogen light source, *Avantes AvaLightHal,* couples light into a fiber and this light passes through a shutter and the C3C-22 and C3C-20 filters. The light is then coupled into an optical fiber by use of a fiber lens. This fiber has an optical fiber lens at its end and this is mounted in the insert at the optical fiber lens flange (nr. 8). The fiber emits light vertically with a wavelength range of 400-560 nm. The path of the light is shown as a yellow line in figure 3.4c. The light passes a pinhole (nr. 15) mounted in the pinhole flange (nr. 6), and is then reflected by a mirror (nr. 13). The light passes through the water and the sample (nr. 12) horizontally (perpendicular to the magnetic field). The spot size of the light on the vial is about 0.5mm in diameter. The transmitted light is reflected downwards by the second mirror and collected by a fiber lens (nr.14) which is also mounted on the pinhole flange. The fiber lens couples the light into the second optical fiber (nr. 7). This optical fiber is about 10 meters long and transfers the light to the USB2000+ spectrometer, located outside the magnet. The USB2000+ is connected to the computer and homebuilt *Labview* script controls both the shutter and spectrometer to measure the absorbance at fixed times and save the data to text files.

For a few experiments a calibrated PT100 thermometer was mounted in the lower part of the insert to measure the temperature at all times during the aggregation process.

Figure 3.5 Pictures from total experimental setup 3 (a), with magnifications of the rotation part with extension tube 1 (b) and the optical part outside the magnet (c). In c), light from a halogen light source passes a shutter and filters after which it is coupled into a fiber again which goes into the magnet and is mounted on the insert. More pictures are shown in supplemental material S4.

3.2 Standard aggregation protocol and measuring procedures

3.2.1 Standard aggregation protocol

The aggregation of $TPPS_3$ monomers into J-aggregates is a highly sensitive process. Therefore a standard protocol has been developed in order to get the same initial conditions for each aggregation experiment. Four different solutions are used for the aggregation of $TPPS_3$, summarized in table 3.1. The clear glass screw top vials and caps are cleaned before use with demi-water and 99.8% *alcohol absolutus* from *Nedalco*.

Table 3.1 Solutions used for the aggregation of $TPPS_3$

Solution	Molarity	Details and origin
Acid (Sulfuric Acid (H_2SO_4) in MilliQ)	1.0 M	Sulfuric Acid pro analysi (95-97%), Merck
Salt (NaCl in MilliQ)	1.0 M	Sodium Chloride pro analysi (99.5%), Merck
MilliQ	-	Department of Bio-Organic chemistry, IMM, RU
Porphyrins($TPPS_3$)*	0.3mM	Synthesized by *I. Occhiuto*, Department of Molecular Materials, IMM, RU

* Two different batches of $TPPS_3$ are used of which the dilutions with molarity 0.3mM are made. Both batches are from the same crystal $TPPS_3$ which was synthesized by *I. Occhiuto.*

The standard aggregation protocol:

- Add 16.7 µL of 0.3mM porphyrin solution to 870µL of MilliQ.
- Mix the porphyrins and MilliQ well using the micropipette
- Add 13.3 µL 1.0 M sulfuric acid solution and mix it gently using the micropipette
- Add 100 µL 1.0 M salt solution and mix gently using the micropipette (timing starts now)

The final concentrations of the salt, acid and $TPPS_3$ are respectively 0.1M, 0.0133M and 5µM. In the experiments by Micali et al.[1] the $TPPS_3$ concentration was between 3 µM and 4 µM. In these experiments 5 µM was used instead to increase the speed of the aggregation in order to save time.

The porphyrin solution used in the aggregation protocol (table 3.1) is a dilution of a $TPPS_3$ batch. In this research, two different batches of $TPPS_3$ are used. Both batches are made from the same crystal $TPPS_3$ synthesized by *I. Occhiuto* from the department of Molecular Materials at the Radboud University Nijmegen. For Batch 1, the crystal $TPPS_3$ is dissolved in MilliQ and refluxed for one hour. This batch is made in February 2012 with a final concentration of 1.95mM $TPPS_3$. For every 10 experiments a new dilution of 0.3mM $TPPS_3$ is made from batch 1. Batch 2 has a concentration of 2.0mM and is made in April 2013. Again the crystal $TPPS_3$ is dissolved in MilliQ, but this time the batch is not refluxed. Two dilutions of 0.3mM $TPPS_3$ are made from batch 2, referred to as batch 2a and 2b.

The sulfuric acid and salt solution were made for a longer period and are always checked for contamination (e.g. dust) before use.

For the characterization experiments the same protocol is used with similar solutions. The concentrations and amounts (µL) are varied to probe the influence of the concentrations and mixing volumes of the reagents.

3.2.2 *General absorbance measurement procedure*

Equation (1) gives the equation for the absorbance of a sample. The decrease of light intensity by a solution is however not only due to absorbance, but also to scattering. The quantity that describes the total reduction in light intensity is called *'extinction'.* In this research the term *'absorbance' is* used although technically extinction measurements are performed. The scattering of the obtained solutions is however negligible, meaning the extinction and absorbance of the solutions are practically the same and equation (1) holds.

In light intensity measurements, the spectrometer always gives a background intensity I_{dark} because of the electrical circuit. To achieve a better sensitivity in the absorbance, this background should be subtracted from both the measuring intensity I and the reference intensity I_0. The resulting equation for the absorbance A is given in equation (17).

$$A = -\log_{10}\frac{I-I_{dark}}{I_0-I_{dark}} \qquad (17).$$

For absorbance measurements, hence, first a dark intensity spectrum and a reference intensity spectrum have to be measured. Before adding the $TPPS_3$ a dark intensity spectrum will be taken with a closed shutter and a reference intensity spectrum will be taken of the MilliQ inside the sample vial. Then the aggregation procedure can start and absorbance spectra can be acquired.

3.2.3 Procedure for probing the influence of rotation

In the experiments investigating the influence of rotation on the aggregation kinetics, porphyrin dilutions of batch 1 are used. In the experiments, first the standard aggregation protocol is performed. After adding the salt, the vial is mounted in experimental setup 2, and the rotation is started. The frequency of the rotation is set at (15 ±0.5) Hz.

The absorbance measurement program is started at the same time as the rotation. A stopwatch is used to measure the time between the moment of adding the salt and enabling the rotation. This time is afterwards added to the kinetic data. After one hour, the rotation is turned off. The absorbance measurements run for another 4.5 hours. Afterwards the vial is removed from the setup and stored at room temperature.

3.2.4 Procedure for probing the influence of the magnetic field

For the experiments probing the influence of the magnetic field on the aggregation kinetics, porphyrin batch 2a and 2b are used. The procedure of the measurements is as follows.

First, the magnetic field is set to 25 T by sweeping up with 80mT/s. The aggregation procedure is performed once the magnetic field reaches 25T. The sample is mounted into the insert and simultaneously the rotation and absorbance measurement program are started. A stopwatch is used to measure the time between the moment of adding the salt and enabling the rotation. This time is afterwards added to the kinetic data. After one hour the magnetic field is swept down from 25T to 0T with a speed of 100mT/s. When the magnetic field reaches 0T, the rotation is turned off, this is after about 3850 s. The absorbance measurements run for another 4.5 hours. Afterwards the vial is removed from the setup and stored at room temperature.

3.3 Circular dichroism experiments

3.3.1 Circular dichroism measurements for aggregation kinetics experiments

For each aggregation, a CD spectrum was measured *ex situ* three days after starting the aggregation. The circular dichroism experiments are performed in a *Jasco J-815 CD spectrometer*. Temperature is set at 23 ^{o}C and 1 ml of sample is transferred to a Hellma quartz SUPRASIL cuvette. A spacer is used to place the cuvette at the desired height in the CD spectrometer. Table 3.2 displays the configuration settings of the spectrometer. Both absorbance and circular dichroism are measured. This procedure avoids any artifacts that may arise from the material sticking to the wall of the vial and measures the true supramolecular chirality of the J-aggregates at rest.

Table 3.2 Configuration of the *Jasco J-815 CD spectrometer*

Parameter	**Value**
Speed	200 nm/min
Data pitch	0.5 nm
Channels	2 (absorbance and CD)
Wavelength range	400 nm - 550 nm

3.3.2 Circular dichroism measurements for aggregate thermodynamics

The temperature dependence of the equilibrium is investigated by measuring absorbance and circular dichroism of equilibrated samples at different temperatures. Four days after the start of the aggregation, the sample is transferred to a Hellma quartz SUPRASIL cuvette and measured in a *Jasco J-815 CD spectrometer.* The temperature of the cuvette including solution is varied from 20^{o}C to 60^{o}C and spectra are taken at intervals of 10 minutes with the same configuration settings as in table 3.2.

3.4 Fluorescence experiments

A solution of purely the diacid of $TPPS_3$ and an equilibrated aggregation solution are transferred to a fluorescence cuvette and fluorescence measurements are performed in a *LS-55 fluorescence spectrometer*.

4 Results

4.1 Characterization $TPPS_3$ monomer and aggregates

The different forms of $TPPS_3$ (free base, diacid, H-aggregate, J-aggregate) can be distinguished by their absorbance spectrum. The aggregates can be further analyzed by circular dichroism experiments. Circular dichroism shows the enantiomeric excess of a solution containing aggregates and the signal is related to the electronic coupling between the monomers inside the aggregates.

4.1.1 Absorbance (and fluorescence)

Figure 4.1 shows the absorbance spectra of the free base form of $TPPS_3$ (a), the diacid form (b) and the aggregates (c) from 400 to 550 nm together with pictures of the solutions. The solutions in these pictures contain 5µM $TPPS_3$. The Soret band of the free base $TPPS_3$ has a maximum at 413 nm. When the pH of this solution is brought down to 1.9, the diacid appears in the absorbance spectrum. The Soret band of the diacid $TPPS_3$ shifts towards 434 nm. After aggregation, both H- and J-aggregates are observed. The H-aggregates have an absorbance maximum at 420nm and The J-aggregates have an absorbance maximum at 489nm.

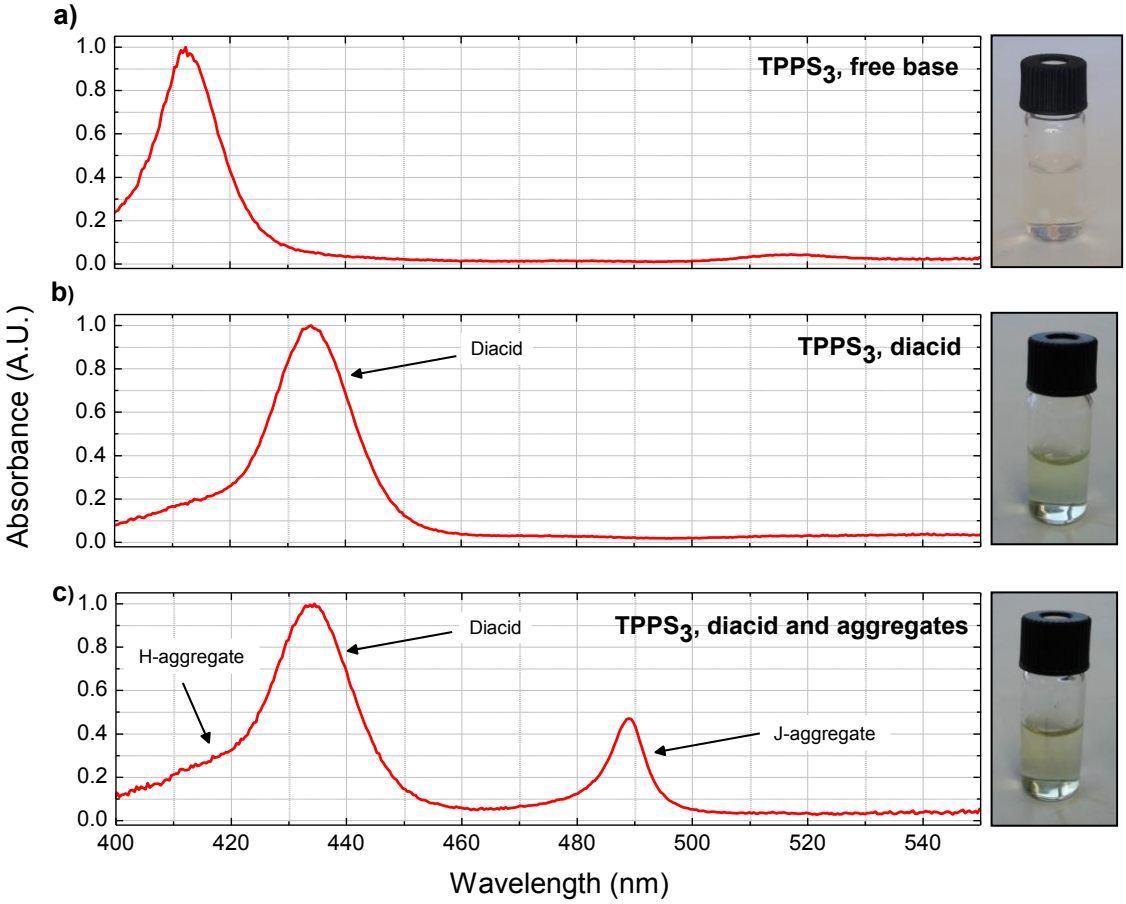

Figure 4.1 Absorbance spectra of $TPPS_3$ in the free base form (a), diacid form (b) and the aggregates form (c). Pictures of the solutions are shown on the right.

In the aggregation kinetics experiments filters of 400-560 nm are used, there is however absorbance above 560 nm. Figure S5 shows the absorbance spectra of $TPPS_3$ up to 800 nm. The diacid form of $TPPS_3$ shows fluorescence at 665 nm when excited with 435nm. The J-aggregates show no fluorescence at all (figure S6).

4.1.2 Circular Dichroism

Both H- and J-aggregates are found in the circular dichroism spectra. The J-aggregates are the aggregates of interest so the CD signal at 489nm is used in further analysis. The shape and position of the CD signal depends on the conditions under which the aggregates are formed. Figure 4.2a shows typical CD signals for both enantiomers formed in: a stationary vial without magnetic field (top figures), a vial rotating at 15 Hz for one hour without applying a magnetic field (middle figures) and a vial rotating at 15 Hz in presence of a magnetic field of 25T for one hour (bottom figures).

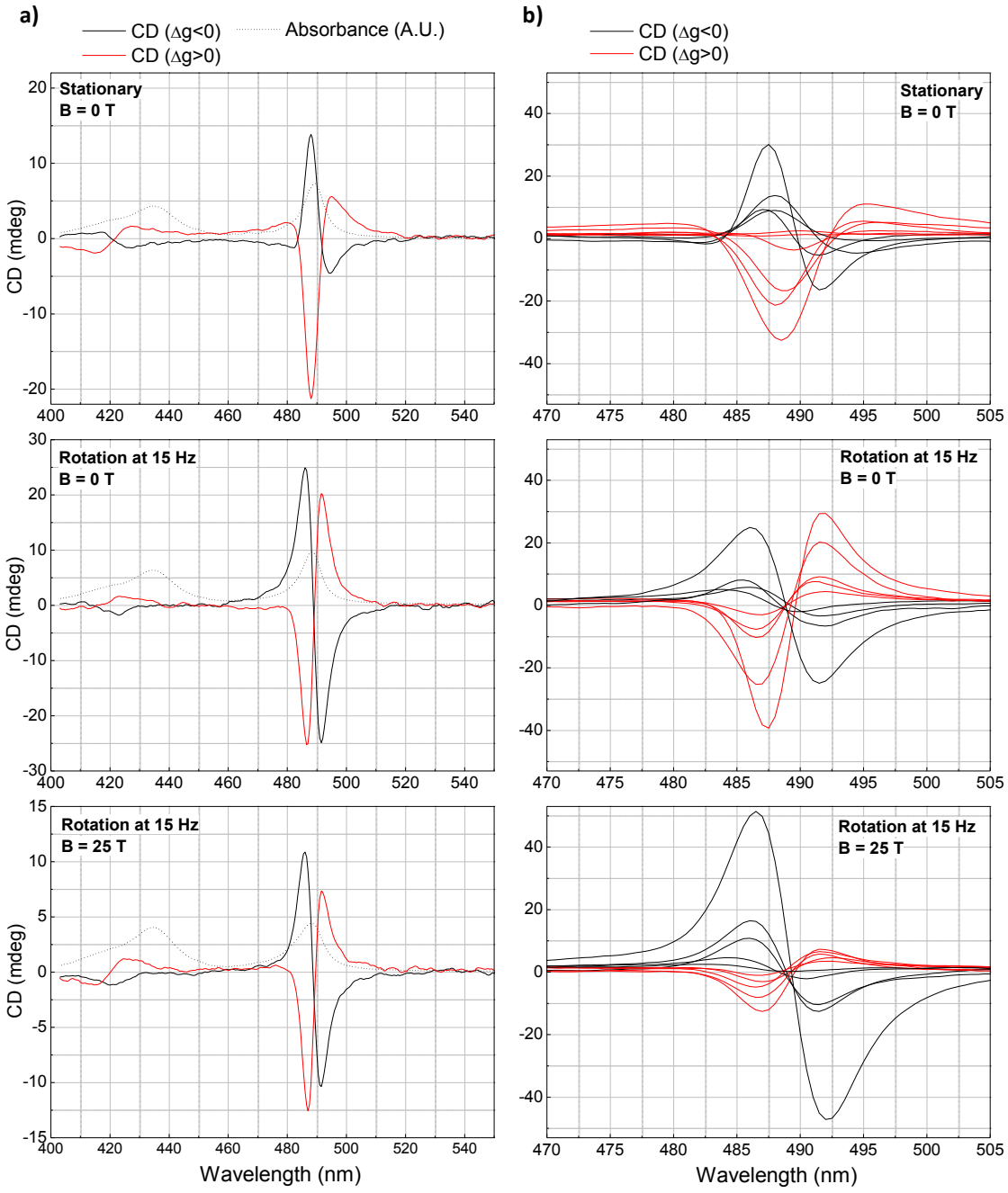

Figure 4.2 Ellipticity (CD) signals of the J-aggregates of $TPPS_3$ formed under different conditions. Typical CD spectra are shown for different conditions (a) and corresponding multiple CD spectra are shown in (b) to see the consistency in the aggregations. The top figures show spectra of aggregates formed in stationary vessels without a magnetic field. The middle figures show CD spectra of aggregates formed in rotating vials (15 Hz) without a magnetic field and the bottom figures shows CD spectra of aggregates formed in rotating vials (15Hz) in a magnetic field of 25 T. In a) also the corresponding absorbance spectrum is shown (dotted lines).

Bisignate CD signals are observed for the J-aggregates. The shape of the signal is however different for the different aggregation conditions. For aggregates formed in stationary vials without a magnetic field, highly asymmetric CD signals with respect to the absorbance maximum are observed. For aggregates formed under rotation conditions (with and without magnetic field) the signals are more symmetric with respect to the absorbance maximum.

Also the consistency in the CD signals of the aggregates is different for the different aggregation conditions (figure 4.2b). When external physical forces are applied, the position and shape of the CD signals is more consistent. Rotation conditions, both with and without a magnetic field, yield a very good consistency. Aggregates formed under stationary conditions show on the other hand a bad consistency. The absorbance maxima are equal for these experiments, but the position of the maxima, minima, and zeros of the CD signals show a large variation.

The CD signal of the aggregates is developing during the aggregation process. The magnitude, shape and position are changing in time. The development is followed for a sample that was rotated at 15 Hz for one hour without applying a magnetic field at 23^{o} C. After three hours the sample was transferred to a quartz cuvette and at several times a CD spectrum was measured. The development of the magnitude of the CD signal is shown in figure 4.3a by plotting Δg against the time. After about 60 hours, the signal looks saturated.

The development of the shape and position of the same sample is shown in figure 4.3b. Figure 4.3b shows the CD signal normalized on its absorbance (*g)* against wavelength for several times. After 72 hours it looks saturated. It should be noted here, that these measurements over time are not that smooth. Over time, the absorbance curves showed bumps around the 475nm, influencing the rest of the spectrum as well. The aggregates probably interact with the walls of a quartz cuvette. These figures do however give an indication of the development of the CD signal.

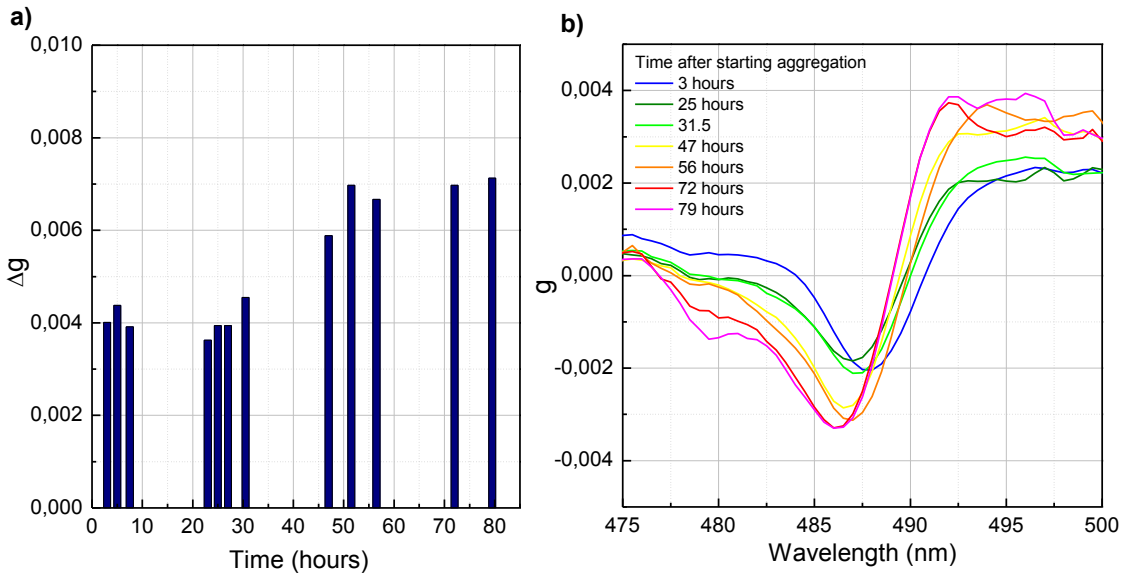

Figure 4.3 The development of the CD spectrum of the aggregates formed under rotation conditions. The development of the magnitude of the CD signal is shown by plotting Δg as a function of time (a) and the development of position and shape is shown by plotting the CD spectra (normalized on the absorbance) in b).

4.2 Aggregation kinetics and chiral selection

4.2.1 Characterization of the aggregation kinetics

The aggregation kinetics of $TPPS_3$ is a statistical and highly sensitive process. The procedure of mixing and the concentrations of the different reagents have a big influence on the kinetics of the aggregation. The influence of several parameters has been explored and is given in supplemental material S7.

Kinetic spectra are measured by following the time trace of the absorbance at different wavelengths: 435 nm for the diacid monomers and 489 nm for the J-aggregates. It is chosen to trace the diacid monomers at a wavelength of 435nm although the absorbance maximum is at 434 nm. This has two different reasons. First, the maximum of the Soret band in figure 4.1 is the sum of both the diacid absorbance and the H- aggregate absorbance. The absorbance maximum of the diacid monomers is thus at a somewhat higher wavelength. Secondly, the noise close to the absorbance maximum is less than on the maximum itself, probably due to resonant light scattering.

Figure 4.4 shows a typical kinetic trace of both the monomer- and aggregate absorbance. The aggregate absorbance over time was often bumpy like in figure 4.4 (grey). Moreover, the equilibrium absorbance of the aggregates varies a lot for aggregations under equal conditions and it is also seen that the aggregates stick to the walls of the vial. These observations indicate that the aggregates are not distributed homogeneously in the solution (supplemental material S8) which is troublesome for the analysis. The analysis of the aggregation kinetics is therefore performed on the absorbance trace of the monomers (diacid). The kinetics of the monomers should be similar since these monomers form the aggregates. The loss of monomer therefore resembles the forming/growth of the aggregates.

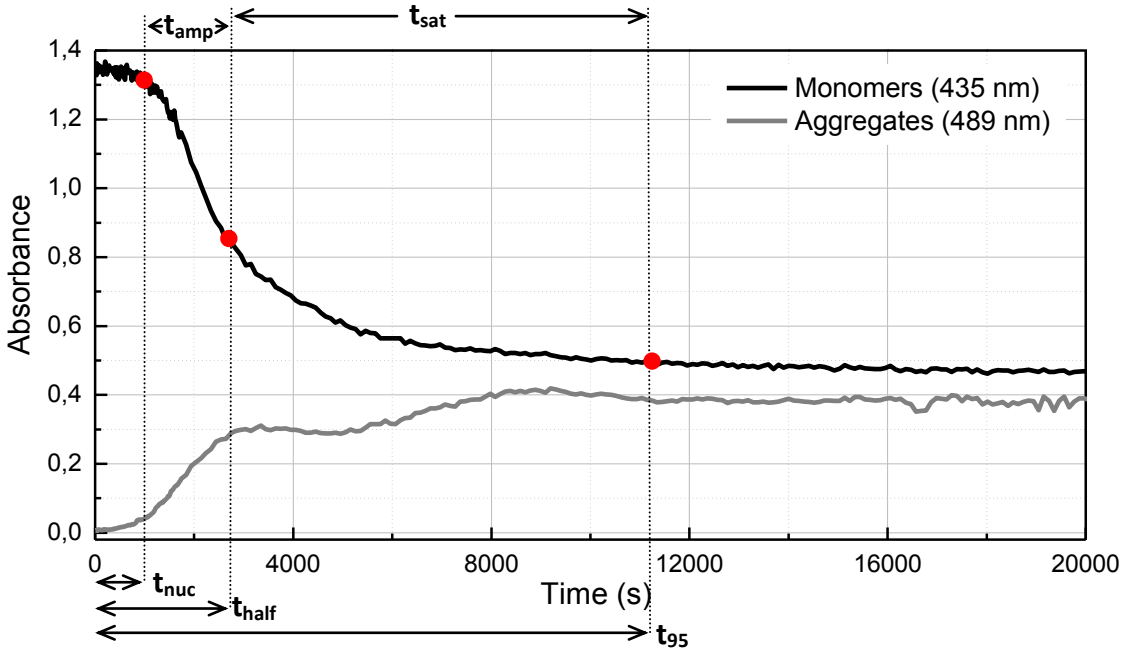

Figure 4.4 Typical kinetic traces of the monomer absorbance (black) and aggregate absorbance (grey). The characteristic times that are used to characterize the spectrum are shown on the monomer curve.

The kinetics of the monomers show roughly three different stages as seen in figure 4.4. These stages are referred to as a nucleation period, an amplification period and a saturation period, respectively shown by t_{nuc}, t_{amp}, and t_{sat}. The different models discussed in *section 2.6.1* were fitted to the kinetic spectra with *Matlab.*

The *Pasternack model*, which fitted the aggregation of $TPPS_4$[33], also fits the aggregation of $TPPS_3$. The same spectrum can however be fitted by multiple combinations of parameter values k_0, k_c, m and n. The Pasternack set of parameter values is underdetermined and can therefore not be used for analysis. The isodesmic model does not fit at all, which is expected since a nucleation period cannot be obtained by isodesmic reaction kinetics. Contrary to the isodesmic model, the cooperative model does have a nucleation incorporated. This model shows good fits for the first part of kinetic spectra (for t_{nuc} and t_{amp}) but after t_{amp} it does not fit anymore, as is shown in figure 4.5.

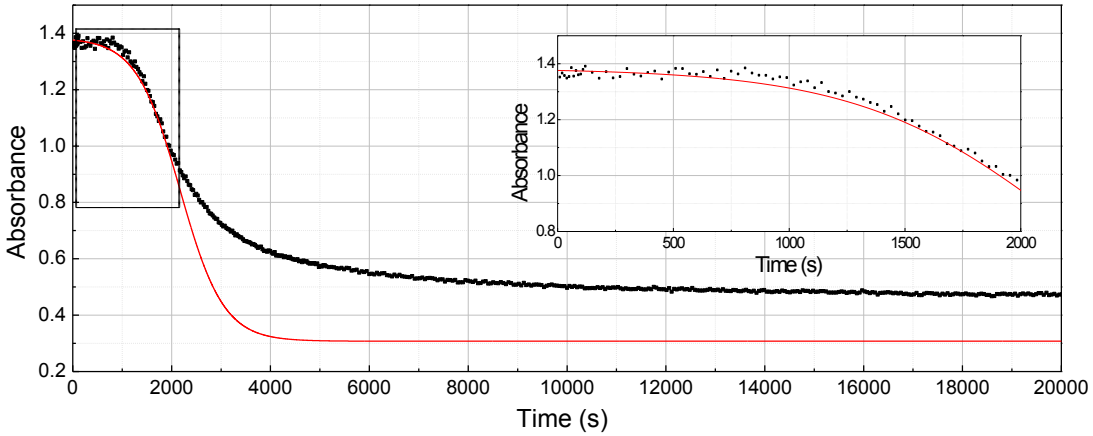

Figure 4.5 Fit of the cooperative model to the aggregation kinetics with a magnification of the first 2000 seconds in the inset.

Many different additions and changes were tried on the differential equations (14) and (15) in order to create a better fit, but none of them succeeded. To quantize the kinetic data, a characterization was therefore made by defining characteristic times. The aggregation process continues for several days, but the end time of the aggregation measurements is set at 20.000s, because the absorbance trace is almost horizontal after this time. Also absorbance values at several defined times are used in the characterization. The monomer absorbance at the beginning, M_0, is a measure of the initial $TPPS_3$ concentration. The relation between M_0 and the monomer absorbance at the end, M_∞, provides information about the thermodynamics as indicated by ΔG in figure 2.3. This difference in Gibbs free energy (ΔG) determines the equilibrium position, meaning how many monomers are present in the aggregates relative to how many free monomers are present in the solution.

To characterize the speed of the reaction, five different times are defined to characterize the different stages shown in figure 4.4. For the definition of these times, the spectrum is first normalized according to equation (18).

$$M_{Normalized}(t) = \frac{M(t) - M_\infty}{M_0 - M_\infty} \qquad (18),$$

in which $M(t)$ is the absorbance of the diacid at time t. For both M_∞ and M_0, averages of 10 data points are taken. Table 4.1 shows the definition of the five characterizing times, of which t_{nuc}, t_{amp}, and t_{sat} are used in further analysis because these three characteristic times describe the three stages of the aggregation. Figure S15 shows an example of a normalized kinetic curve including the characteristic times.

Table 4.1 Definitions of the characteristic times in the analysis of a kinetic spectrum.

Time parameter	Definition
t_{nuc}	Time for which $M_{normalized}$ is at least 5 data points in a row less than 0.98
t_{half}	Time for which $M_{normalized}$ is for the first time less than 0.5
t_{95}	Time for which $M_{normalized}$ is for the first time less than 0.05
t_{amp}	Difference between t_{half} and t_{nuc}
t_{sat}	Difference between t_{95} and t_{half}

4.2.2 Influence of rotation on the formation of chiral aggregates

In this section the influence of rotation during the aggregate formation is shown on both the kinetics and the chirality of the aggregates. For these experiments, $TPPS_3$ batch 1 is used. Figure 4.6 shows the kinetic traces (background corrected) for both stationary and rotation conditions at 23° C. The time axis is on a logarithmic scale to see the variation in the early regimes more clearly. Important to notice is that the rotation lasted only for one hour, as depicted in figure 4.6. Rotation on average increases the speed of the aggregation. The relative amount of monomers present in the solution at 20.000s is thereby lower for aggregations with rotation.

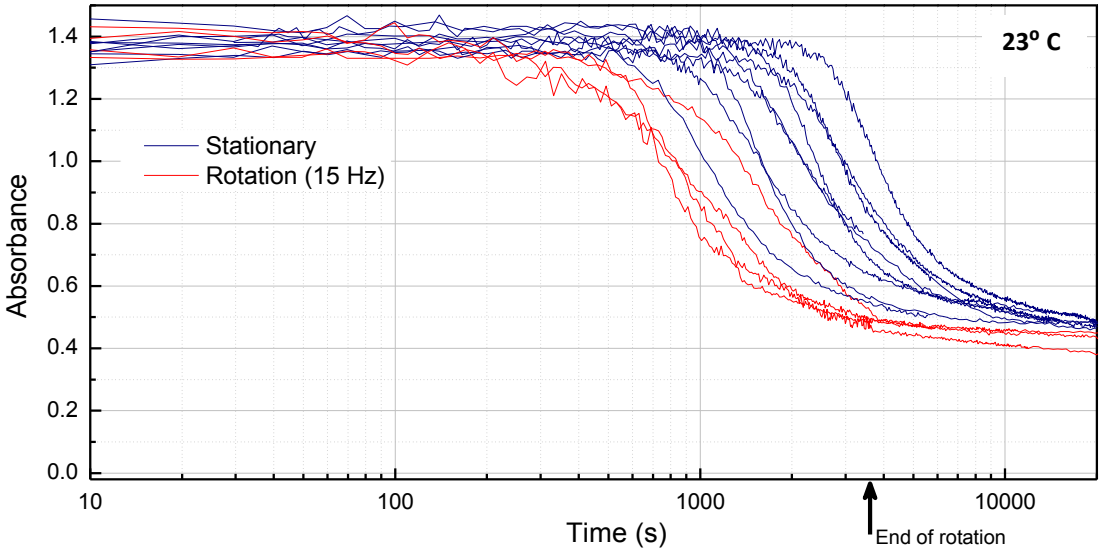

Figure 4.6 Kinetic traces of the monomers without rotation (blue) and with rotation (red) during the aggregation process at 23° C.

Analysis based on the characteristic times from table 4.1 is performed to quantify the acceleration of the aggregation kinetics by rotation. Of every single kinetic spectrum the characteristic times are determined. The averages of these times (including standard deviation) are shown for the rotation (red) and stationary (blue) conditions at 23° C in figure 4.7a. Similar graphs as figure 4.6 and figure 4.7a are observed for aggregations at temperatures of 18°C and 28°C (respectively figure S16, S18 and figure S17,S19).

Rotation increases the speed of the aggregation in all three stages. For every temperature, all three characteristic times of the aggregation are smaller for rotation conditions than for stationary conditions. The standard deviations are thereby almost always smaller than the differences in time averages and often there is even no overlap between the standard deviations originating from the averages, as for t_{amp} and t_{sat} in figure 4.7a.

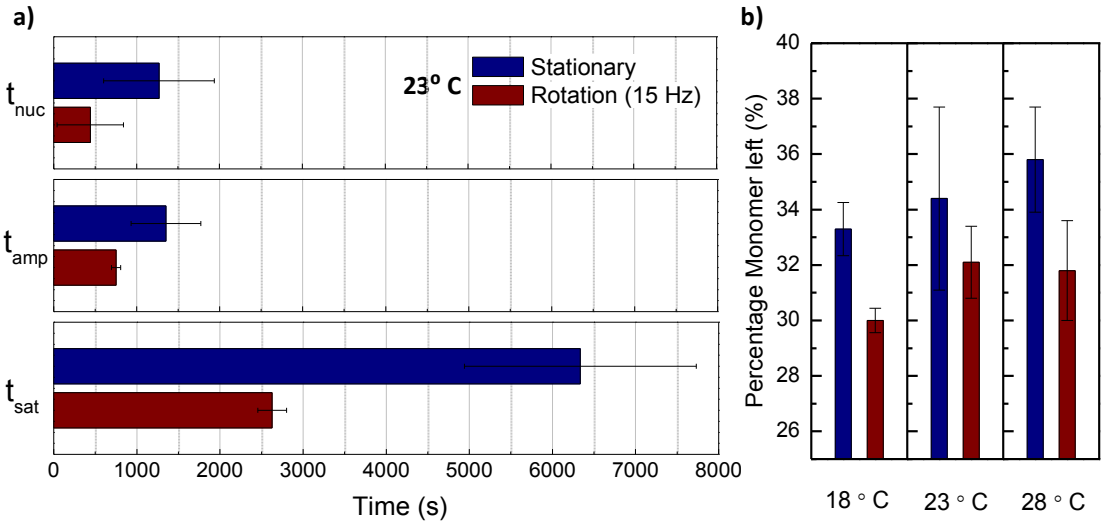

Figure 4.7 The influence of rotation on the aggregation kinetics at a temperature of 23° C expressed by the three characteristic times: t_{nuc} , t_{amp} and t_{sat}. b) The influence of rotation on the percentage of monomer left at the end of the aggregation, for different temperatures.

Figure 4.7b shows the percentage of monomer that is still present in the solution at the end of the aggregation ($M_\infty / M_0 * 100$ %) for different temperatures. The amount of monomer left is for rotation conditions on average always lower than for the stationary case. The standard deviations are thereby always smaller than the difference in average. This suggests that the aggregates formed under rotation have a different absolute configuration resulting in a larger ΔG (energetically more favorable aggregates), see figure 2.3.

Figure 4.8 shows the values of the dissymmetry factor Δg for all experiments. These Δg values show a large bias towards a positive Δg. For the rotation experiments, negative Δg values are only observed by rotating anti-clockwise.

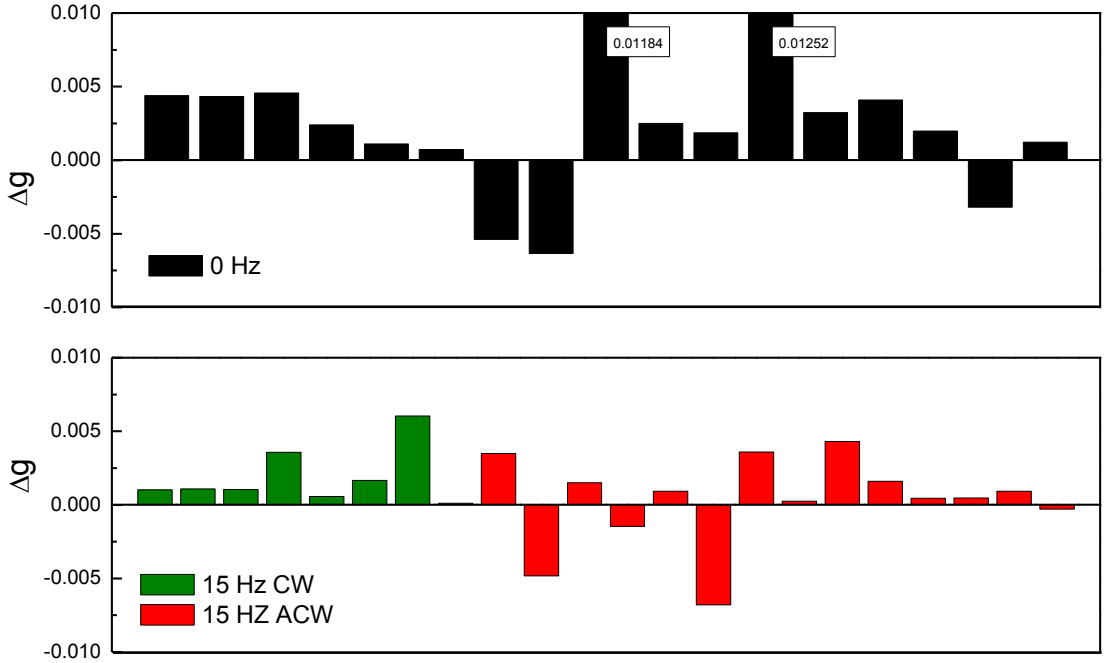

Figure 4.8 The value of Δg for all experiments for stationary conditions (a) and rotation conditions (b), either clockwise (green) or anticlockwise (red).

The time parameters derived for each experiment are plotted against the absolute value of Δg of the corresponding experiment, but no clear relations were found in these graphs, see figure S20.

Note: Influence of temperature on the aggregation kinetics

When comparing the aggregation kinetics at different temperatures it is seen that the variation in the characteristic times increases with increasing temperatures, but that the averages are equal (see figure 4.7a, S18 and S19). The percentage of monomer left is on average increasing with increasing temperature (figure 4.7b), but the variation is too big to actually confirm that these averages are actually different. It is however seen that the equilibrium position shifts by increasing the temperatures up to 60°C. Increasing the temperature results in fewer aggregates and more monomers in accordance with figure 4.7b (see figure S22).

4.2.3 Influence magnetic field on the formation of chiral aggregates

The influence of the magnetic field on the formation of chiral aggregates is investigated by measuring the aggregation kinetics while applying both rotation and a magnetic field. The vial experiences an effective gravity equal to the normal gravity. For comparison, zero-field rotation measurements are done in the same experimental setup. The temperature of the circulator was set at 23°C and the temperature inside the cooling tube remained stable (23.5±0.1°C) during the entire aggregation.

The first eleven measurements were performed with batch 2a. For batch 2a, chiral selection is observed 10 out of 11 times according to the rotation direction (figure 4.9a). The same chiral selection is found as Micali et al.[1]. Clockwise rotation together with a magnetic field yields a chiral selection resulting in a negative Δg. For anticlockwise this chiral selection is opposite, yielding a positive Δg. After these eleven experiments batch 2b was made to use for the rest of the experiments. With batch 2b no selection was observed (figure 4.9b), 9 out of 10 experiments yielded a positive Δg.

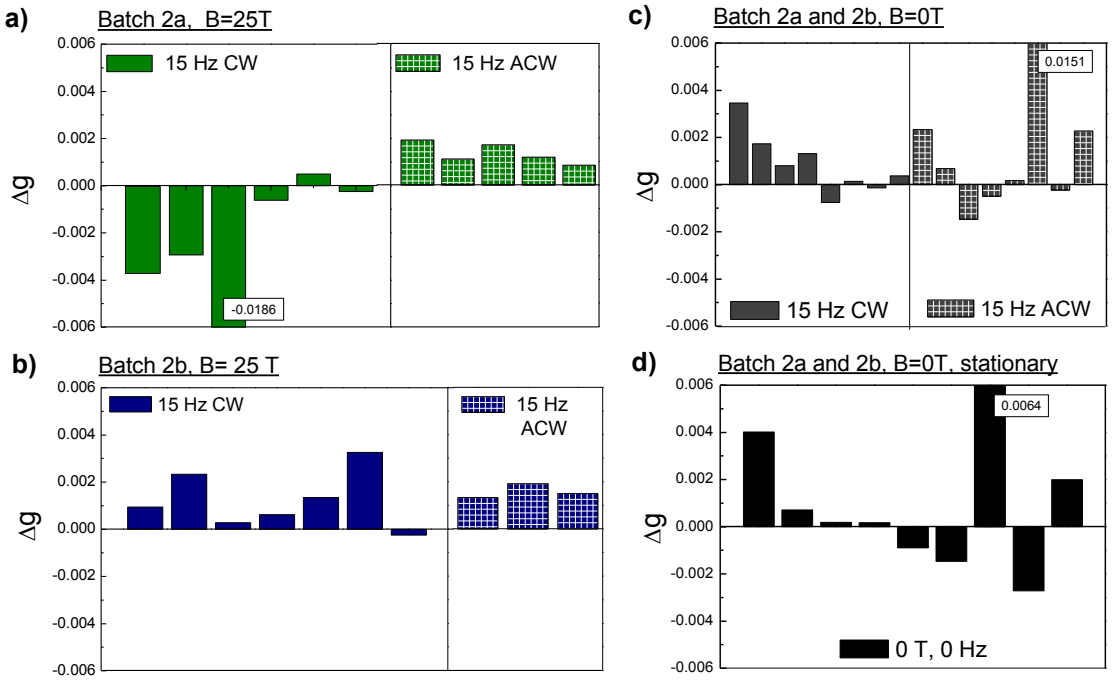

Figure 4.9 Dissymmetry parameter Δg for all experiments with batch 2. The Δg values of aggregates formed in a magnetic field of 25 T combined with a rotation of 15Hz are shown for batch 2a (a) and 2b (b). Control experiments without the magnetic field are performed for batch 2a and 2b with and without a rotation of 15 Hz for which the Δg values are shown in respectively (c) and (d).

Aggregations are also performed without a magnetic field to look at the *Δg* without chiral selection. Both batch 2a and 2b are used in these experiments and no significant differences in the kinetics are found between these batches, as shown in figure S23 for rotation conditions. The *Δg* values of aggregates formed without magnetic field and with rotation are shown in figure 4.9c and experiments without both the magnetic field and rotation are shown in figure 4.9d. Again there is a chiral bias towards positive Δg.

Figure 4.10 shows the first 6000 seconds of the normalized aggregation kinetics of the magnetic field experiments with batch 2a (red and green) and the zero field rotation experiments (blue) with batch 2a and 2b. The magnetic field experiments for clockwise (green) and anticlockwise (red) rotation are performed alternately and on several times of the day.

On average the magnetic field does not have an effect on the aggregation kinetics. The same three different stages can be identified, the characteristic times are on average equal and there is again a large variation. There is however a clear difference between the kinetics of clockwise and anti-clockwise rotation. The spectra of the magnetic field experiments with clockwise and anticlockwise rotation are shifted towards respectively the fastest and slowest of the kinetic spectra without a magnetic field.

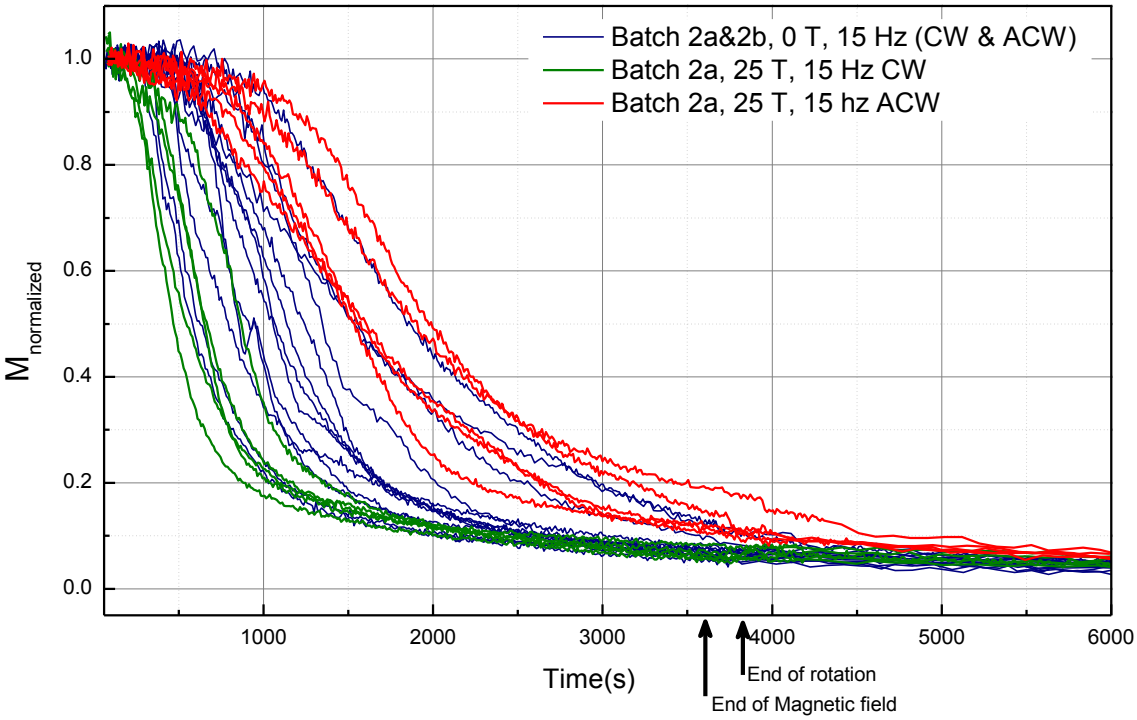

Figure 4.10 Normalized aggregation kinetics of batch 2a in a magnetic field of 25T with anticlockwise (red) and clockwise (green) rotation. Also, aggregation kinetics of zero field rotation experiments performed with batch 2a and 2b are shown in blue. When a magnetic field of 25 T is applied, chiral selection according to the rotation direction was observed. A negative Δg is obtained for clockwise rotation and a positive Δg for anticlockwise rotation. The magnetic field and rotation are switched off at the times depicted in the figure.

For the magnetic field experiments with batch 2b this difference in aggregation kinetics for clockwise and anticlockwise rotation is almost totally gone as shown figure 4.11. For the zero field rotation experiments no big difference in aggregation kinetics for clockwise- and anticlockwise rotation was found as shown in figure S24.

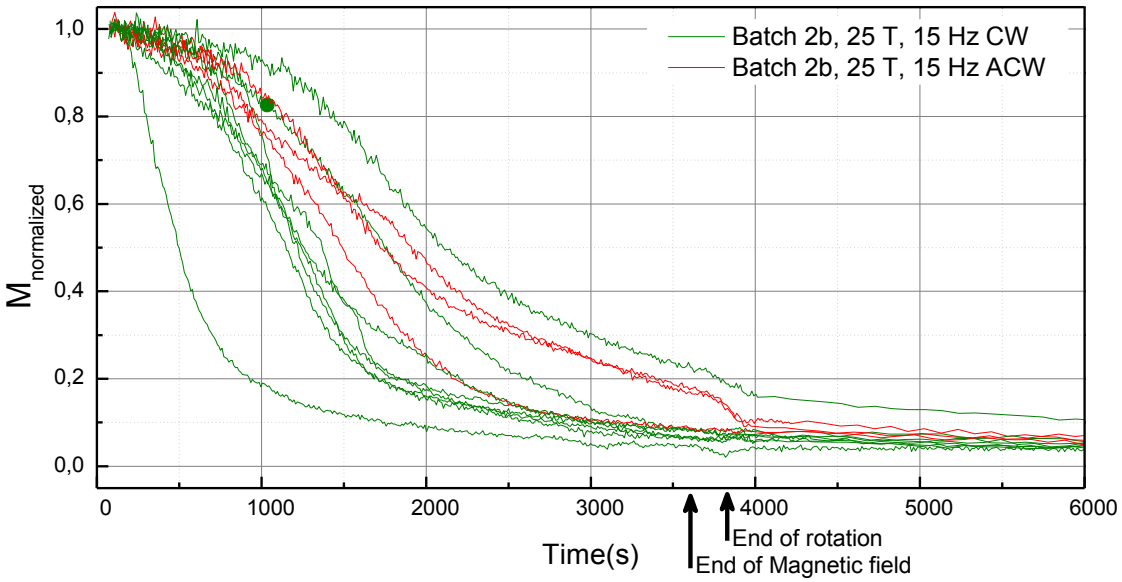

Figure 4.11 Normalized aggregation kinetics of batch 2b in a magnetic field of 25T for both clockwise (green) and anticlockwise (red) rotation at 15 Hz. Chiral selection was not observed for this batch. The magnetic field and rotation are switched off at the times depicted in the figure.

Figure 4.12 shows the difference in aggregation kinetics for clockwise and anticlockwise rotation in a magnetic field in the analysis of the characteristic times. The analysis of the zero-field rotation experiments is also shown.

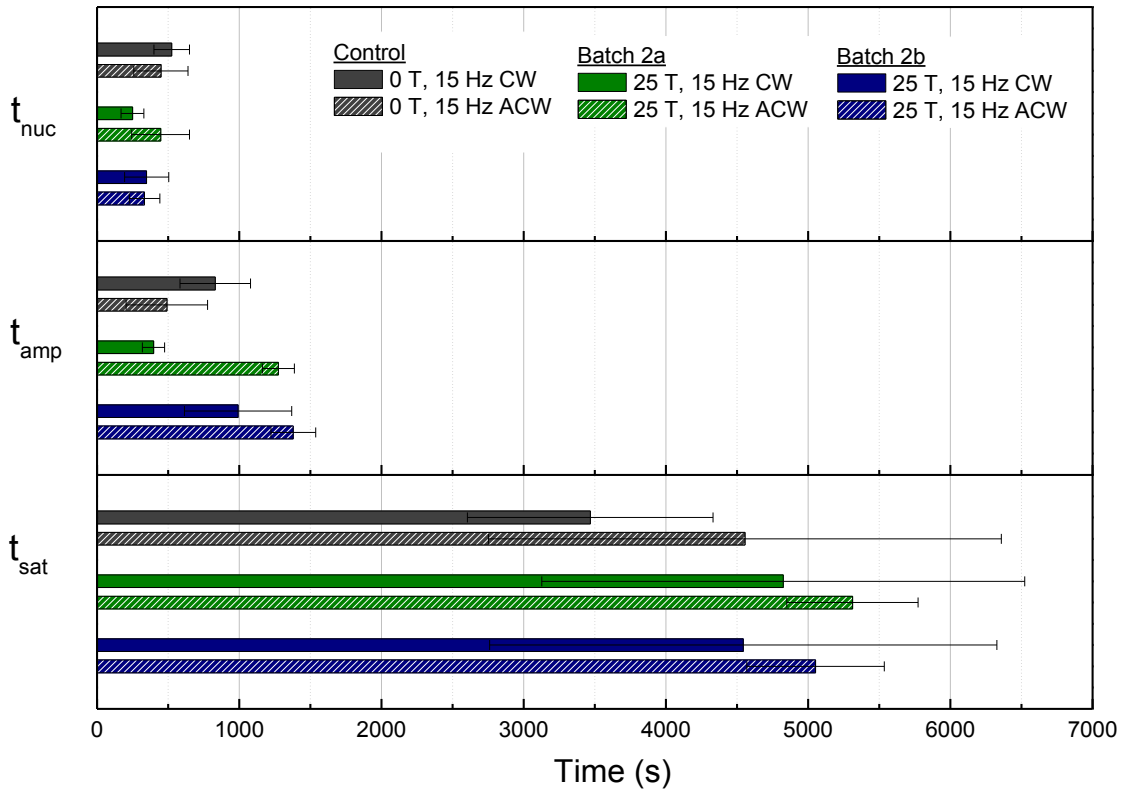

Figure 4.12 Analysis of the characteristic times for the kinetic spectra of aggregations with rotation in a magnetic field for batch 2a (green) and batch 2b (blue). Also the zero field rotation experiments are shown (grey).

The main difference in the aggregation kinetics (batch 2a) for the clockwise and anticlockwise rotation is in the nucleation time t_{nuc} and amplification time t_{amp}. This difference is almost totally gone for batch 2b and also for the zero field measurements which even tend to have a slightly opposite difference.

For the magnetic field experiments, also the dissymmetry factor Δg is plotted against the characteristic times t_{nuc}, t_{amp}, and t_{sat} (supplemental material S11, figure S21). Again no clear relations are observed.

The percentage of monomer left (at t=20.000s) is shown in figure S25 for the different aggregation conditions (*NB*). The on average smallest percentage of monomers left is for the magnetic field experiments with batch 2a. The aggregations of batch 2b in a magnetic field and the rotation experiments (B=0) have a comparable percentage that is higher. The stationary experiments yielded on average the highest percentage of monomer left. The variation in this percentage is however big compared to the differences.

Some of the kinetic spectra in figure 4.10 and 4.11 show a small change in monomer absorbance at the time the magnetic field is sweeping down, between 3600 s to 3840 s. Not only the monomer absorbance, but also the aggregate absorbance changes when sweeping the magnetic field down. In fact, the aggregate absorbance changes a lot more than the monomer absorbance during this time interval. For most experiments, the aggregate absorbance goes up when sweeping down from 25T to 0T. This does not count for all experiments however. The different observed changes in absorbance, while sweeping down, are given in supplemental material S15 together with the specific situation in each experiment.

5 Discussion

The starting point for this research is the publication from Micali et al. concerning supramolecular chiral selection by a falsely chiral influence. In this research the aggregation kinetics of this chiral selection process is investigated. The influence of rotational and magnetic forces on this kinetics is probed to learn more about the mechanisms of aggregation and chiral selection. This section discusses the results in a similar order as the results section.

5.1 Characterization of monomers and aggregates

The free base and diacid form of $TPPS_3$ both have a specific absorbance spectrum with absorbance maxima at respectively 413 and 434 nm (figure 4.1). Both H- and J-aggregates are visible in the UV/Vis and CD spectra. For the formation the aggregates, protonation of the free base of $TPPS_3$ is needed. An increased ionic strength, by adding NaCl, then facilitates the aggregation. The absorbance of the H-aggregates is around 420 nm and overlaps with the absorbance of the diacid $TPPS_3$. The J-aggregates absorb at a wavelength of 489 nm and are thereby completely distinguishable. The J-aggregates are formed by non-covalent interactions such as hydrogen bonding, π-π stacking and electrostatic interactions. This formation is an equilibrium process and the equilibrium state depends on the temperature (figure S22).

5.2 The aggregation kinetics

5.2.1 General characteristics of the aggregation kinetics

The aggregation process is a statistical process (figure 4.6, S16 and S17) and a highly sensitive one. The kinetics depend highly on the aggregation procedure which includes not only the final concentrations of the acid, salt and $TPPS_3$, but also the mixing volumes, the order of mixing and timing between the different steps (supplemental material S7). The aggregation kinetics can therefore be said to highly depend on the microscopic environment and the local concentrations of all reagents. This explains its high sensitivity and statistical nature. Contamination also plays a role in the aggregation process and is easily attained. A contamination, such as dust, can enhance the speed of the aggregation by facilitating the nucleation. A contamination might also be the reason for the observed chiral bias towards positive Δg, since it is previously seen that chiral templates can direct the chirality.[39]

The aggregation kinetics can be divided into three regimes (figure 4.4); a nucleation period, an amplification period and a saturation period. None of the models described in the scientific background can accurately model this kinetics. The cooperative model does give a good fit for the nucleation and amplification period (figure 4.5), which suggest the correct model includes a form of cooperative growth. In the saturation regime, the cooperative model fails to fit the kinetic data. Instead of analyzing each kinetic spectrum with the parameters of a model, it is therefore chosen to define characteristic times which describe the three different stages of the aggregation kinetics (*section 4.2.1*).

5.2.2 The influence of rotation

The influence of rotation on the aggregation process is investigated by performing *in situ* absorbance measurements of stationary and rotating solutions. In rotation conditions, the vial is rotating at a frequency of (15±0.5) Hz for the first hour of the aggregation. After three days the aggregates are analyzed *ex situ* by circular dichroism measurements.

Rotation significantly increases the speed of the aggregation in every stage: nucleation, amplification and saturation. For three different temperatures (18°C, 23°C and 28°C), all three characteristic times of the aggregation are on average smaller for rotation conditions than for

stationary conditions. The standard deviations are thereby almost always smaller than the differences in time averages and often there is even no overlap between the averages including standard deviation (figure 4.6, 4.7a, S16, S17, S18 and S19).

Besides the faster aggregation kinetics, rotation also has an influence on the absolute configuration of the aggregates. The CD signals are considerably different for aggregates formed under stationary and rotation conditions (figure 4.2). The CD signals of aggregates formed under stationary conditions are highly asymmetric with respect to the absorbance maximum of the aggregates. The zeros of the CD signals don't correspond to the maxima of the absorbance and the maximum and minimum of the CD signal are of different magnitude. On the other hand, aggregates formed under rotation conditions have CD spectra that are more like typical bisignate CD signals. Besides, there is a large variation in the CD signals for the stationary aggregations regarding both the position and shape. The CD signals of aggregates formed under rotation conditions are much more consistent. This suggests that the mechanism of aggregation is more controlled when the solution is rotating compared to stationary.

Another influence of rotation is that the relative amount of monomer left at the end of the aggregation is on average smaller for rotation conditions than for the stationary conditions (figure 4.7b). The relative amount of monomer left is related to the thermodynamics of the aggregates, because the equilibrium state is determined by ΔG (figure 2.3). It suggests that aggregates formed under rotation conditions are energetically more favorable (larger ΔG) because a relatively less amount of monomers is left at the equilibrium state.

All results discussed above lead to the conclusion that the aggregation of $TPPS_3$ results in different aggregates for rotation and stationary conditions. The difference in CD signals shows that the absolute configuration of the aggregates formed under stationary and rotation conditions is different. Besides, the aggregates formed under rotation conditions are energetically more favorable as seen in the relative amount of monomer left. The speed of the aggregation is thereby increased upon rotation which can be a result of the different thermodynamics. The potential energy profiles for aggregates of different energies are likely to be different, resulting in different kinetics.

Rotation thus clearly alters the aggregation process, resulting in different aggregates and aggregation kinetics. The microscopic environment in the solution must therefore be altered by rotation since the microscopic environment is essential in the formation of the aggregates. This is seen in the sensitivity and statistical nature of the aggregation process. The local hydrodynamics, influencing the microscopic environment, are the result of the rotation which cannot be described by a solid body rotation. In a solid body rotation, the microscopic environment does not differ from a stationary situation and this way there should be no influence of the rotation at all. An explanation is that secondary flows arise in the vial if it is rotated. The question is if this is inherent to the rotation of a fluid inside a vial or because of technical inaccuracies which give rise to a small precession of the vial when rotated. The parabolic curvature of the solution (meniscus), which is a result of the rotation of a partly filled vial, might be important for these secondary flows and local hydrodynamics. The importance of the meniscus is already hinted at by Micali et al. since they did not find enantioselection in completely filled vials.

Comparison of the aggregation kinetics in this research with the aggregation kinetics measured by Micali et al. is difficult because a different $TPPS_3$ batch and also a higher $TPPS_3$ concentration are used in this research. It is measured that rotation conditions result in different aggregates and different aggregation kinetics with respect to stationary conditions. It is however unknown how this compares to stirring. This research however suggests that rotation of the sample vial cannot be described by a solid body rotation, as was stated by Micali et al.

Chirality of the aggregates

Another topic is the chirality of the aggregates which can be seen in the circular dichroism signal and is described by the dissymmetry parameter *Δg.* For stationary aggregation conditions, clearly no chiral selection takes place. A large bias towards positive values of *Δg* is observed (figure 4.8 and 4.9) of which the origin is unknown.

Ribo et al.[9] previously found chiral selection of J-aggregates only based on the rotation direction with stirring. From the data of $TPPS_3$ in this research, batch 1 and rotation conditions, it cannot be determined if there is chiral selection based on only the rotation direction. For clockwise rotation, only positive Δg values are obtained. For anticlockwise rotation, the majority of the experiments resulted also in positive Δg values, but a few resulted in negative Δg (figure 4.8). Chiral selection on rotation direction is possible if the J-aggregates are of such a size that the normal gravity can have an influence. Ribo et al. had however much larger aggregates (~25μM) than observed for $TPPS_3$ by Micali et al.[1](<0.1μM). The aggregates of $TPPS_3$ in this research might be different since a higher concentration of $TPPS_3$ is used, but the size of the aggregates is not measured in this research.

5.2.3 The influence of the magnetic field

The influence of the magnetic field on the aggregation was investigated by measuring *in situ* absorbance of a rotating vial with and without a magnetic field applied for one hour. After three days *ex situ* a CD spectrum of the sample is measured to look at the chirality and absolute configuration of the aggregates. When applying a magnetic field of 25T combined with a (15±0.5) Hz rotation, the same chiral selection as found by Micali et al. was observed for batch 2a (figure 4.9a). The supramolecular chirality of the aggregates is determined by the relative direction of the effective gravity and angular momentum. With an effective gravity equal to the normal gravity, aggregates with a negative *Δg* are obtained for clockwise rotation and aggregates with a positive *Δg* for the anticlockwise rotation. Although a different $TPPS_3$ batch and a different $TPPS_3$ concentration were used, the same absolute enantioselection by the rotational and magnetic forces occurred, proving the robustness of the chiral selection mechanism. The combination of the external physical forces, a falsely chiral influence, is able to overrule the chiral bias observed for aggregations without applying a magnetic field (figure 4.9c,d).

The magnitude of the CD signals observed in this research, indicating the magnitude of the enantiomeric excess, is however much lower than the ones observed before by Micali et al.[1]. This might be an effect of the batch or the concentration. No relation could be found however between the characteristic times and the magnitude of the CD signals, indicating that concentration might not lead to different magnitudes of the circular dichroism (since concentration alters the speeds of the aggregation). Another possibility is that the aggregation kinetics does influence the magnitude of the CD signal, but since the characteristic times are approximately all in the same order of magnitude, it could not be observed in this research.

Besides the influence of the magnetic field on the chirality of the aggregates, also the influence on the aggregation kinetics is investigated. The magnetic field does on average not have an effect on the aggregation kinetics, neither slowing down nor accelerating (figure 4.10). The aggregation is a statistical process with a large variation and the characteristic times, describing the different stages, are on average equal with and without a magnetic field (figure 4.12). The magnetic field has however an influence on the aggregation kinetics by splitting the kinetics for the different rotation directions (figure 4.10). With a magnetic field of 25T, the aggregation kinetics for clockwise rotation is significantly faster than for anticlockwise rotation. This difference in aggregation kinetics is mainly expressed in the nucleation and amplification stage.

For such a difference to occur, the symmetry between clockwise and anticlockwise rotation has to be broken. The question is if the symmetry is broken by an artifact or something inherent to the aggregation system.

A possible artifact, causing symmetry breaking, is that the rotation is not exactly equal for anticlockwise and clockwise rotation. Because the rotator was originally built for clockwise rotation, the anticlockwise rotation might be less stable (this is not observed visually). Several observations indicate however that the symmetry is not broken by an artifact like this. First of all, without applying a magnetic field there is only a small difference in aggregation kinetics between the different rotation directions, which is even in the opposite direction as for the chiral selection process (figure S24). Secondly, in batch 2b no chiral selection was observed when applying the rotational and magnetic forces. For this batch also the difference in aggregation kinetics for the different rotation directions disappeared (figure 4.9b). To provide clear evidence that the symmetry breaking is not caused by an artifact, the observed difference should be reproduced and in addition checked by inverting gravity instead of inverting the rotation direction.

If the symmetry is broken by something inherent to the system, the question still remains if this difference in aggregation kinetics is directly coupled to the chiral selection. The Lorentz force is for example able to break symmetry in the distribution of the ions in the solution. The distribution of ions is inverted, when inverting the rotation direction. This distribution is important for the kinetics of the aggregation. The Lorentz force does however not play a role in the chiral selection, since inverting the magnetic field does not change the chiral selection while it does change the Lorentz force.[1] The Lorentz force is thus able to change the dynamics of the system without influencing the chiral selection. The fact that no difference in aggregation kinetics was observed when no chiral selection took place (batch 2b) suggests however that the aggregation kinetics and chiral selection are coupled.

The potential energy diagram in figure 2.3 shows that the kinetics towards each enantiomer is coupled with the chiral selection mechanism of a falsely chiral influence. This is necessary for a falsely chiral influence to induce enantioselection, because it cannot distinguish between the enantiomers energetically. This means that if the falsely chiral influence is present, one enantiomer is formed more easily which is opposite for the inversed falsely chiral influence. This does however not have to result in different aggregation kinetics between the two rotation directions (only between the enantiomers for each rotation direction). If there is a difference in the kinetics under different rotation directions, as is observed, this means that the kinetic pathways of forming the enantiomers are different for both the different rotation directions and for each enantiomer. Thus, as said before, symmetry is broken between the rotation directions and a cause for the symmetry breaking has to be found.

The chiral bias present in the system is a cause of symmetry breaking. Important to notice is that the aggregation kinetics for chiral selection opposite to the chiral bias is faster than for chiral selection equal to the bias. This means that the difference in kinetics is not simply the consequence of one selection being in the same direction as the bias and the other in the opposite direction. The bias might however be important for the observed difference in aggregation kinetics. The bias can act in two different ways. Either it facilitates the forming of one enantiomer or it inhibits the formation of the other enantiomer. The knowledge about the selection towards positive Δg has faster aggregation kinetics than for negative Δg and that the chiral bias is towards positive Δg does however not give a conclusive answer to the nature of the bias. The same also counts for the selection forces, which also either can act as facilitators or as inhibitors.

Another important observation in this aggregation process is that the aggregates are not distributed over the solution homogeneously (supplemental S8) and that this is altered by the magnetic field (supplemental S15). This suggests that the magnetic field influences the microscopic environment which is very important for the aggregation mechanism and chiral selection.

Chiral selection takes place only when applying a magnetic field, but the sign of the magnetic field is not important as seen by Micali et al.. Therefore it is the alignment force, originating from the magnetic field that plays an important role in the chiral selection process. Magnetic alignment only acts on structures big enough and this means that the chiral selection takes place at a time when the aggregates are big enough to be magnetically aligned.

5.3 Future plans

This research provides a lot of new insight in the mechanism behind the aggregation of this chiral selection process, but it provides also a lot of new questions. It clearly involves a mechanism in which the microscopic environment with the local hydrodynamics is important for the aggregation and chiral selection mechanism. Several kinds of experiments in the future can help to better understand the mechanism of this chiral aggregation process.

Most importantly is to measure the effect of inverting the effective gravity on the aggregation kinetics for clockwise and anticlockwise rotation. If this results in a significant difference in the aggregation kinetics depending on the sign of the effective gravity, it is really proven that the aggregation kinetics and chiral selection are one to one coupled. This means that there is a factor inherent to the system, causing symmetry breaking.

Then it is important when the chiral selection actually takes place. This is already under investigation by applying rotational and magnetic forces for different times and at different starting points. The experimental setup for measuring the aggregation kinetics might be of use, since the process can be followed and at any desirable moment, physical forces can be turned on and off. A major drawback of this experimental setup is that only one sample can be measured at a time in contrast to seven samples before.

Another aspect of the aggregation is where it actually takes place. Does the aggregate formation take place everywhere in the solution or only at a certain interface (glass/liquid, air/liquid or even glass/liquid/air). This can be investigated using fluorescence microscopy. Although in this research the aggregates did not show any fluorescence, they should possess it. By using lasers instead of a lamp and the possibility to detect fluorescence on smaller time scales, it might be possible to observe this fluorescence. If sufficiently strong fluorescence is observed, it can be used to detect and locate the aggregates inside the sample vials.

Since the aggregates stick to the wall of the vial, it is useful to measure the aggregation kinetics in vials that are coated in a way to prevent this interaction. In this way the influence of the glass can be investigated. Fluorinated agents as coating agents are useful in such an approach because most molecules are fluorophobic.

The last two future plans involve *in situ* measurements of certain characteristics of the aggregates, which provide information about the mechanism. The first idea is to perform circular dichroism experiments *in situ*. This way the development of the chirality can be followed which will provide much insight into the mechanism. In principle the same insert can be used as for the aggregation kinetics measurements. Adjustments have to be made however, due to magneto- circular dichroism effects of the mirrors and lenses. A second idea is to do *in situ* dynamic light scattering (DLS) measurements. The size of the aggregates will also give a lot of information about the growth process and if this could be followed in time for different aggregation conditions, this would provide a lot of new information.

6 Conclusion

Previously, Micali et al.[1] were able to achieve enantioselection of the J-aggregates of $TPPS_3$ by applying rotational and effective gravitational forces. In this research the aggregation of the diacid into the J-aggregates is investigated for different aggregation conditions and the influence of the external forces on the kinetics and chiral selection is examined.

The aggregation consists of roughly three different stages; a nucleation stage, an amplification stage and a saturation stage. A large variation is found in the aggregation kinetics between aggregations under equal circumstances. The aggregation process highly depends on the microscopic environment and fluctuations in this environment are the reason for the statistical nature of the process.

Rotational forces are of great influence on this microscopic environment. The local hydrodynamics determine the nucleation-growth of the aggregates and this cannot be described by a solid body rotation. A 15Hz rotation of the sample during the first hour of aggregation namely leads to the formation of different aggregates than obtained under stationary conditions. The absolute configuration, measured by CD, is considerably different for the aggregates formed under rotation conditions than for the aggregates formed under stationary conditions. Moreover, the equilibrium state consists of a relatively lower amount of monomers suggesting that the aggregates are energetically more favorable when formed under rotation conditions. The rotation thereby also accelerates the aggregation process in all three stages. That the rotation cannot be considered a solid body rotation can be explained by the emergence of secondary flows if the vial is being rotated. The meniscus of the solution might be an important factor in this mechanism.

Magnetic forces also have a big influence on the aggregation because together with rotational forces a falsely chiral influence is formed which can lead to enantioselection. The same enantioselection as Micali et al. is found in this research by applying a magnetic field of 25T and a rotation of 15 Hz. Although a different batch and different concentration of $TPPS_3$ are used, the same enantioselection occurs which proves the robustness of the chiral selection mechanism. The supramolecular chirality is directed by relative direction of the effective gravity and angular momentum. With the effective gravity being equal to the normal gravity, a clockwise rotation results in a negative Δg and anticlockwise rotation results in positive Δg. The falsely chiral influence is able to overrule to chiral bias, which is towards positive Δg. The J-aggregates formed under these conditions have bisignate CD signals.

The magnetic field does on average not have an effect on the aggregation kinetics. The magnetic field does however create a difference in the aggregation kinetics depending on the rotation direction. The formation of enantiomers with positive Δg has significantly slower aggregation kinetics than the formation of enantiomers with negative Δg. For this to happen, symmetry between the rotation directions must be broken. The chiral bias is a factor that breaks the symmetry, but the bias is found to be towards positive Δg while the aggregation kinetics for selecting the positive Δg enantiomer is slower. The bias thus cannot simply explain the observed difference in aggregation kinetics. It is unlikely that an artifact is responsible for the symmetry breaking because in a $TPPS_3$ dilution that does not show chiral selection under the same conditions, also the difference in aggregation kinetics is gone. To provide clear evidence that this differentiation in aggregation kinetics is inherent to the chiral selection mechanism, the same result should be obtained by inverting the effective gravity instead of the rotation direction.

The aggregation of $TPPS_3$ in chiral aggregates thus is a very complicated process which is determined by the microscopic environment and local hydrodynamics, which are influenced by both the rotational and the magnetic forces. The observed difference in aggregation kinetics depending on the rotation direction when applying a magnetic field indicates the importance of the kinetics in chiral selection by a falsely chiral influence. More research has to be done to understand more about the aggregation mechanism involving chiral selection.

Acknowledgements

First I would like to thank drs. Peter van Rhee (Phd HFML) for his daily supervision during my entire internship. Then I would like to thank prof. dr. Peter Christianen for his help and the fruitful discussions we had. Last but certainly not least I would like to thank the technical staff of the HFML and in particular Lijnis Nelemans and ing. Peter Albers for their help in establishing my experimental setups.

References

1. Micali N *et al*., Selection of supramolecular chirality by application of rotational and magnetic forces. *Nat Chem* **4**(3): 201-207. (2012).
2. Barron L.D., *An introduction to chirality at the nanoscale*. Wiley-VCH, Weinheim (2009)
3. Brown, J. M. et al., Chemical asymmetric synthesis. *Nature* **342** (6250): 631-636. (1989).
4. Flores, J.J. et al., G. A. Asymmetric photolysis of (*RS*)-leucine with circularly polarized UV light. *J. Am. Chem. Soc.* **99**, 3622–3625 (1977).
5. Noorduin, W. L. *et al*., Complete chiral symmetry breaking of an amino acid derivative directed by circularly polarized light. *Nature Chem*. **1**, 729–732 (2009).
6. Berger, R. et al. M., Electroweak quantum chemistry of alanine: parity violation in gas and condensed phases. *ChemPhysChem* **1**, 57–60 (2001).
7. Kondepudi, D. K. et al., Weak neutral currents and the origin of biomolecular chirality. *Nature* **314**, 438–441 (1985).
8. Aquilanti, V. et al., G. S. Observed molecular alignment in gaseous streams and possible chiral effects in vortices and in surface scattering. *Orig. Life Evol. Biosph*. **36**, 435–441 (2006).
9. Ribo, J. M. et al., Chiral sign induction by vortices during the formation of mesophases in stirred solutions. *Science* **292**, 2063–2066 (2001).
10. Escudero, C. et al., Folding and hydrodynamic forces in J-aggregates of 5-phenyl-10,15,20-tris(4-sulfophenyl)porphyrin. *Angew. Chem. Int. Ed*. **45**, 8032–8035 (2006).
11. Alexander Kuhn, A. et al., Absolute asymmetric reduction based on the relative orientation of achiral reactants. *Angew. Chem. Int. Ed*. **48**, 6857–6860 (2009).
12. Rikken, G. L. J. A. et al., Enantioselective magnetochiral photochemistry. *Nature* **405**, 932–935 (2000).
13. Avalos, M. *et al*. Absolute asymmetric synthesis under physical fields: facts and fictions. *Chem. Rev.* **98**, 2391–2404 (1998).
14. Lord K. Baltimore, lectures on molecular dynamics and the wave theory of light. London: DJ Clay &Sons; 1904. Reprinted by Cambridge University Press, p703. (2010)
15. Beenakker, W.J.P., Kwantummechanica 2, Radboud University Nijmegen, jaargang 2012-2013
16. Greaves, H., Towards a geometrical understanding of the CPT theorem. [Preprint] URL: http://philsci-archive.pitt.edu/id/eprint/3676 (accessed 2013-06-05). (2007)
17. Barron, L. D. True and false chirality and absolute asymmetric-synthesis. *J. Am. Chem. Soc*. **108**, 5539–5542 (1986).
18. Rikken, G. L. J. A. et al., Observation of magneto-chiral dichroism. *Nature* **390**(6659): 493-494. (1997)
19. Barron, L. D., Reactions of chiral molecules in the presence of a time-non-invariant enantiomorphous influence: a new kinetic principle based on the breakdown of microscopic reversibility. *Chem. Phys. Lett*. 135, 1–8 (1987).

20. Barron, L. D. True and false chirality and absolute asymmetric-synthesis. *J. Am. Chem. Soc*. 108, 5539–5542 (1986).
21. Loudon, R., The quantum theory of light, 3rd edition, Oxford, Oxford Science Publications (2010)
22. Berova, N., et al., *Circular Dichroism: Principles and applications,* 2nd edition, Wiley-VCH, New York (2000)
23. **a** *G. Scheibe, Angew. Chem. 1937, 50, 51;* **b** *G. Scheibe et al., Naturwissenschaften 1937, 25, 75;* **c** *G. Scheibe, Angew. Chem. 1937, 50, 212–219; the first report of Scheibe on the absorbance spectra of a solution of PIC iodide in water describes the formation of H-aggregates:* **d** *G. Scheibe, Angew. Chem. 1936, 49, 563.*
24. **a** *E. E. Jelley, Nature 1936, 138, 1009–1010;* **b** *E. E. Jelley, Nature 1937, 139, 631–632.*
25. Boiadjiev, S.E., et al., Exciton Chirality. (A) Origins of and (B) Applications from Strongly Fluorescent Dipyrrinone Chromophores, *Monatshefte f€ur Chemie* **136**, 489–508 (2005)
26. Würthner, F. et al., J-Aggregates: From Serendipitous Discovery to Supramolecular Engineering of Functional Dye Materials. *Angew. Chem. Int. Ed.*, **50**: 3376–3410. (2011)
27. El-Hachemi, Z. et al., Structure vs. properties - chirality, optics and shapes - in amphiphilic porphyrin J-aggregates. *Journal of Materials Chemistry C* **1**(20): 3337-3346. (2013)
28. Griffiths D.J., *Introduction to electrodynamics*, 3rd edition, San Fransisco, Pearson Education , p202 (2008)
29. Gielen, J.C., Phd thesis: *Supramolecular aggregates in high magnetic fields*, Radboud University Nijmegen, p10-13, (2010)
30. Maret, G. et al., Biomolecules and polymers in high steady magnetic fields, *Topics in Applied PhysicsVol*. **57**, p143-204 (1985).
31. Kitahama, Y. et al., Study of internal structure of meso-tetrakis (4-sulfonatophenyl) porphine J-aggregates in solution by fluorescence microscope imaging in a magnetic field, *Langmuir* **22**, 7600-7604 (2006).
32. Berry, M. V. et al., Of flying frogs and levitrons. *Eur. J. Phys*.**18**, 307 (1997).
33. Heijna, M. C. R. et al., Magnetically controlled gravity for protein crystal growth. *Appl. Phys. Lett*. **90**, 264105 (2007).
34. De Greef, T. F. A. et al., Supramolecular Polymerization. *Chemical Reviews* **109**(11): 5687-5754. (2009)
35. Smulders, M. J., et al., How to Distinguish Isodesmic from Cooperative Supramolecular Polymerisation. *Chem. Eur. J.*, **16**: 362–367. (2010)
36. Pasternack, R. F. et al., Aggregation Kinetics of Extended Porphyrin and Cyanine Dye Assemblies. *Biophysical Journal* **79**(1): 550-560 (2000)
37. Pasternack, R. F. et al., A Nonconventional Approach to Supramolecular Formation Dynamics. The Kinetics of Assembly of DNA-Bound Porphyrins. *Journal of the American Chemical Society* **120**(24): 5873-5878. (1998)
38. Lagarias, J.C., et al., Convergence Properties of the Nelder-Mead Simplex Method in Low Dimensions, *SIAM Journal of Optimization*, Vol. **9** Number 1, pp. 112-147, (1998)
39. Castriciano, M. A., A., et al., Kinetic effects of tartaric acid on the growth of chiral J-aggregates of tetrakis(4-sulfonatophenyl)porphyrin. *Chemical Communications* **48**(40): 4872-4874. (2012)

Supplemental Material

In the supplemental material extra data and figures are given to complement the information given in the report itself.

Contents

S1 Derivation of the relationship between ellipticity and absorbance difference.

Figure S1 shows how linearly polarized light is turned into elliptically polarized light because of the difference in absorbance for left- and right circularly polarized light in a chiral medium. This difference in absorbance results in an ellipticity with angle φ which is in the order of millidegrees.

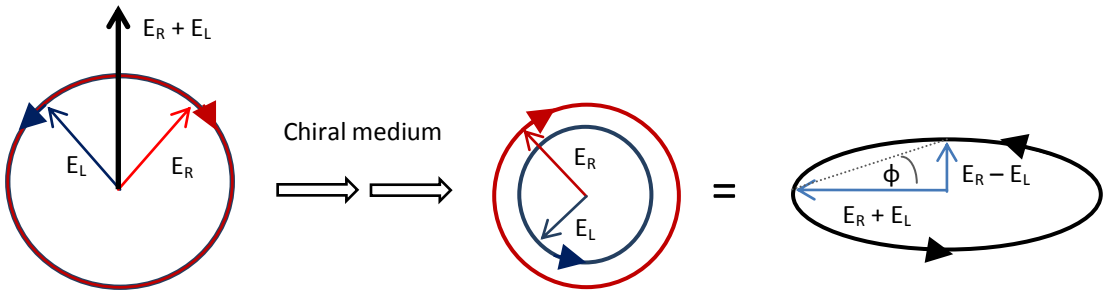

Figure S1. Linear polarized light (black) consists of left circularly polarized light (blue) and right circularly polarized light (red) which are absorbed differently in a chiral medium, resulting in elliptically polarized light.

The angle φ depends on the strength of the electric fields of left and right circularly polarized light;

$$\varphi = arctan\left(\frac{E_R - E_L}{E_R + E_L}\right)$$

Because the angle φ is very small, arctan(φ) ≈ φ. The amplitudes of the electric field are equal to the root of the intensity of the light. This gives

$$\varphi = \frac{E_R - E_L}{E_R + E_L} = \frac{\sqrt{I_R} - \sqrt{I_L}}{\sqrt{I_R} + \sqrt{I_L}}$$

The intensity of the light is related to the absorbance according to equation (1) giving

$$\varphi = \frac{\sqrt{I_0 e^{-\ln 10 \cdot A_R}} - \sqrt{I_0 e^{-\ln 10 \cdot A_L}}}{\sqrt{I_0 e^{-\ln 10 \cdot A_R}} + \sqrt{I_0 e^{-\ln 10 \cdot A_L}}}$$

$$\varphi = \frac{e^{\frac{-\ln 10}{2} A_R} - e^{\frac{-\ln 10}{2} A_L}}{e^{\frac{-\ln 10}{2} A_R} + e^{\frac{-\ln 10}{2} A_L}} = \frac{e^{\frac{\ln 10}{2} \Delta A} - 1}{e^{\frac{\ln 10}{2} \Delta A} + 1} \quad \text{with} \quad \Delta A = A_L - A_R$$

ΔA is small and the exponentials can therefore be approximated by the Taylor series ($e^x = 1 + x + x^2 + \ldots$) in first order leading to

$$\varphi = \frac{\frac{\ln 10}{2} \Delta A}{\frac{\ln 10}{2} \Delta A + 2} = \frac{\ln 10}{4} \cdot \Delta A$$

Converting φ from radials to millidegrees results in equation (3):

$$\varphi = \Delta A \cdot \frac{\ln 10}{4} \cdot \frac{180}{\pi} \cdot 1000 \approx 32982\, \Delta A$$

S2 Intensity spectra using filters C3C22 and C3C20

In experimental setup 2 and setup 3, the Ocean Optics USB2000+ spectrometer is used. This spectrometer uses a grating to separate the different wavelengths spatially and a CCD-chip measures the light intensity for these different wavelengths at different positions. Higher order peaks of double or triple frequencies can this way coincide with the first order peaks of the intended frequency. To circumvent this, a combination of filters was used in these experimental setups. Thereby a combination of two filters was necessary to optimize the sensitivity for wavelengths close to 400nm. The intensity spectrum of the halogen light source with these filters, separately and together, is shown in figure S2.

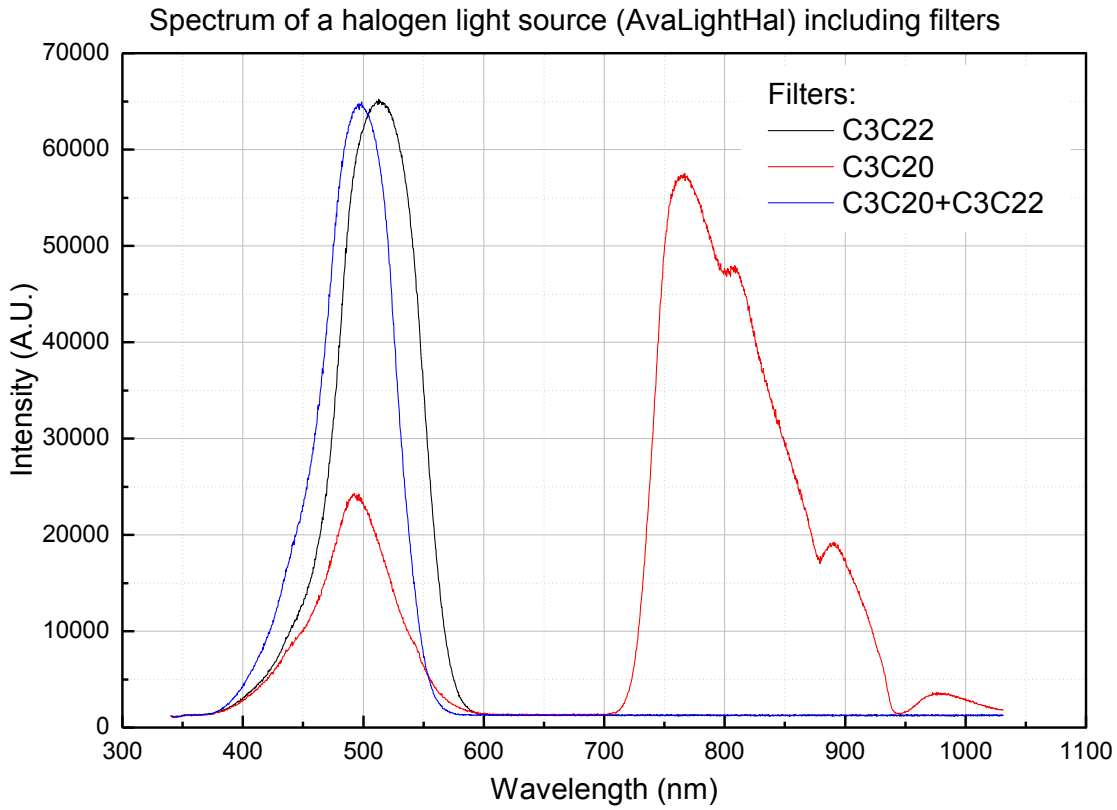

Figure S2. Intensity spectrum of the halogen light source including filters C3C20 and C3C22 used in experimental setup 2 and 3.

S3 Specifications of the magnet (Cell 1 at the HFML Nijmegen)

The specifications of the magnet in Cell 1 at the HFML, Nijmegen are provided below. This magnet is used in all magnetic field experiments performed in this research. It is a 50 mm bore 30 T Bitter magnet and the field strength is set by the electrical current. Table S1 shows the characteristics of the magnetic field at the field center, at different current strengths. Figure S3 shows the magnetic profile, meaning the strength of the magnetic field at position *z* inside the magnet, with a current of 9kA.

Table S1. Specifications of magnet Cell 1 (HFML Nijmegen), current versus magnetic field at the field center

B (T)	I (kA)	B(T)	I(kA)	B (T)	I (kA)	B (T)	I (kA)
0.5	0.6067	**8.0**	9.7071	**15.5**	18.8039	**23.0**	27.8938
1.0	1.2135	**8.5**	10.3137	**16.0**	19.4102	**23.5**	28.4994
1.5	1.8202	**9.0**	10.9203	**16.5**	20.0164	**24.0**	29.1051
2.0	2.4269	**9.5**	11.5269	**17.0**	20.6226	**24.5**	29.7106
2.5	3.0337	**10.0**	12.1334	**17.5**	21.2287	**25.0**	30.3161
3.0	3.6404	**10.5**	12.7400	**18.0**	21.8348	**25.5**	30.9216
3.5	4.2471	**11.0**	13.3465	**18.5**	22.4409	**26.0**	31.5270
4.0	4.8538	**11.5**	13.9530	**19.0**	23.0469	**26.5**	32.1324
4.5	5.4605	**12.0**	14.5594	**19.5**	23.6529	**27.0**	32.7377
5.0	6.0672	**12.5**	15.1659	**20.0**	24.2589	**27.5**	33.3430
5.5	6.6739	**13.0**	15.7723	**20.5**	24.8648	**28.0**	33.9482
6.0	7.2806	**13.5**	16.3787	**21.0**	25.4707	**28.5**	34.5533
6.5	7.8872	**14.0**	16.9850	**21.5**	26.0765	**29.0**	35.1584
7.0	8.4939	**14.5**	17.5914	**22.0**	26.6823	**29.5**	35.7635
7.5	9.1005	**15.0**	18.1977	**22.5**	27.2881	**30.0**	36.3684

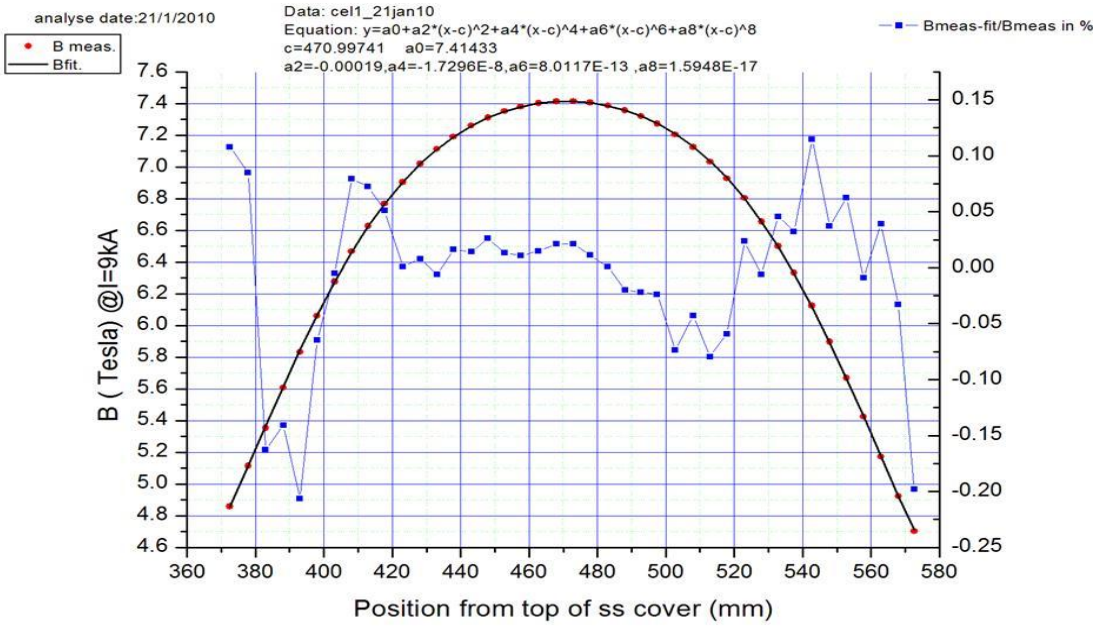

Figure S3. Magnetic field profile of magnet in Cell 1 (HFML, Nijmegen), at a current of 9kA

S4 Pictures of experimental setup 3

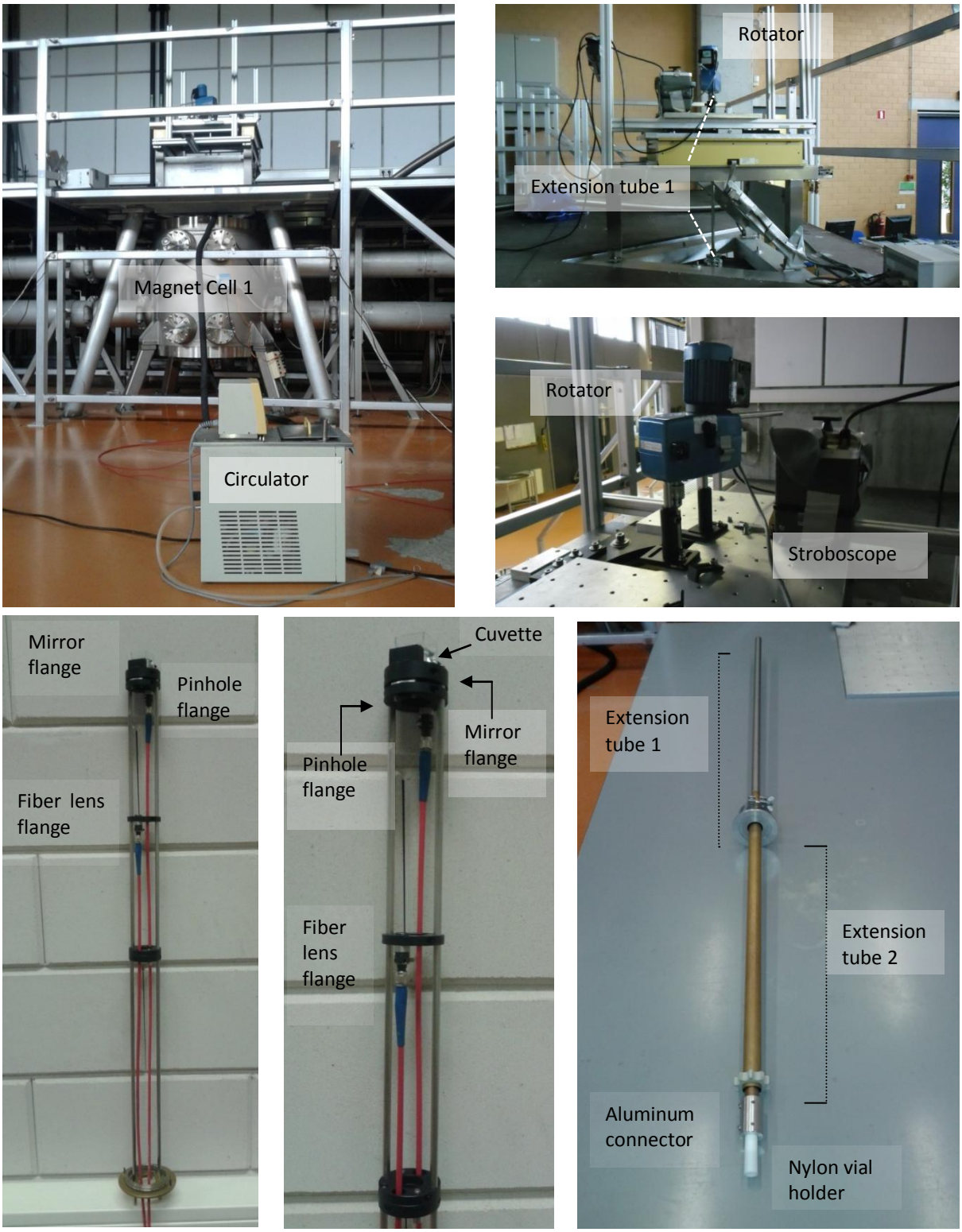

Figure S4. Extra pictures of experimental setup 3. Total setup (up) and upper and lower insert (down)

S5 Absorbance spectra of $TPPS_3$ up to 800 nm

Figure S5 shows the absorbance spectra from the free base $TPPS_3$ (a), the diacid $TPPS_3$ (b) and from the diacid, J-aggregates and H-aggregates (c) up to 800nm. The curves in the upper right corner are magnifications of 500-750nm, because many peaks are present but all of low intensity. Arrows assign which peaks belong to which structure.

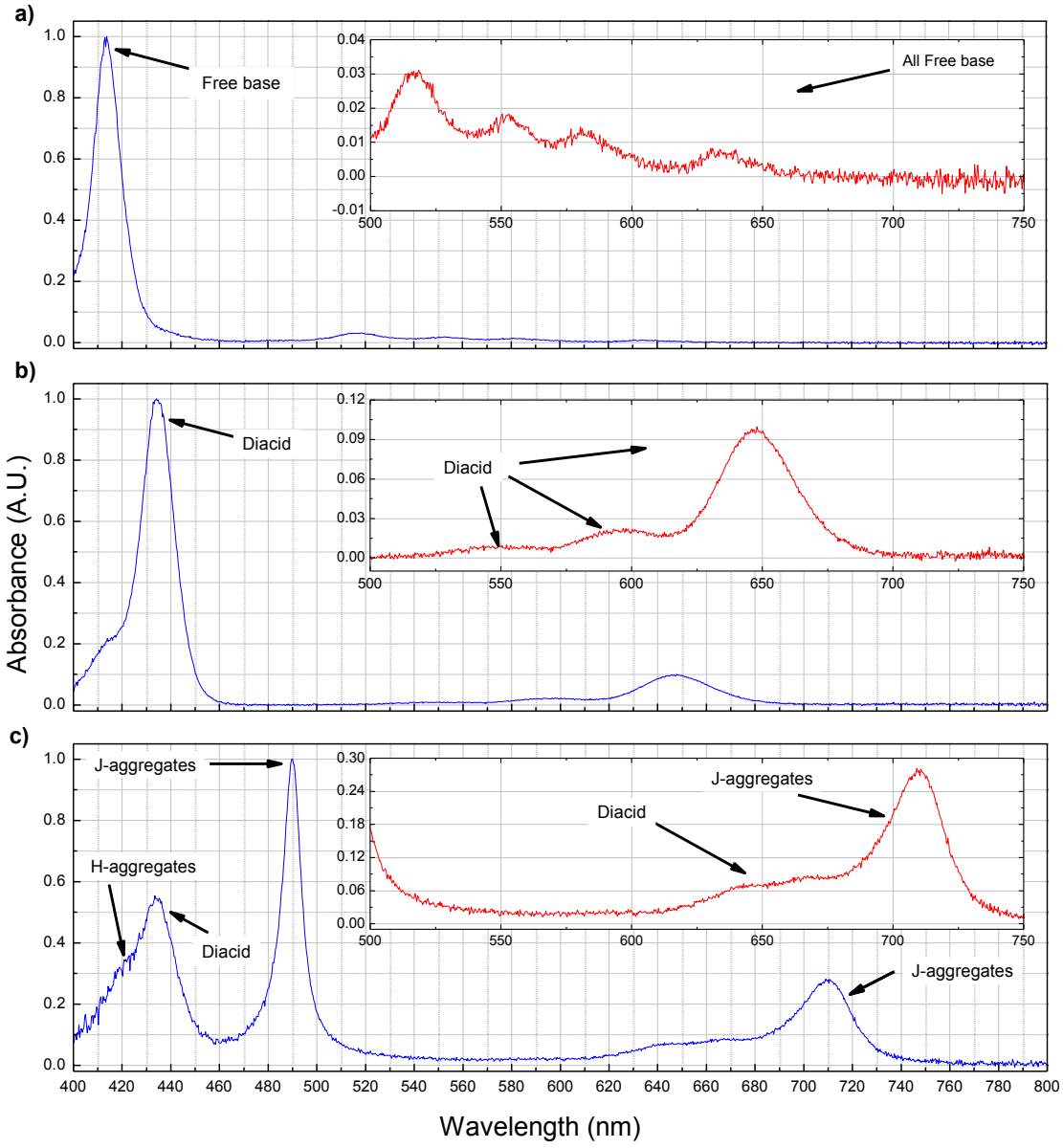

Figure S5. Absorbance spectrum for $TPPS_3$, the free base form (a), the diacid form (b) and the diacid form plus aggregates (c).

S6 Fluorescence of $TPPS_3$

Figure S6 shows the fluorescence spectra of a solution with only the diacid form of $TPPS_3$ (red) and a solution with both the diacid and J-aggregates present (blue). The diacid is fluorescent at 665nm with an excitation wavelength of 435nm. For the solution in which the J-aggregates are present, no extra fluorescence was observed. The fluorescence of the diacid in this solution is of lower intensity.

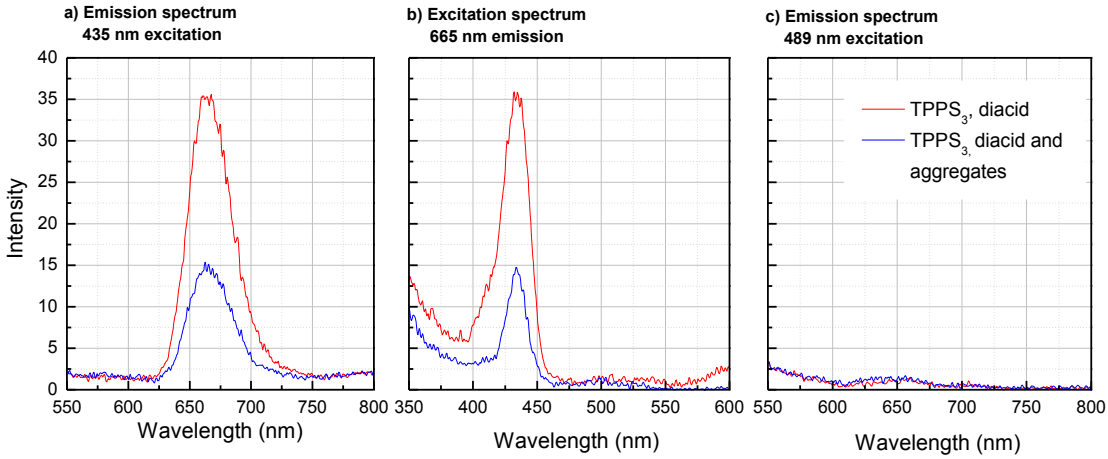

Figure S6. Fluorescence spectra of $TPPS_3$ diacid solution (red) and aggregate solution (blue). An emission spectrum with excitation at the monomers (435 nm) is shown in (a), an excitation spectrum at 665nm emission is shown in (b) and an emission spectrum with excitation at the aggregates (489nm) is shown in c).

S7 Sensitivity aggregation procedure

The aggregation of $TPPS_3$ diacid monomers into J-aggregates is a statistical process as can be seen in figure 4.6, S16 and S17. The aggregation process is very sensitive, which is probably necessary for small forces like the effective gravitation to be able to cause enantioselection. This sensitivity makes it hard to work with. Many parameters have an influence on the aggregation kinetics, but it is difficult to put this quantitatively since statistical variation is always present. Table S2 shows a list of the different parameters that will be discussed. The main idea is that the aggregation kinetics is highly influenced by the microscopic environment in the solution, so anything affecting this, will affect the kinetics as well.

Table S2. Parameters in the aggregation procedure that influence the aggregation kinetics

Number	Parameter
1	Final concentration of $TPPS_3$
2	Final concentration of NaCl (salt)
3	Final concentration of sulfuric acid (H_2SO_4)
4	Mixing volumes of 1,2, and 3
5	Order and timing of mixing 1,2 and 3
6	Aging of $TPPS_3$ solution

The general protocol, as described in the results section is:

- Add 16.7 µL 0.3mM porphyrin solution to 870 µL of MilliQ and mix it well
- Add 13.3 µL 1.0 M sulfuric acid solution and mix it gently using the micropipette
- Add 100 µL 1.0 M salt solution and mix it gently using the micropipette

In this protocol, the parameters from table S2 are varied to characterize their influences. Four different solutions are used in the aggregation procedure (table 3.1) with each their own function.

The $TPPS_3$ concentration is the amount of monomer that can react to form the aggregates. The sulfuric acid concentration determines the pH of the solution and thereby the ratio between the free base and diacid form of $TPPS_3$. A sodium chloride solution is added as a trigger for the aggregation. The sodium and chloride ions will increase the ionic strength of the solution, thereby reducing the repulsion forces between the anionic $TPPS_3$ monomers and facilitating the aggregation. Each of the concentrations of these reagents has to a certain extent an influence on the aggregation kinetics.

1 $TPPS_3$ concentration

Figure S7 shows the influence of the concentration of $TPPS_3$ on the aggregation kinetics in a stationary Hellma quartz cuvette. Higher $TPPS_3$ concentrations lead to faster kinetics; both the nucleation time and the amplification time (as defined in the results section) are shorter. Probably also the saturation time, but this cannot be seen in this figure. This is a general trend, and for every concentration there is some statistical variation causing the normalized traces to overlap. In general the speed of the aggregation goes up with higher concentrations. This is expected since the local concentrations of the monomer will be higher. This increases the chance of nuclei formation and also increases the amplification rate.

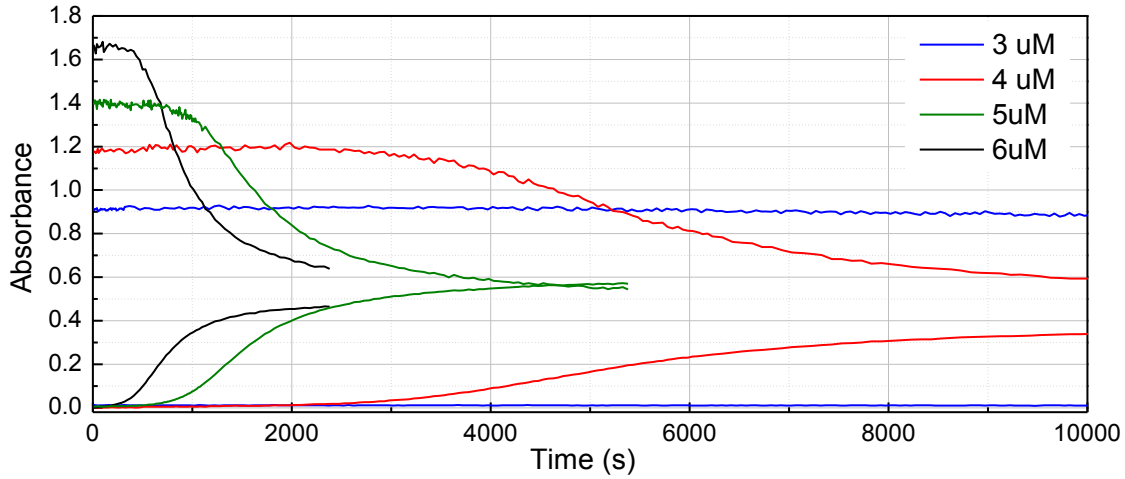

Figure S7. Aggregation kinetics in a stationary quartz cuvette with different concentrations of $TPPS_3$: 3µM (blue), 4µM (red), 5µM (green) and 6µM (black).

2 Sodium chloride concentration

The influence of the sodium chloride concentration is tested by performing aggregations of 6uM $TPPS_3$ with three different NaCl concentrations; 0.050M, 0.075M and 0.100M. The aggregations were done in a stationary Hellma quartz cuvette. For every salt concentration three traces are measured, shown in figure S8. For higher salt concentrations, all three characteristic times are smaller. This figure clearly shows the facilitating role of the salt. The sodium chloride increases the ionic strength of the solution, and as predicted, this facilitates the clustering of the monomers. It facilitates both the formation of the nuclei as the growth of the aggregates.

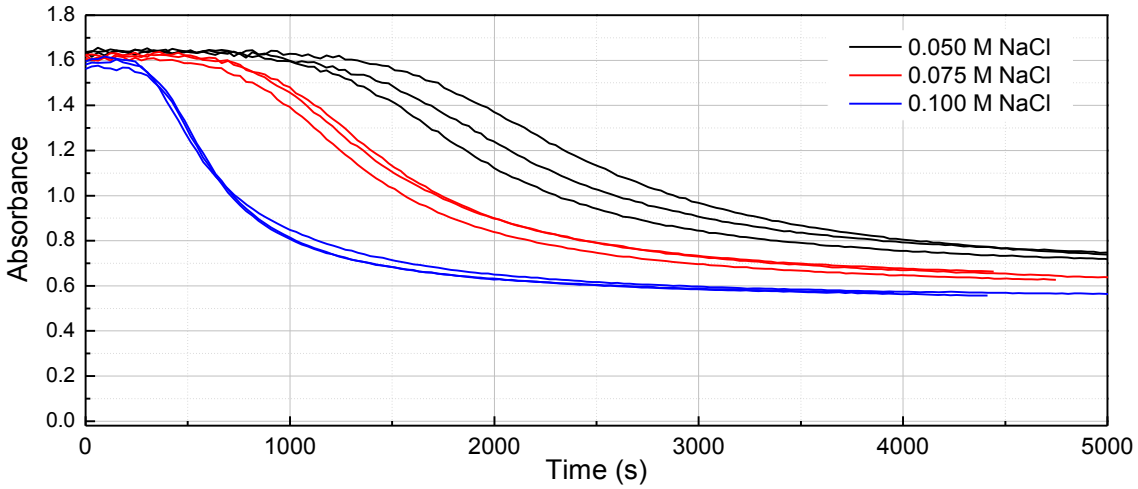

Figure S8. The aggregation kinetics of 6uM $TPPS_3$ with different concentrations of NaCl: 0.50M (black), 0.075M (red) and 0.100 M (blue).

3 Sulfuric acid concentration

The concentration of sulfuric acid does not have such a big influence as the salt- and $TPPS_3$ concentration. The sulfuric acid is needed to protonate the $TPPS_3$ for which a pH of less than about 4.8 is needed. The pK_a of $TPPS_4$ is 4.8[29] so for the $TPPS_3$ this will be similar. The pH of a 0.0133 M sulfuric acid solution is about 1.9, so any small variations in this pH will not really affect the ratio of *free base : diacid* since almost all $TPPS_3$ is protonated.

4 Mixing volumes

Besides the final concentrations, also the mixing volumes are influencing the aggregation kinetics. The mixing volumes are inversely proportional to the concentrations of a certain compound in these volumes if equal final concentrations are realized. Adding small volumes will result in high local concentrations of that specific compound while adding this volume. In the standard aggregation protocol, the influence of the mixing volumes of both the $TPPS_3$ and H_2SO_4 solution is negligible. The aggregation is not started when only the free base is present and a high local concentration of H_3O^+ does not trigger the reaction. For these solutions a volume should be chosen that can be accurately dosed, which means volumes close to the maximum volumes of the pipets (20µL, 200µL or 1000µL). The added volume of the NaCl concentration is important since high local concentrations of sodium chloride facilitate the nuclei formation. Smaller mixing volumes of NaCl thus lead to faster kinetics.

5 Mixing order and timing

The order of mixing in the standard aggregation protocol is according to the function of the different solutions. Salt acts as the trigger and therefore is the last additive. The order of mixing does matter for the aggregation kinetics. If the porphyrin solution is added last, then aggregation kinetics such as figure S9 are obtained. By adding the porphyrin solution last, immediate protonation occurs and there will be a high local concentration of the diacid which results in fast kinetics. As in figure S9, at the start of the absorbance measurements, already aggregates are formed. The $TPPS_3$ molecules should therefore be mixed well in the solution, before adding the salt.

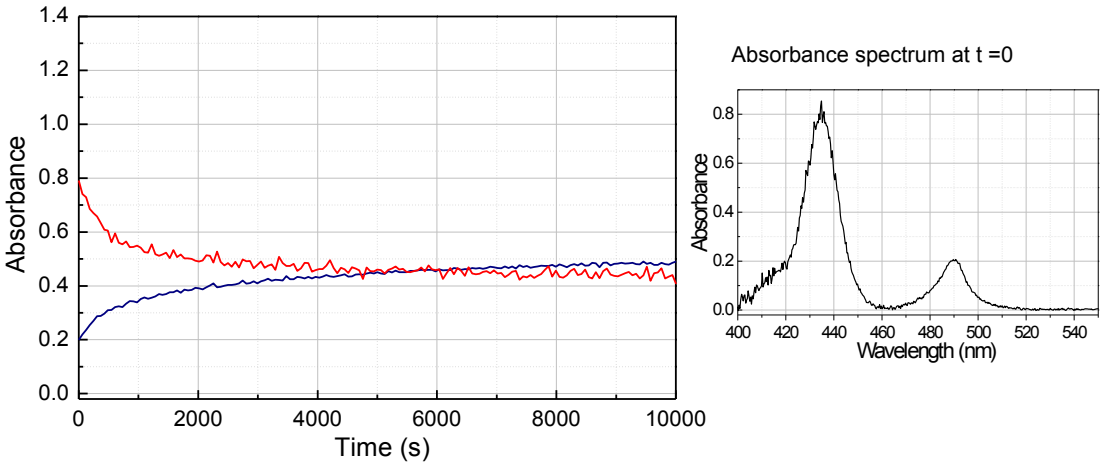

Figure S9. Typical curve for the aggregation kinetics when the porphyrin solution is added last, or the porphyrin solution is not well mixed. The kinetic traces (left) and the absorbance spectrum at time zero (right) are shown.

Although the influence is quite less, the H_2SO_4 solution should be added after the $TPPS_3$ solution because of the same reason. Without the addition of sodium chloride, the porphyrin molecules can still aggregate, but at a much slower rate. This is depending on the concentration of the diacid. Adding the $TPPS_3$ solution in solution with pH=1.9 results in high local concentrations of the diacid of $TPPS_3$ and facilitates the aggregation. The aggregation kinetics of 5µM $TPPS_3$ without adding the salt is shown in figure S10 with a close up of the first 20.000 seconds, the time at which the aggregation following the standard aggregation procedure is equilibrated. The diacid form of $TPPS_3$ In figure S10 also the curve of the free base of $TPPS_3$ is shown, showing that the free base is stable over time.

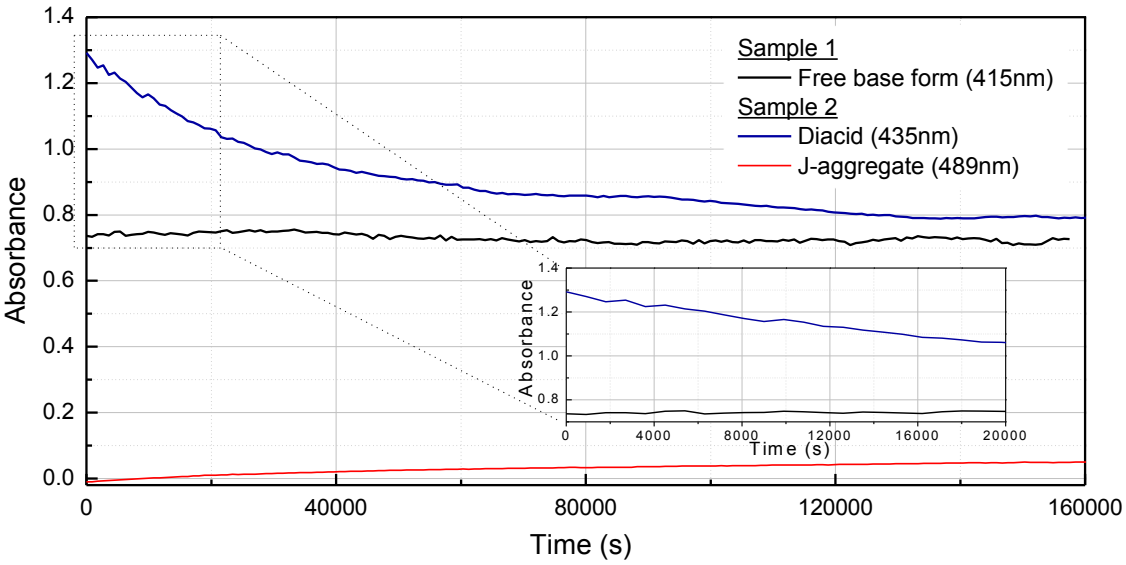

Figure S10. The stability of the free base form of $TPPS_3$ (black) and the diacid (blue) which forms aggregates (red) even without adding salt.

Figure S11 again shows the stability of both the free base (a) and the diacid form (b) of $TPPS_3$. A 1 ml solution of 4 µM $TPPS_3$ is poured into a Hellma quartz cuvette and the absorbance spectrum is measured with experimental setup 1. After measuring an absorbance spectrum, the solution is shaken by hand for 30 seconds and thereafter again an absorbance spectrum is measured. This is done for a solution with and without adding the sulfuric acid.

The free base of $TPPS_3$ shows to be very stable, its absorbance spectrum does not change. The diacid is forming aggregates however, when the solution is subjected to shaking. Both figure S10 and S11 thus show that the free base is stable over time while the diacid is rather unstable.

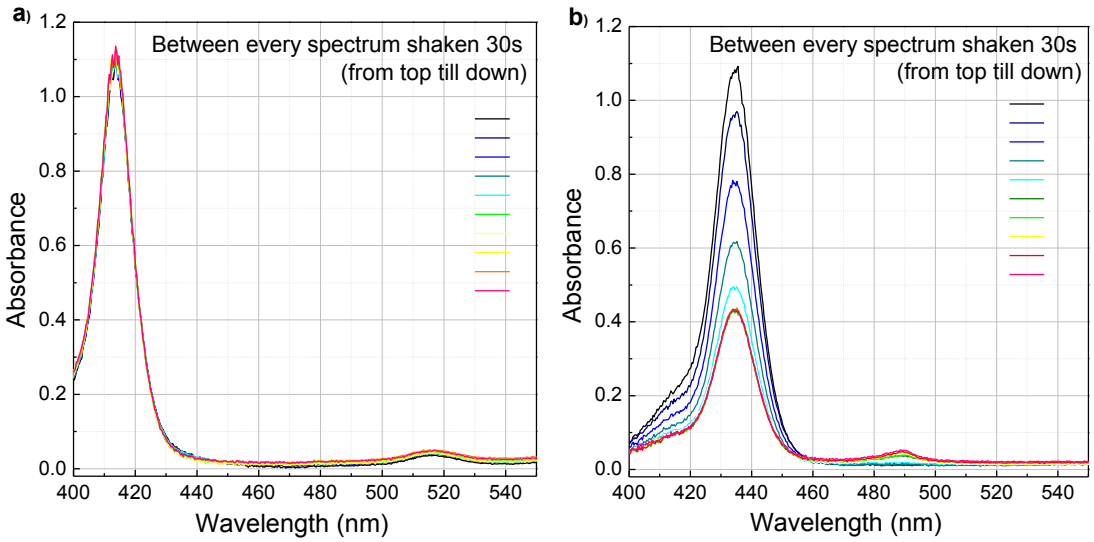

Figure S11. The stability of the free base (a) and the diacid form (b) of $TPPS_3$. A 1 ml solution of 4 µM $TPPS_3$ is poured into a Hellma quartz cuvette and absorbance spectra are measured after shaking the solution for 30 seconds.

Although the free base form of $TPPS_3$ looks rather stable, there is a hint that the aggregation kinetics differ for old solutions of $TPPS_3$. When a low concentration of $TPPS_3$ is dissolved, the solution will slowly change over time ("aging"), resulting in slower aggregation kinetics. This is not tested but hinted at by all performed characterizing experiments. Micali et al. have seen this as well and proposed an explanation, *the zinc theorem*. The glass in which the solution is stored, contains zinc. The $TPPS_3$ solution can extract zinc ions and incorporate them inside the molecule. This will result in a positive charge inside the molecule, giving rise to slower aggregation kinetics. This theorem is not proven however.

Another important influence on both the aggregation kinetics and the chiral selection, is contamination. Contamination in the solution, such as dust, causes faster aggregation kinetics by facilitating nuclei formation. Thereby chiral selection can be influenced if the contamination contains chiral templates[39]. A contamination is easily acquired. For example in the magnetic field influence experiments, a new dilution of $TPPS_3$ was made of which for each aggregation 16.7µL was used in the aggregation experiments. Only diluting the batch destroyed the chiral selection (figure 4.9).

S8 Inhomogeneity of J-aggregates in solution

The analysis of the characteristic times was done for the monomer traces of $TPPS_3$ (435 nm) because the aggregate traces were less well defined. This is due to the fact that the aggregates are not homogeneously distributed in the solution. Figure S12 shows an example of the aggregation kinetics for both the monomers and aggregates. The monomer trace is a smooth line as almost always obtained in the aggregation. The aggregate trace is not a smooth line and the absorbance spectra at several times are shown inside figure S12 to show that this is not caused by for example a background shift.

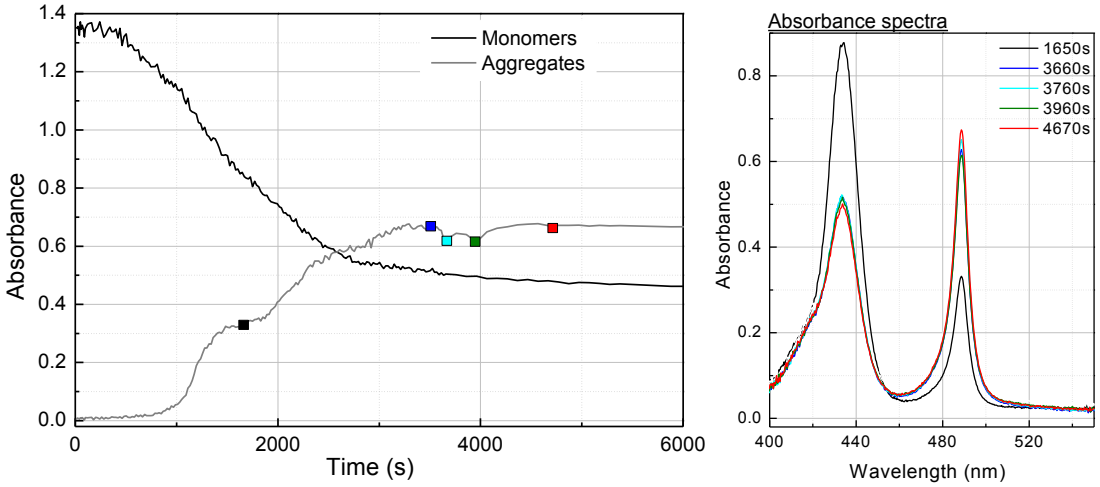

Figure S12. An example of the aggregation kinetics, showing both the monomer as the aggregate trace, respectively black and grey lines. The aggregate curve shows bumps and this is seen not only in the traces, but also in the full absorbance spectra at several times. For each depicted point an absorbance trace is given in the same color.

The J-aggregates are not homogeneously spread in the solution and it is seen that the aggregates stick to the walls of the vial. Figure S13 shows the aggregate trace at the first 5000 seconds. At 3850s the rotation is switched off resulting in a background shift in the absorbance spectrum, since the position of the vial can be slightly different. The aggregate absorbance differs however more than this background shift while the monomer absorbance does not. When rotating the vial the aggregate absorbance changes a lot, which can be explained by the fact that the aggregates stick to the walls of the vial and don't do this homogeneously.

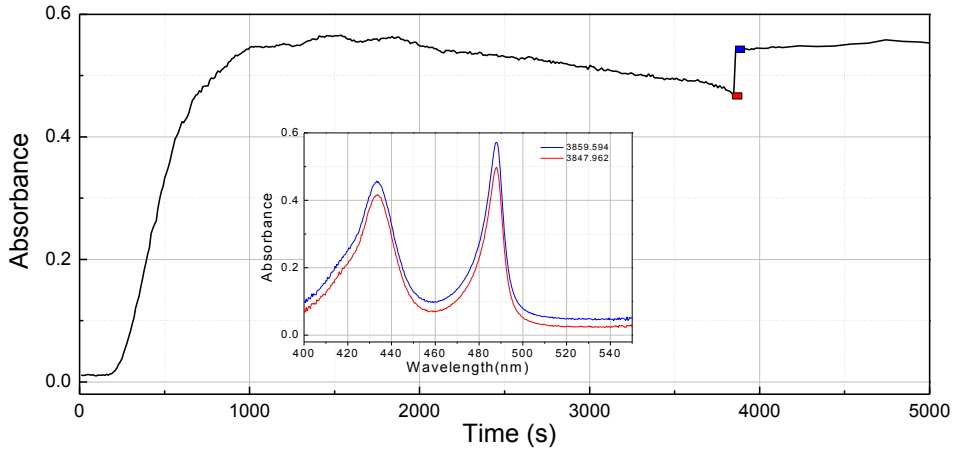

Figure S13. Influence of switching of rotation at 3850s, showing that the aggregates stick to the walls of the vial non-homogenously.

The magnitude of the aggregate absorbance in an equilibrated solution is also different between experiments, while equal amounts of monomer aggregated. This could be explained by the inhomogeneous distribution of the aggregates. For slower aggregations, the aggregate absorbance is on average lower, indicating more aggregates are not in the center of the vial.

Figure S14 shows pictures of equilibrated aggregation solutions. Figure S14a shows that after about two weeks, flocks of aggregates are formed in the solution and that there is sedimentation of these large clusters (figure S14b). Figure 14c is a vial after the removal of 1 ml of the sample needed for CD measurements. A green surface is present on the walls, showing the sticking of the aggregates on the vial walls. If these solutions are shaken, all is dissolved again.

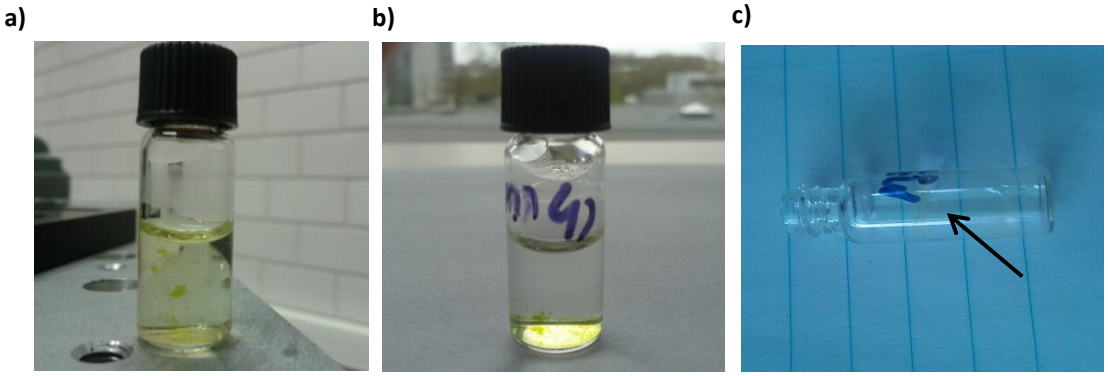

Figure S14. Pictures of aggregation solutions showing flakes of aggregates in the solution after two weeks (a) and sedimentation of the aggregates (b). Aggregates stick to the walls of the vial (c) which is seen after removing 1 ml of the solution for CD measurements.

S9. Example of a normalized spectrum including time parameters

Figure S15 shows an example of a normalized graph (logarithmic time scale) including the characteristic times of the monomer trace (435nm) of an aggregation performed to probe the influence of rotation.

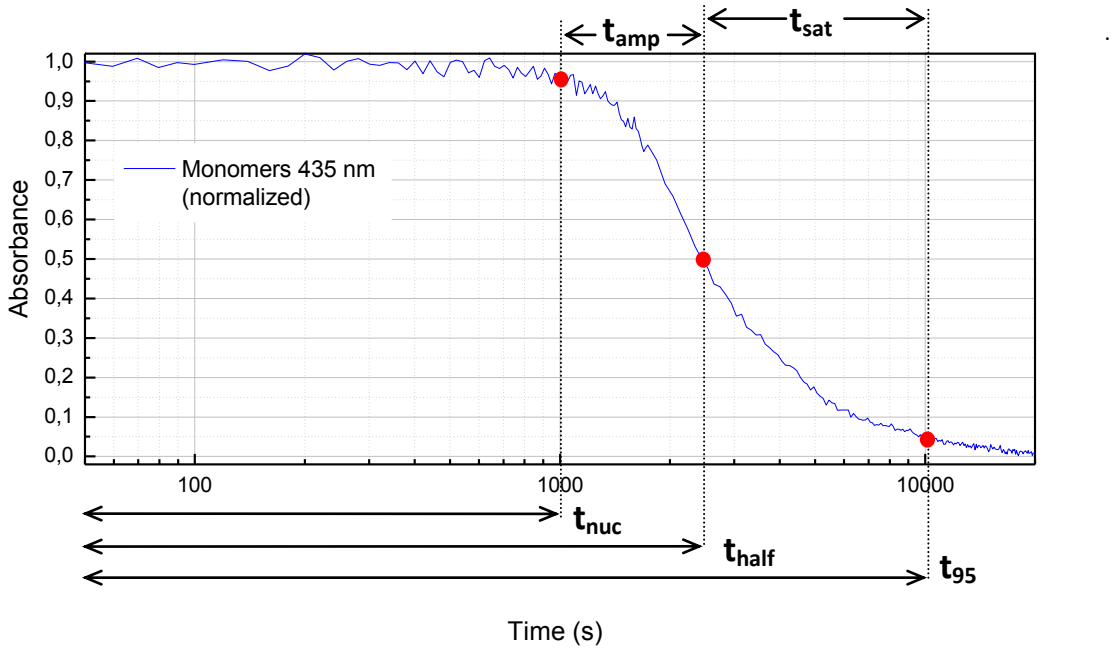

Figure S15. An example of a normalized trace including the time parameters

S10 Aggregation kinetics at 18°C and 28°C

Figure S16 and S17 show the background corrected monomer traces for both rotation (red) and stationary (blue) experiments for respectively 18°C and 28°C. These experiments are performed using the standard aggregation protocol with batch 1 of $TPPS_3$ and experimental setup 2. These experiments are performed to see the influence of rotation on the aggregation kinetics.

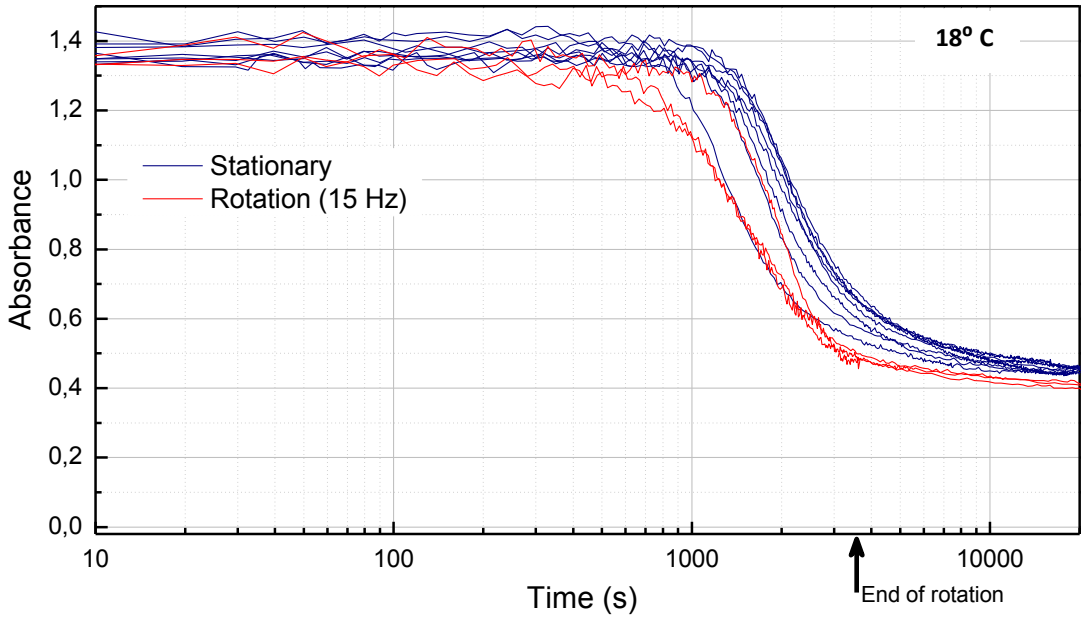

Figure S16. Kinetic spectra of the monomers with rotation (red) and without rotation (blue) during the aggregation process at 18° C.

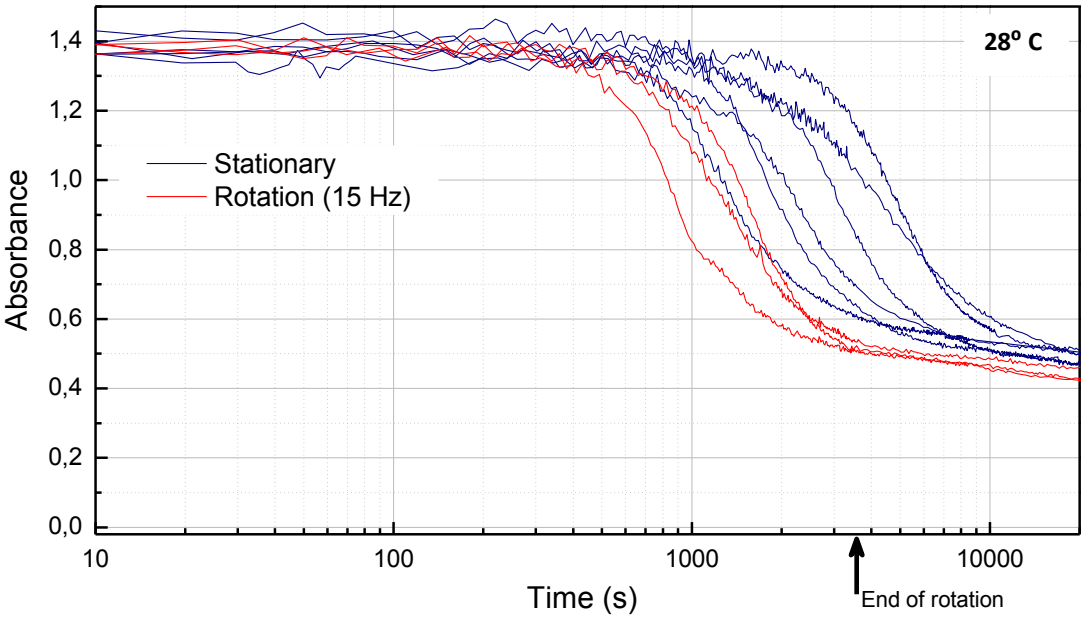

Figure S17. Kinetic spectra of the monomers with rotation (red) and without rotation (blue) during the aggregation process at 28° C.

Figure S18 and S19 show the analysis of these traces, displaying the characteristic times for respectively 18°C and 28°C.

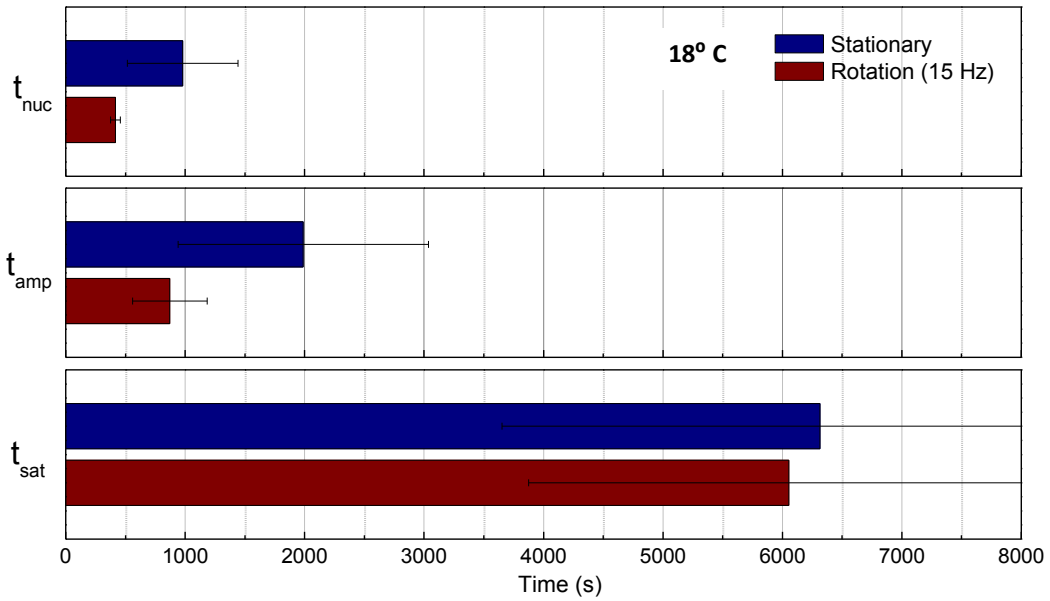

Figure S18. The influence of rotation on the aggregation kinetics expressed by the three characteristic times, t_{nuc}, t_{amp} and t_{sat} at a temperature of 18° C.

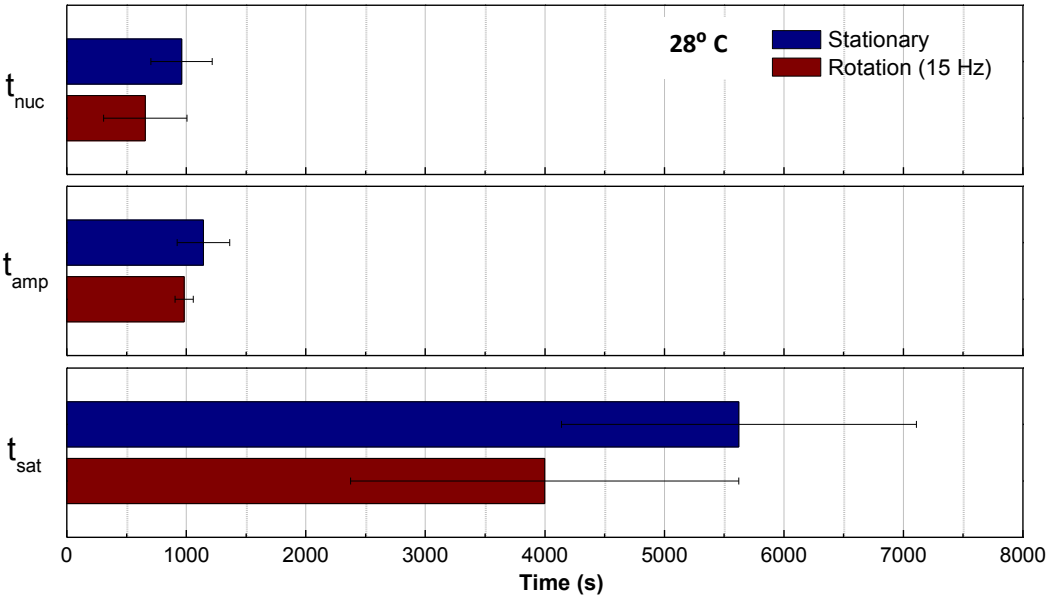

Figure S19. The influence of rotation on the aggregation kinetics expressed by the three characteristic times, t_{nuc}, t_{amp} and t_{sat} at a temperature of 28° C.

All of these figures are similar to figure 4.6 and figure 4.7a shown in the *section 4.2.2*. Rotation increases the speed of the aggregation. All characteristic times are on average shorter when the sample is rotated. Because of the large variation, there is some overlap between the two conditions. The temperature does not have a big influence on the aggregation kinetics. The equilibrium concentration of the monomers is higher for increasing temperatures (figure 4.7b) which is proven further in figure S22. The standard variations of the characteristic times increase with increasing temperature, but the averages are equal.

S11. Dissymmetry parameter Δg versus time parameters

The absolute value of Δg (representing the enantiomeric excess) is plotted against the three different time parameters t_{nuc}, t_{amp}, and t_{sat} for all experiments with the batch 1 in figure S20. These experiments are performed to probe the influence of rotation. No relation between the characteristic times and the enantiomeric excess is found.

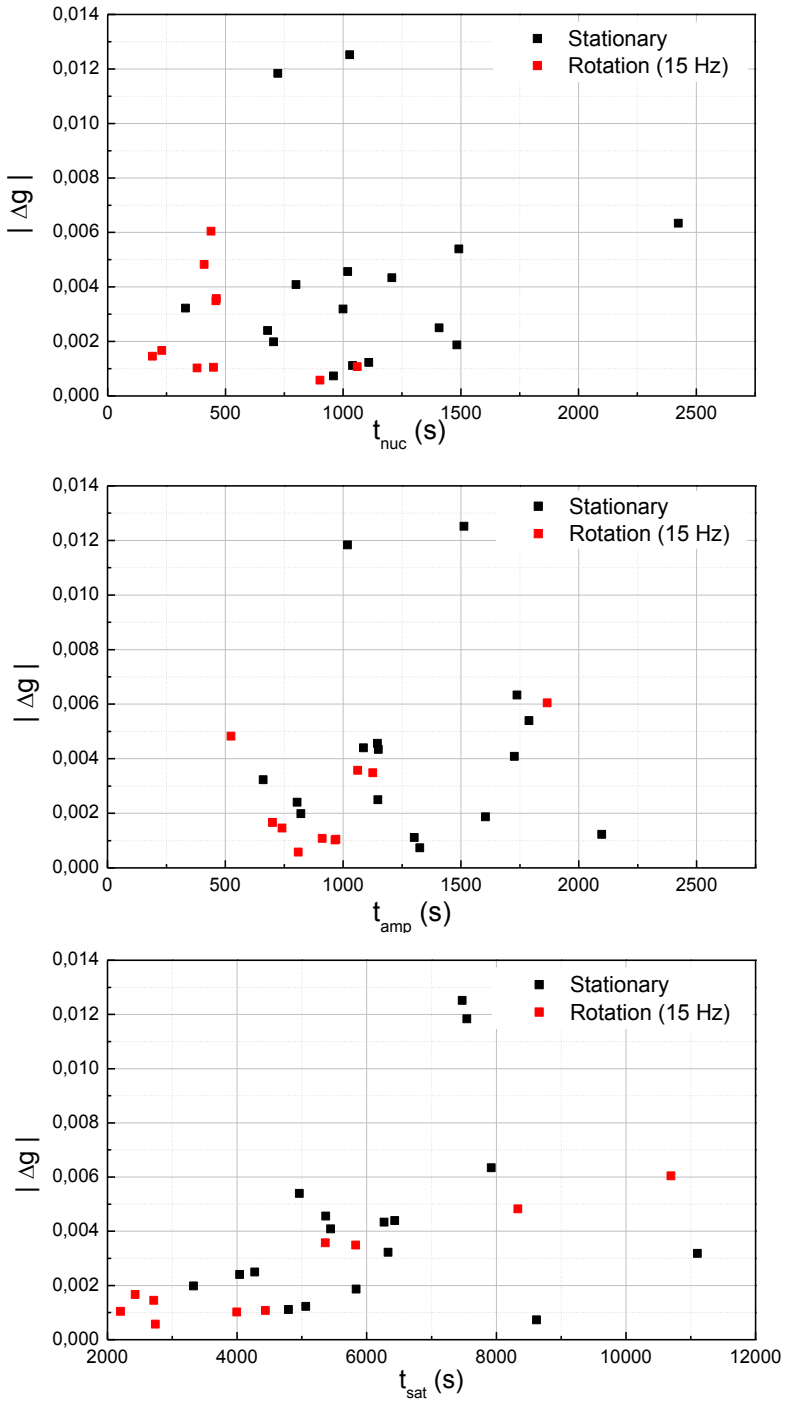

Figure S20. Absolute value of the dissymmetry parameter Δg plotted against t_{nuc} (a), t_{amp} (b) and t_{sat} (c) for all experiments involving batch 1 of $TPPS_3$ (probing the influence of rotation). Data points are grouped on aggregation conditions: stationary (black) and rotation (red).

For all experiments with batch 2, probing the influence of the magnetic field, the absolute value of Δg is plotted against the three different characteristic times t_{nuc}, t_{amp}, and t_{sat} in figure S21. Two data points are shown separately because their Δg value is beyond the reach of the figure. Again, no clear relation between the characteristic times and the enantiomeric excess is found. In the magnetic field experiments (both batch 2a and 2b), with increasing t_{nuc} and t_{amp}, increasing Δg values are obtained. The slope is however very small and it is not clear if this is a real trend.

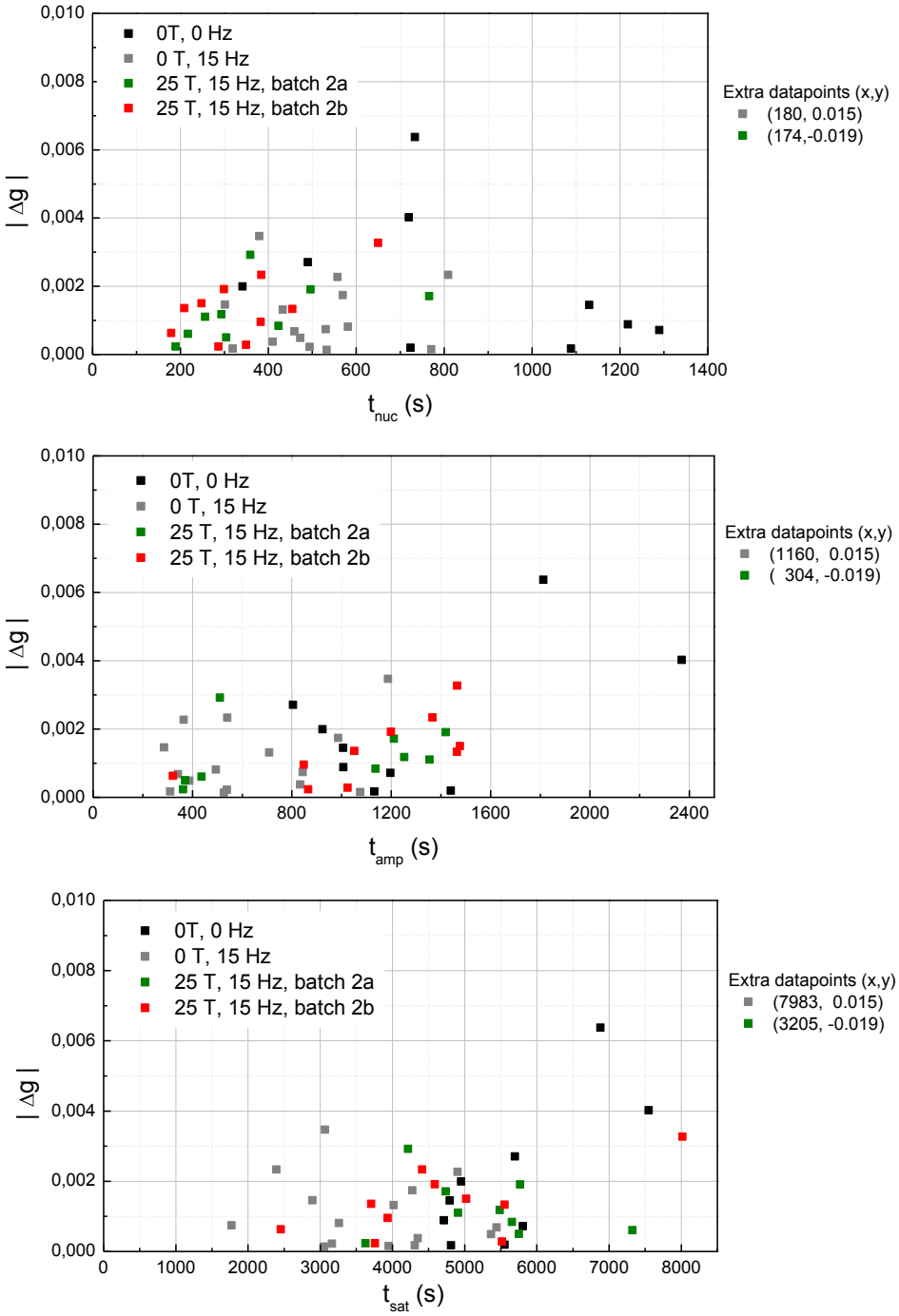

Figure S21. Absolute value of the dissymmetry parameter Δg plotted against t_{nuc} (a), t_{amp},(b) and t_{sat} (c) for all experiments with batch 2 of $TPPS_3$ (probing the influence of the magnetic field). Data points are grouped on aggregation conditions: stationary and 0T (black) , rotation and 0T (red), 25 T 15 Hz batch 2a (green) and 25T 15 Hz batch 2b (red). The coordinates of two extra data points are given on the right because their Δg value is out of the range of the figure.

S12. Influence of temperature on the equilibrium

Figure S22 shows the influence of temperature on an equilibrated aggregation solution containing both monomers and J-aggregates of $TPPS_3$. The temperature of the solution is set by the temperature controller of the *Jasco J815 CD spectrometer* and absorbance spectra are measured at several times and temperatures. At each temperature, the sample was not equilibrated yet as can be seen in the two different curves at 60°C (orange and red). This graph is however just to show that the aggregation of $TPPS_3$ is an equilibrium process and the temperature has an influence on this. This influence is expected since the monomers interact non-covalently in forming J-aggregates. By increasing the temperature, thermal energy is provided to the monomers to dissociate from the aggregates again.

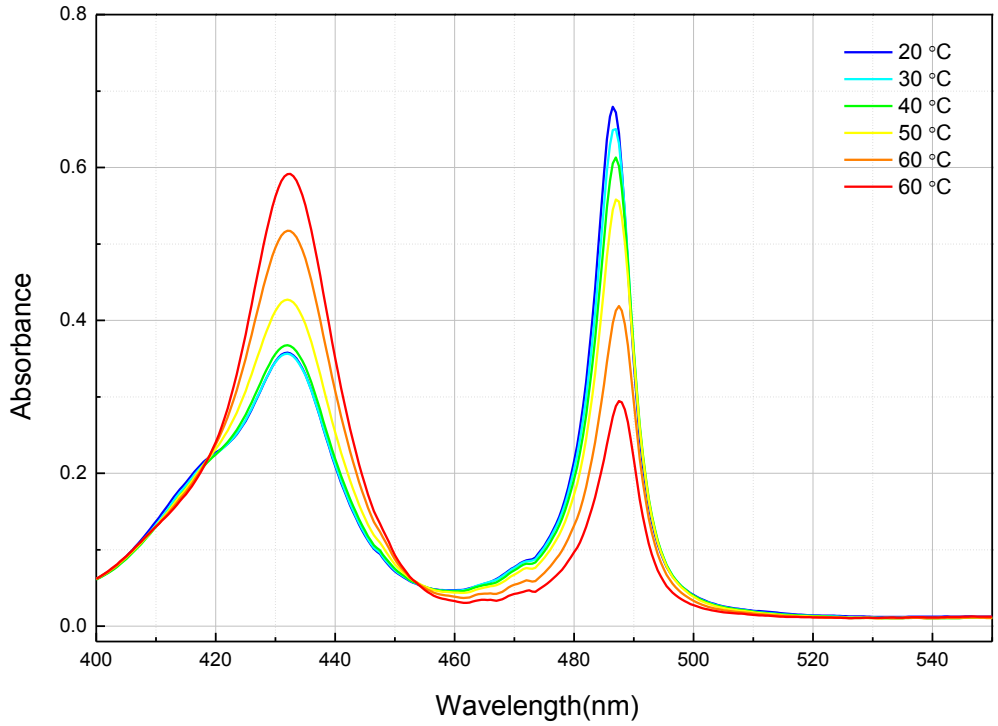

Figure S22. The influence of temperature on an equilibrated solution containing both monomers and J-aggregates of $TPPS_3$. This figure shows that the aggregation is an equilibrium process and that the equilibrium position is influenced by the temperature. At each temperature, the sample was not equilibrated yet as can be seen in the two different curves at 60°C (orange and red curve).

S13. Extra figures on the kinetic spectra of batch 2

Figure S23 shows the background corrected data of the aggregation kinetics for the zero field rotation experiments for both batch 2a and 2b. There is no big difference in the aggregation kinetics between these two batches if no magnetic field is applied.

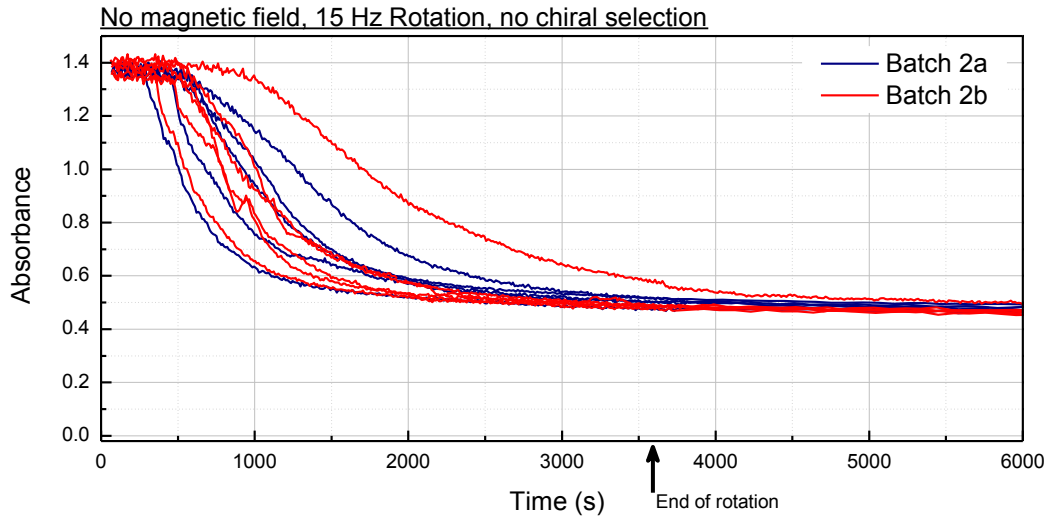

Figure S23. Zero field rotation experiments of batch 2a (blue) and batch 2b (red). There is no difference in the aggregation kinetics between these two batches if no magnetic field is applied.

Figure S24 shows the kinetic spectra of batch 2a and 2b together for clockwise and anticlockwise rotation without applying a magnetic field. There is a slight difference in the aggregation kinetics of clockwise and anticlockwise rotation, opposite to the aggregation kinetics obtained with the experiments of batch 2a of $TPPS_3$ in a magnetic field. Figure S24 shows that the two rotation directions have overlapping aggregation kinetics.

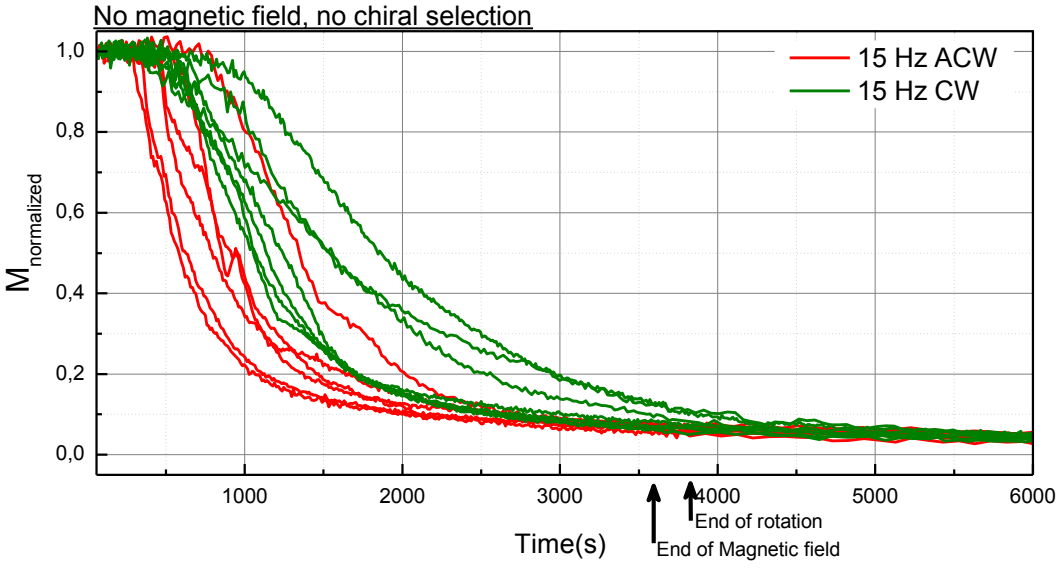

Figure S24. Kinetic spectra of the batch 2 for clockwise (green) and anticlockwise (red) rotation without a magnetic field.

S14. Influence of aggregation conditions on the percentage monomer left

Figure S25 shows the average value and standard deviation of the percentage of monomer left for the aggregations in several conditions. Rotation generally leads to a lower percentage of monomers left at 20.000s. In the magnetic field experiments with batch 2a(green), also a lower percentage of monomers left is observed while this is not observed for batch 2b(red). In the dilution leading to chiral selection thus more monomers aggregated within the first 20.000 s. This might say something about the thermodynamics of the formed aggregates. The standard deviations are however too big to be able to say that it is significant.

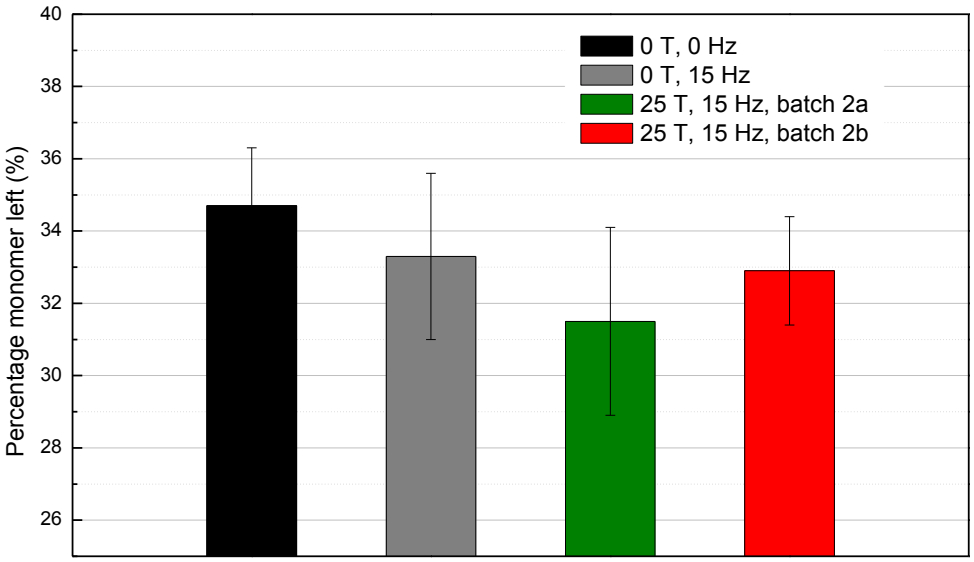

Figure S25. Influence of aggregation conditions on the percentage of monomer left.

S15. Influence of sweeping the magnetic field down from 25 T to 0 T

Several different effects on the absorbance of the monomers and aggregates are observed when sweeping the magnetic field down from 25T to 0 T. Figure S26a-d show the different cases and for all experiments, the absorbance change is given for both the aggregates and the monomers in table S3. The effect is the biggest on the aggregate absorbance which goes up in most of the experiments. The monomer absorbance also changes, but only slightly and only in a few experiments. The reason for the change in absorbance when sweeping the magnetic field down to 0 T is not known, but there are many possibilities.

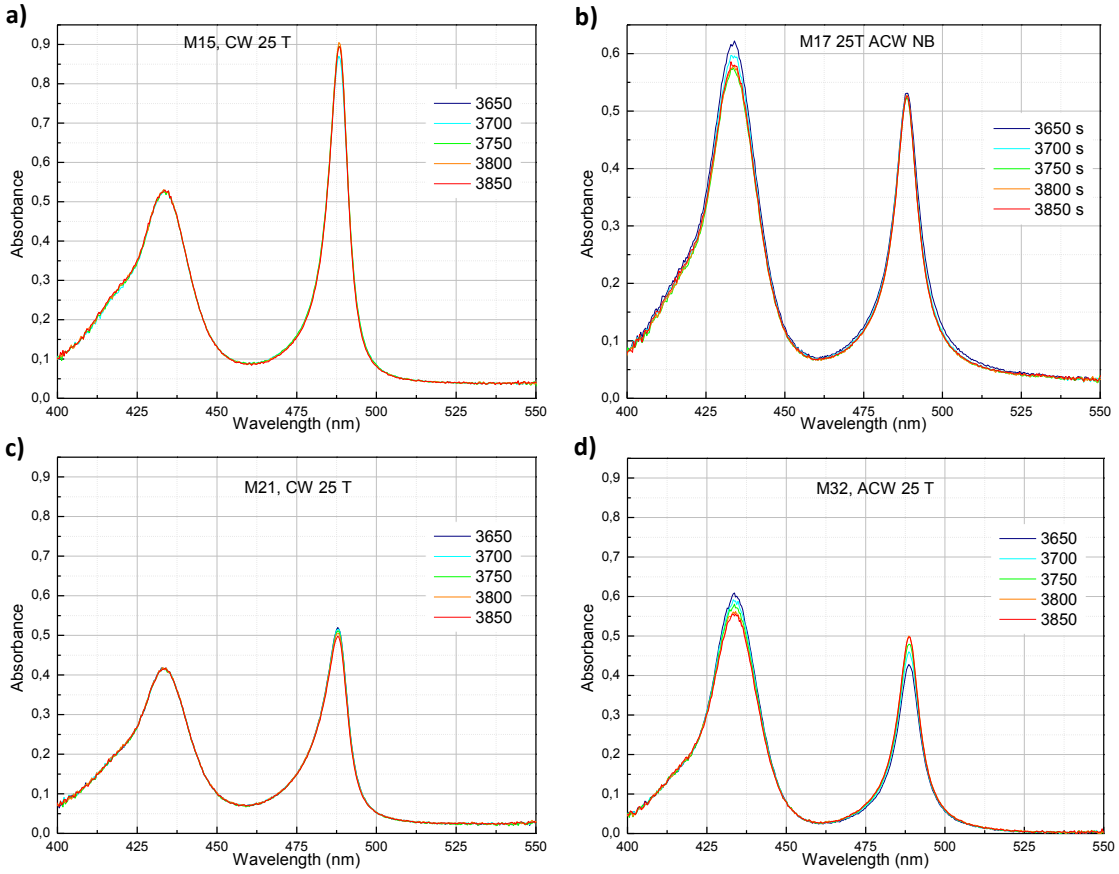

Figure S26. Effect of the magnetic field on the monomer absorbance *M* and aggregate absorbance *A*. a) M - and A ↑ , b) M ↓ and A - , c) M - and A ↓ and d) M ↓ and A ↑

Several influences of the magnetic field are the Lorentz force, the alignment force and the effective gravitational force (section *2.4*). The effective gravity in these experiments is equal to the normal gravity because the vials are placed at the center of the magnetic field (the field gradient is zero). The gravity thus is the same with and without magnetic field, thus this force cannot be an explanation for the absorbance change.

The Lorentz force and alignment force, however, are only present when the magnetic field is present. The Lorentz force can change the distribution of the aggregates and monomers and the alignment force changes the orientation of the aggregates (or clusters of approximately >1000 monomers). A change in distribution can definitely alter the measured absorbance because the light spot is in the middle of the solution. The Lorentz force is orientated differently directed for clockwise and anticlockwise rotating vials, so a different absorbance change would be expected for the different rotation directions. However, no such difference is observed in the absorbance change.

The alignment force can also result in an absorbance change, since the polarizability is not equal for the different directions in the molecule and therefore the absorbance along different directions in the molecule is different. The alignment is equal for all situations so this effect should be equal for all experiments.

Another important fact is that the aggregation is not yet equilibrated at the time the magnetic field is swept down. The monomers still are able to aggregate during the sweeping which also causes an absorbance change (monomer absorbance goes down and aggregate absorbance goes up). This aggregation might even be enhanced or reduced by the magnetic field in some way, causing the absorbance change.

Probably a combination of the previous influences causes the absorbance change when sweeping the magnetic field down from 25T to 0T. It is at least clear that the magnetic field has an influence on the distribution and/or orientation of the aggregates and also on the monomers, but to a lesser extent.

Table S3. Effect of the sweeping the magnetic field down monomer and aggregate absorbance.

Batch 2a

Experiment	**Rotation**	**Sign of Δg**	**Selection?**	**Effect on monomer M and aggregate absorbance A**
M10	CW	-	Yes	A ↑, M -
M12	ACW	+	Yes	A ↑, M ↑
M13	CW	-	Yes	A ↑, M ↑
M14	ACW	+	Yes	A ↑, M -
M15	CW	-	Yes	A ↑, M -
M16	CW	-	Yes	A ↑, M ↑
M17	ACW	+	Yes	A ↓, M ↓
M19	CW	+	No	A ↑, M -
M20	CW	-	Yes	A ↑, M -
M21	CW	-	Yes	A ↓, M -
M22	ACW	+	yes	A ↑, M -

Batch 2b

Experiment	**Rotation**	**Sign of Δg**	**Selection?**	**Effect on monomer M and aggregate absorbance**
M24	CW	+	No	A ↑, M ↑
M25	ACW	+	'yes'	A ↑, M -
M26	CW	+	No	A ↑, M -
M28	CW	+	No	A ↑, M -
M30	CW	+	No	A -, M -
M31	ACW	+	'yes'	A ↑, M -
M32	ACW	+	'yes'	A↑, M ↓
M33	CW	+	No	A ↑, M -
M36	CW	+	No	A -, M -
M37	CW	-	yes	A ↑, M -